# JET FORMATION AT THE SEA ICE EDGE

HAROLD DBS HEORTON

UCL PhD

January 2013

I, Harold Heorton confirm that the work presented in this thesis is my own. Where information has been derived from other sources, I confirm that this has been indicated in the thesis.

## Abstract

Mesoscale jet formation due to the Coriolis Effect is well understood over sharp changes in surface roughness such as coastlines (Hunt et al. 2004). This sharp change in surface roughness is experienced by the atmosphere flowing over, and ocean flowing under, a compacted sea ice edge. Sea ice edge jets have been observed (Johannessen et al. 1983). This thesis presents a study of a dynamic sea ice edge responding to atmospheric and oceanic jet formation during various wind and ocean current conditions. An idealised analytical model of sea ice drift is created using the momentum balance of Gray & Morland (1994) and the viscous plastic rheology of Hibler (1979). This is compared to an ice edge in the Los Alamos sea ice climate model (CICE) run on an idealised domain. A scheme has been developed which analyses sea ice concentration and adds jets to the CICE model forcing data. The response of the model to jet formation is tested at various resolutions.

The formation of atmospheric jets at the sea ice edge is shown to increase the wind speed parallel to the sea ice edge and results in the formation of a sea ice edge jet. The increase is dependent upon the angle between the ice and wind and results in an increase in ice transport along the sea ice edge of 40%. Observations and climate model data of the polar oceans has been analysed to show areas of likely atmospheric jet formation with the Fram Strait being of particular interest. The possibility of oceanic jet formation and the resultant effect upon the sea ice edge is less conclusive. The coupling between the components of climate models is currently crude and does not allow for jet formation (Maslowski et al. 2012). Most climate models also misrepresent the ice drift through the Fram Strait leading to errors in the prediction of Arctic sea ice extent.

# CONTENTS

# LIST OF FIGURES

# LIST OF TABLES

Table 1: Mathematical Notation

| | |
|---|---|
| | General Variables |
| $(x, y, z)$ | Eulerian postion vector |
| $\mathbf{u} = (u, v)$ | Two dimensional velocity vector |
| $= (u, v, w)$ | Three dimensional velocity vector |
| $\mathbf{k} = (0, 0, 1)$ | Vertical identity vector |
| $t$ | Time |
| $h$ | Thickness |
| $T$ | Temperature |
| $S$ | Salinity |
| $A$ | Sea ice concentration |
| $\rho$ | Density |
| $m$ | Mass |
| $P$ | Pressure |
| $f_c = 2\Omega \sin\theta$ | Coriolis parameter for latitude $\theta$ and the Earth's rotational speed $\Omega$ |
| $g = 9.8\text{m s}^{-1}$ | Gravitational acceleration |
| | Sea Ice Model Variables (Chapter 2) |
| $G(h, t)$ | Sea ice thickness distribution |
| $f$ | Sea ice growth rate |
| $\psi$ | Mechanical redistribution of sea ice |
| $\xi = \frac{\partial u_i}{\partial x_i}$ | Sea ice velocity divergence |
| $\rho_I$ | Sea ice density |
| $\alpha^I$ | Ratio of vertical to horizontal ice flux during ridging |
| $k^I$ | Sea ice mass transfer from leads |
| $q^I$ | Volume flux of surface accumulation |
| $b^I$ | Volume flux of basal melt |
| $c_T$ | Thermal capacity of sea ice |
| $k$ | Conductivity of sea ice |
| $I_0$ | Penetrating solar radiation |
| $\kappa_B$ | Beers extinction coefficient |
| $q$ | Energy of melting of sea ice |
| $L_o$ | Sea ice latent heat of fusion |
| $\mu_m$ | Relation between sea salinity and melting temperature |
| $\tilde{\boldsymbol{\tau}}^a$ | Atmospheric drag upon sea ice |
| $\tilde{\boldsymbol{\tau}}^o$ | Oceanic drag upon sea ice |
| $\mathbf{S}$ | Ocean tilt force |
| $\boldsymbol{\sigma}$ | Sea ice stress tensor |

| | |
|---|---|
| | Jet Calculations (Chapter 3) |
| $U_{A(O)}$ | Far field wind (ocean) speed |
| $(u', v')$ | Fluid velocity perturbations |
| $p$ | Pressure perturbation |
| $h_A$ | Far field ABL (Atmospheric Boundary Layer) height |
| $h_M$ | Far field OML (Ocean Mixed Layer) depth |
| $h$ | Perturbation to the shallow layer (ABL or OML) |
| $h_t$ | Perturbation to the ocean surface |
| $h_b$ | Perturbation to the mixed layer |
| $h_s$ | Surface shear slayer height |
| $l_s$ | Shear layer height |
| $z_{00}$ | Ocean surface roughness length |
| $z_0$ | Broken sea ice roughness length |
| $\rho_{A(O)}$ | Air (ocean) density in the ABL (OML) |
| $\Delta\rho_{A(O)}$ | Air (ocean) density inversion strength |
| $\Delta g_{A(O)}$ | ABL (OML) reduced gravity |
| $\mathcal{F}_{A(O)}$ | Atmospheric (Oceanic) Froude number |
| $\mathcal{L}_{RA(O)}$ | Atmospheric (Oceanic) Rossby radius |
| $(-\overline{u'w'})[z]$ | Reynolds stresses |
| $(-\overline{u'v'})[z]$ | |
| $\Delta(-\overline{u'w'})[z]$ | Reynolds stress perturbations |
| $\Delta(-\overline{u'v'})[z]$ | |
| $(\bar{u}, \bar{v})$ | Fluid velocity averaged perturbations |
| $\overline{F}, \overline{G}$ | Averaged body forces |
| $\phi, \phi\prime$ | Original and modified angle between far field wind or current and the sea ice edge |
| $(X, Y)$ | Non-dimensionalised position vector (aligned with the sea ice edge) |
| $\widehat{F}, \widehat{G}, \widehat{R}$ | Scaled forcing functions, |
| $\widehat{R}^{(0)}, \widehat{R}^{(1)}$ | leading and first order |
| $(\widehat{u}, \widehat{v})$ | Scaled velocity perturbation, |
| $\widehat{u}^{(0)}, \widehat{u}^{(1)}$ | leading and first order, |
| $\widehat{v}^{(0)}, \widehat{v}^{(1)}$ | aligned with wind or current |
| $\widehat{h}$ | Scaled thickness perturbation, |
| $\widehat{h}^{(0)}, \widehat{h}^{(1)}$ | leading and first order |
| $\Delta C_F, \Delta C_G$ | Surface drag parameterisation functions |
| $\Delta_0, \Delta_u$ | Surface drag component functions |
| $\kappa$ | von Kármán's constant |
| $\widehat{n}$ | Non-dimensional distance normal to the ice edge |

| | |
|---|---|
| $\Phi[X, Y]$ | Forcing potential function |
| $\widehat{\Delta C_F}$ | Scaled drag parameterisation |
| $u^2_{\text{diff}}$ | Ocean and sea ice velocity difference parameterisation |
| $J^{(0)}, J^{(0)}$ | Jet solution functions |
| $J^{(0)'}, J^{(0)'}$ | and derivatives |
| $\widetilde{u}$ | Velocity perturbation normal and |
| $\widetilde{v}$ | parallel to the sea ice edge |
| $\widetilde{U}$ | Complete velocity normal and |
| $\widetilde{V}$ | parallel to the sea ice edge |
| $\widehat{U}_{O(1,2)}$ | Far field ocean velocity components |
| $\widehat{U}_{I(1,2)}$ | Ice drift velocity components |
| $d$ | Ice edge typical length |
| | Analytical Model (Chapter 4, Appendix A) |
| $C_{a(o)}$ | Atmospheric (oceanic) drag |
| $\mathbf{U}_a$ | Wind velocity |
| $\dot{\varepsilon}_{ij} = \frac{\partial u_i}{\partial x_j}$ | Sea ice strain rate |
| $p$ | Internal ice pressure |
| $e$ | Plastic yield curve eccentricity |
| $\eta, \zeta$ | Shear and bulk viscosities |
| $g(A)$ | Ice strength parameterisation |
| $c$ | Ice strength constant parameter |
| $\widehat{\mathbf{u}} = (\widehat{u}, \widehat{v})$ | Non-dimensionalised sea ice velocity |
| $U_I$ | Typical sea ice drift speed |
| $\widehat{\boldsymbol{\tau}}^{\boldsymbol{a(o)}}$ | Scaled atmosphere (ocean) drag |
| $\mathcal{T}_{a(o)}$ | Typical atmosphere (ocean) drag |
| $\alpha_{1,2}$ | Constants and functions in equations |
| $\beta_{1,2,3}$ | (4.2.8) and (4.2.9) |
| $\mathbf{T}_{1,2}$ | Combined forcing functions |
| $u^{a(o)}_{\widehat{n}}, v^{a(o)}_{\widehat{n}}$ | Scaled wind (current) components |
| $\widehat{\mathbf{U}}_O, \widehat{\mathbf{U}}_I$ | Typical non-dimensional ocean and ice velocity for $u^2_{\text{diff}}$ |
| $A_i$ | Ice concentration expansion |
| $u_i, v_i$ | Ice velocity expansion |
| $\epsilon$ | Small expansion factor |
| $\alpha$ | and expansion power |
| $\mathcal{X}$ | Length contacted variable |
| $\mathcal{D}_{ij}$ | Contracted parts of the stress tensor |
| $\widehat{\sigma}_{ij,\mathcal{X}}$ | $\mathcal{X}$ derivative of expanded stress tensor |
| $X_{\text{peak}}$ | Point of peak wind or current speed |
| $g_i(A)$ | Ice strength approximation functions |
| $A_i, m_i, c_i$ | Constants of approximation |
| $\mathcal{Q}_i$ | Sets used in approximation |
| $l$ | Distance from ice edge, CICE forcing |

## Acknowledgements

There are two central figures involved in the writing of this thesis. First is my supervisor Danny, without whom the transition from floundering calculations and appalling writing to a PhD thesis would never been possible. Secondly is my wife Becca. During the course of my study we have created two beautiful girls and have got married. I would never have managed to stay sane through all of this and finally finish my PhD without you Becca.

Many others amongst my family and friends have provided much needed insight and direction. Special mention goes to Ann Keen at the Met Office Hadley centre, Rosie, Nikhil, Michel and Alek at CPOM and to Seymour and Katherine who have recently passed away. The development of the atmospheric and oceanic jet theory was greatly assisted by Julian Hunt.

This thesis was funded by the Natural Environment Research Council with case sponsorship from the UK Met Office.

For Iris and Hazel.

# CHAPTER 1

# INTRODUCTION

To introduce you to this thesis key ideas and existing research are presented in this chapter. A description of sea ice is presented in section 1.1. Jet formation is introduced in section 1.2 and a review of research at the sea ice edge is presented in section 1.3. Detailed descriptions of modelling processes are reserved for discussion in chapter 2. Finally the introduction is summarised leading to the aims of this thesis in section 1.4.

## 1.1 Sea Ice

Sea ice is frozen sea water that floats upon the surface of the Earth's polar oceans. The extent of sea ice cover is in constant flux as it melts and refreezes with the changing seasons. It covers between 4-6% of the Earth's surface (between 17.5 - 28.5$\times 10^6$ km$^2$) at any time (Comiso 2003).

During winter in the northern hemisphere sea ice fills the Arctic Ocean (see figure 1.1). It extends into the northern Atlantic Ocean in the Greenland and Labrador Seas and in the Baltic Sea. As the temperature increases in summer the ice retreats back to the Arctic Ocean opening up the Canadian Archipelago and

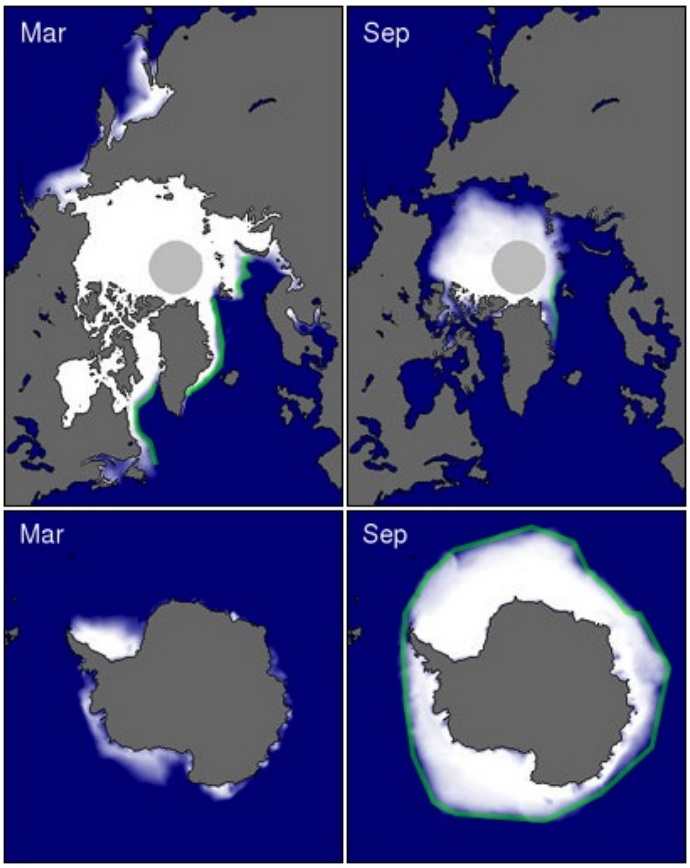


Figure 1.1: Mean sea ice extent 1979-2000 (`http://nsidc.org/cryosphere/sotc/sea_ice.html`). Marginal Ice Zones are highlighted in green. Image courtesy of the National Snow and Ice Data Center (NSIDC), University of Colorado, Boulder

Siberian Sea and halving the sea ice extent (see figure 1.2). Sea ice can also exist in non polar seas, the Baltic and Caspian for example (Kouraev et al. 2003).

The South Ocean presents the opposite oceanic system to the north. Whereas the Arctic ocean is surrounded by land, the Antarctic continent is surrounded by the Southern Ocean. During winter in the southern hemisphere sea ice surrounds Antarctica up to $60^{\circ}$ south (figure 1.1). During summer the sea ice melts revealing the coast of the Antarctic continent except for a few locations such as the Weddell Sea east of the Antarctic Peninsula .

Arctic sea ice extent has been observed to be reducing, with an unprecedented summer low in September

2007 (Comiso et al. 2008) and further lows in 2008 and 2011 and a new record low in 2012 (see figure 1.2). The September minimum sea ice extent over the period 1953-2011 is observed to be reducing at a rate of -6.2% decade$^{-1}$ with an accelerate rate of approximately -10% decade$^{-1}$ for the period 1979-2011 (Stroeve et al. 2012). The March maximum has also decreased, though at a lesser rate of approximately -2% decade$^{-1}$ (Stroeve et al. 2012). Stroeve et al. (2008) attribute the decline in Arctic sea ice extent to a thinning sea ice cover and changing atmospheric conditions over the Arctic causing an increased export of sea ice out of the Arctic ocean to warmer waters. The decrease in sea ice extent is an acceleration from the trend over the last 30 years that was not forecast or captured in global climate models (Stroeve et al. 2007). Stroeve et al. (2007) comment that models with better physical representation of the sea ice physics do a better job of capturing the trend. Further discussion of sea ice modelling and climate modelling is presented in chapter 2. Continuous sea ice cover in the Arctic ocean is no longer a certainty and many would think it unlikely giving predictions of an ice free Arctic in the summer (Wang & Overland 2009, Stroeve et al. 2008, Holland et al. 2006).

The Antarctic however has seen a small increase in sea ice extent ($\approx$1% decade$^{-1}$ Cavalieri & Parkinson 2008) particularly in the Ross sea ($\approx$4% decade$^{-1}$ Comiso et al. 2011). This increase is also attributed to changing atmospheric conditions (Holland & Kwok 2012) and is further discussed in chapter 2.

The sea ice cover is made up of individual irregularly shaped sheets of sea ice called floes (Untersteiner 1986). The sea ice floes are typically 1-30 km in diameter (Herman 2010). The state of the sea ice cover is determined by the temperature of the ocean surface and fluxes between the atmosphere and ocean (Thorndike et al. 1975). Sensible heat fluxes are the change in temperature of the sea ice, latent heat fluxes alter the sea ice mass through melting and freezing (Untersteiner 1986). The underside of the sea ice pack is assumed to be at the freezing point of sea water (-1.8°C, Untersteiner 1986) as a higher or lower temperature would cause the melting or growth of sea ice respectively. The atmospheric temperature above the sea ice varies seasonally. Comiso (1994) give summer atmospheric temperatures that can be as high as 1°C above sea ice in both the Arctic and Antarctic and winter temperatures as low as -25°C (Antarctic) and -35°C (Arctic). A cold atmosphere lowers the temperature of the sea ice causing the formation of new ice on the underside of the sea ice pack (Thorndike et al. 1975). As the underside of the sea ice is in contact with the ocean and is at its melting point, the sea ice insulates the ocean from the cold atmosphere (Toole et al. 2010).

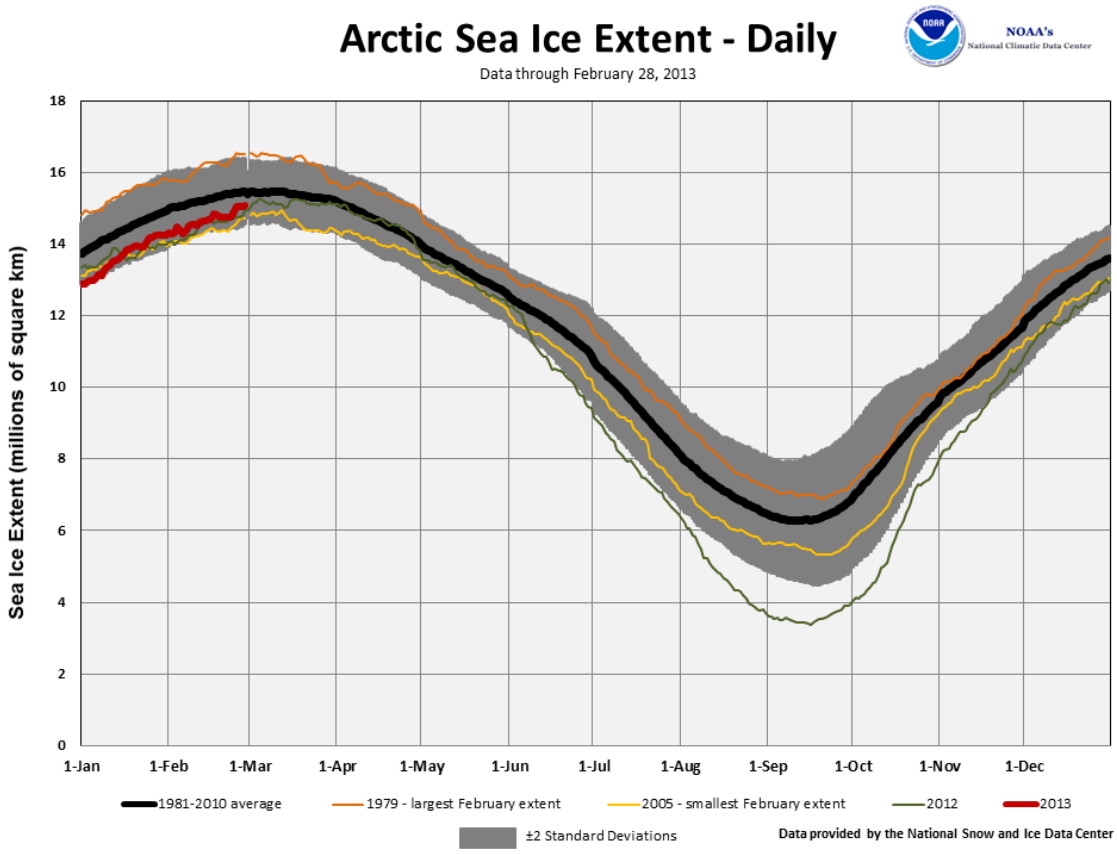


Figure 1.2: 2012 and 2013 (up to February 28th) Arctic sea ice extent compared to the period 1979-present (`http://www.ncdc.noaa.gov/sotc/global-snow/`). The sea ice extent varies continually throughout the year with the minimum extent typically occurring in September. The 2012 September extent (red line) is lowest ever observed. Image/data courtesy of the National Snow and Ice Data Center (NSIDC)/ National Oceanic and Atmospheric Administration (NOAA)

Alternatively the sea ice insulates a warm atmosphere from a cold ocean. The warm atmosphere will increase the temperature of the sea ice. If the sea ice temperature becomes greater than its freezing point, it will melt (Untersteiner 1986).

Mechanical deformation to sea ice is observed to be concentrated into kinematic features which are long and thin, stretching for hundreds of kilometres across the sea ice pack (Kwok 2001). If the sea ice cover is compressed horizontally due to a converging sea ice cover it can distort (Wadhams 2000). These distortions come in the form of pressure ridges when two sea ice floes are compressed together or sheared past one

another piling up ice about the floe boundary (Feltham 2008). The ice thickness in pressure ridges can be in excess of 20 m, mostly contained in keels below the sea ice (Bourke & Garrett 1987). The ice can also distort under tensile stresses, cracking to form leads (in the open ocean) and polynyas (near land masses) (Wadhams 2000). Cracks in the sea ice expose the open ocean to the atmosphere and account for more than 70% of the upward heat fluxes although only cover 1 to 2% of the ice pack (Marcq & Weiss 2012).

Sea ice is comparatively fresh compared to sea water (Aagaard & Carmack 1989). As sea water freezes to form sea ice brine is ejected and conversely during melting events, fresh water is introduced to the ocean (Aagaard & Carmack 1989). Sea ice is therefore linked to the the salinity of the ocean. As water of higher salinity is denser, sea ice formation can cause the sinking of cold polar water along continental slopes in the polar oceans (Rudels 1995). The formation of cold deep water helps drive the global thermohaline circulation (Broecker et al. 1995) which redistributes heat and salt throughout the world's oceans.

Albedo is a measure of how much solar radiation is reflected away from a surface (Curry et al. 1995). The albedo of sea ice is high compared to that of the ocean. Sea ice reflects 80-90% of the Sun's energy compared to 10% by the open ocean (Curry et al. 1995). The occurrence of melt ponds (pools of melted sea ice water trapped above the sea ice, Fetterer & Untersteiner 1998) can alter the albedo of sea ice to about 20% during the melting season (Perovich et al. 2002). This difference in reflectivity causes a feedback mechanism where the melting of sea ice leads to a smaller sea ice ice cover, causing the greater absorption of heat energy into the ocean and more sea ice melting (Curry et al. 1995).

## 1.2 Jet Formation

In the study of fluid dynamics, bands of increased fluid velocity relative to the surroundings are often encountered. Examples are the Jet Stream in the North Atlantic Ocean and laminar boundary layer flow near solid obstacles. These bands are named as jets and their formation can be caused by a variety of physical phenomena such as turbulence (Belcher et al. 1990), surface gradients (Hunt et al. 2004) and boundary layer flow (Dyke 1975).

Atmospheric jets are known to form over coastlines with a band of faster wind centred over the shore (Simpson 2007). Wind patterns where the sea meets the land are best understood by sailors who encounter

them on a daily basis (Simpson 2007). The atmospheric jets are colloquially known as "bends" to the wind. The location of these bends and the faster winds associated with them can give a key advantage in yacht races. Houghton (1992) gives direction to sailors to search for faster winds closer to the coast. There are further observations of "rivers of wind" (Laing & Brenstrum 1996) at coast lines, of particular interest is Pomeroy & Parish (2001) who present a study of jet formation along the Californian coastline.

A particular formation of atmospheric jets over coastlines can be accurately described by modeling the Coriolis acceleration on flows over a sharp change in surface roughness (Hunt et al. 2004, Orr et al. 2005*a*). The model presented by Hunt et al. considers wind jets formed over various surface roughness and elevation features. The model uses turbulent boundary layer theory (Belcher et al. 1993) considering processes that are of too small a scale to be resolved by current numerical atmospheric models. Of particular interest to this thesis is the study of bands of increased surface roughness at an arbitrary angle to a uniform wind field. This arrangement can be found at a compacted sea ice edge in the open ocean during on-ice winds (Massom et al. 2008). There are further requirements for the state of the atmosphere during jet formation which are discussed at the beginning of chapter 3. A similar jet formation is also possible for winds flowing off-ice (Orr et al. 2005*a*) although such an arrangement will tend to disperse the sea ice edge (Lu et al. 2008) smoothing the sharp change in surface roughness length (Birnbaum & Lupkes 2002).

The sea ice edge presents a similar change in surface roughness length to that found at coast lines. The surface roughness lengths of both are approximately 0.001 - 0.01 m as described by Jarmalavicius et al. (2012) for coast lines and Guest & Davidson (1991) for the sea ice edge. The roughness length of sea ice can vary and is further discussed in section 3.1.4. The theory of Hunt et al. defines a sharp change as over 1-10 km. This length scale criterion is met by a compacted sea ice edge (Massom et al. 2008). The surface roughness of the ocean surface is variable depending upon wave state (Donelan et al. 1993), which in turn depends upon wind speed (Drennan et al. 2003). The maximum roughness length associated with the open ocean surface is around $10^{-4}$ m, several orders less than over sea ice (Fairall et al. 2003).

Sea ice at the sea ice edge is often free drifting and driven by winds and ocean currents (Vihma et al. 1996). The relationship between sea ice drift and wind stress is often an Ekman Drift (Ogi & Wallace 2012) where there is a constant angular difference between the ice and wind velocity vector (Csanady 2001). The applied stresses from the atmosphere and ocean also drive the drift of pack ice along with internal ice stresses

(Hibler 1986). The strength and direction of the drift is a major factor in sea ice extent. For example Ogi & Wallace (2012) show the circulation of Arctic polar winds can cause low sea ice extents if directed towards the Fram Strait.

The sea ice component of global climate models at best crudely parameterises processes at the sea ice edge (McLaren et al. 2006). These parameterisations include an increased atmospheric drag over the Marginal Ice Zone and increased melting for low ice concentrations (chapter 2). Other climate models do not consider the changing sea ice state at the sea ice edge (increased roughness for example, see chapter 2). Atmospheric jets at the sea ice edge have previously been considered by Glendening (1994) through the occurrence of coastal fronts, a rapid change in temperature and wind strength. Glendening focusses on the development of the Atmospheric Boundary Layer (ABL) due to thermal forcing and does not use the same methods as Hunt et al..

An atmospheric phenomena of similar scale to the roughness driven coastal jets are low level jets (Smedman et al. 1993). These jets have been observed over many of the world's oceans such as the Arabian Sea (Grossman & Friehe 1986), the Californian coast (Zemba & Friehe 1987, Gerber et al. 1989) and Baltic Sea (Smedman et al. 1993). These jets are characterised by an increasing wind speed with height with a peak at a certain height before a decrease in speed (Smedman et al. 1993). Low level jet formation in the Baltic Sea during the summer is shown to be a result of of warm air flowing from the land to over the cold ocean (Smedman et al. 1993). This causes the rapid stabilisation of the lower atmosphere and the subsequent frictional decoupling (i.e the atmosphere becomes independent of surface conditions) which, through turbulence, causes the formation of a low level jet (Hogstrom & Smedman 1984).

There have been several observations of low level jets over the sea ice edge (Vihma & Brummer 2002) and sea ice pack (Andreas et al. 2000). These jets develop vertically with a peak wind speed at $\approx 100$ m from the ocean surface. Vihma & Brummer (2002) attribute the jet formation to changing baroclinity (a measure of air pressure and density gradient alignment, Csanady 2001), due to the jet's on - ice direction and the temperature difference between the open ocean and sea ice pack. Andreas et al. (2000), however, discount this method for low level jet formation in the sea ice covered Weddell Sea. The jets they observed were of varying direction and exhibited a turning angle. Because of these reasons Andreas et al. account for the low level jet formation through the decoupling of the atmosphere through stable stratification.

The various methods of low level jet formation discussed above are caused by thermal differences at the Earths surface. The jet formation discussed in this thesis is caused by a change in surface roughness length and has not previously been considered over sea ice.

## 1.3 The Sea Ice Edge

The transition from open ocean to a continuous sea ice cover is not a clearly defined edge. The build up of ice occurs over a distance defining the Marginal Ice Zone (MIZ). The MIZ contains sea ice floes typically smaller than in the sea ice pack with a width of 5-50 m and a thickness 1-2 m (Frankenstein et al. 2001, Lu et al. 2008). Figure 1.3 shows sea ice conditions typical of the MIZ. The state of the MIZ, and thus the extent of the sea ice pack, can change rapidly due to changing atmospheric and oceanic conditions. For example King et al. (2010) observed a rapid retreat of the sea ice edge in the Bellingshausen Sea due to prolonged on-ice winds.

The effect of land upon sea ice and the MIZ leads to there being only four MIZs of significant size: in the Greenland Sea, the Labrador Sea, the Bering Sea and the Antarctic Ocean with a complete circumpolar ice edge during April to December (see highlighted green areas in figure 1.1). During the summer months in the seas north of Russia, due to the sea-ice edge's proximity to land and the absence of any significant wave generation, the ice edge does not differ that greatly from the sea-ice pack and the MIZ is small and almost non existent (Wadhams 2000).

The transition zone exists due to the large floes of the sea ice pack (1-30 km in diameter, Herman 2010) being unable to exist at the sea ice edge due to wave interaction (Meylan & Squire 1994). Ocean waves, upon encountering a region covered with sea ice, will be partly reflected back into the ocean with a portion able to propagate beneath the ice cover (Lu et al. 2008). Ocean waves passing through an ice floe impart a bending stress. If the stress is great enough the floe will break. The act of moving the ice floes and potentially breaking them up dampens the ocean waves. These interactions account for the increasing floe size (Lu et al. 2008) and decreasing wave strength at greater distances into the sea ice pack. Measurements of waves in the sea ice pack have been made from ships (Robin 1963), submarine (Wadhams 1978), buoys and aircraft (Liu et al. 1991). As a thicker sea ice floe has greater strength against bending stresses, the floe

Figure 1.3: Ice breaker in the marginal ice zone of the McMurdo Sound, Antarctica. Note the small broken ice floes. The width of the foreground is approximately 500 m.

thickness and size distributions in the MIZ are strongly linked (Toyota et al. 2011) with the thicker floes tending to be of a larger diameter. When a storm encounters the sea ice edge the large waves associated with it can break up the sea ice floes rapidly altering the state of the sea ice edge (Asplin et al. 2012).

The interaction of waves and sea ice within the MIZ has been widely studied and wave attenuation coefficients have been calculated (Wadhams et al. 1988, Hayes et al. 2007) along with models of wave ice interaction (Meylan & Squire 1994, Kohout & Meylan 2008).

During freezing events the marginal ice zone is an area of sea ice formation (Pedersen & Coon 2004). The first state of sea ice formation is frazil ice: a suspension of ice crystals in sea water (Untersteiner 1986). As more of these ice crystals form they agglomerate into grease ice, a soupy layer of frazil crystals, or pancake ice which is roughly circular pieces of new ice up to 4 m in diameter (Weeks & Ackley 1986). The formation of new ice ejects brine into the upper ocean (Rudels 1995).

The upper layer of the ocean is known as the Ocean Mixed Layer (OML). This layer is defined as a well mixed layer with constant temperature, salinity and density (Williams et al. 2008). The bottom of the

layer is at a level of strong gradient in density. The state of the OML in the MIZ, particularly its depth, is strongly linked to the sea ice cover, for example the Antarctic the OML is thin in the summer and deep in the winter (Gordon & Huber 1990). The difference in depth is accounted for by the entrainment of deeper water thickening the layer in the winter (Markus 1999). In the Arctic Ocean the warm Atlantic water continually interacts with the sea ice edge altering the bouyancy of the layer (McPhee & Morison 2001). The state of the OML can conversely affect the state of the sea ice edge. Watanabe et al. (2004) show how a difference in ocean temperature continually melts ice at the sea ice edge in the sea of Okhotsk. The polar OML is a widely studied topic due to the large ecosystems that it supports (see Williams et al. 2008).

The compaction of the MIZ due to continued on-ice winds has been observed in the Antarctic (Massom et al. 2006, Massom et al. 2008, King et al. 2010). These observations are from the Bellingshausen Sea west of the Antarctic Peninsula during anomalous weather patterns that caused unusually prolonged on-ice winds. In these events the broken floes of MIZ were compacted by winds over a period of approximately one week retreating the sea ice edge by up to 250 km. At this time the ice concentration at the sea ice edge had reached near 100% resulting in a halt in the ice retreat and a relatively thin MIZ covering the outer 10 km of the ice pack (Massom et al. 2008).

Off-ice winds will conversely tend to disperse the ice edge, though bands of ice are likely to form (Lu et al. 2008). These bands of ice can be accounted for due to sea breezes (Chu 1987), wave interaction and ocean stresses (Fujisaki & Oey 2011). The ice edge is also likely to disperse for a still atmosphere and ocean. The internal ice pressures of sea ice in the marginal zone have been shown to have an expansion effect (Flato & Hibler 1989) when not externally forced by atmospheric and oceanic stresses. This expansion may however be due to the model rheology (as discussed in section 2.3.1) and there are limited observations of the sea ice edge during calm winds and a still ocean which prohibit a study of this.

The lowest part of the atmosphere is known Atmospheric Boundary Layer (ABL) which is typically well mixed with a sharp decrease in air density at the top of the layer (Brümmer & Thiemann 2002). For on-ice winds, particularly in winter, the large temperature difference between the ocean (typically 0° C) and sea ice (-10° C to -15° C) (Vihma & Brummer 2002) results in a stably stratified atmosphere (air density decreases with increasing altitude) over the sea ice edge (Brümmer & Thiemann 2002). However during the melting season the sea ice can be of a greater temperature than the ocean due to the freezing point of the relatively

fresh sea ice being greater than the ocean. This results in a less stable ABL. For the majority of on-ice winds the atmosphere is stably stratified in both the Arctic (Vihma & Brummer 2002, Vihma et al. 2003) and Antarctic (Andreas et al. 2000). The thermal differences between the ice and ocean tend to form local off-ice winds during still conditions (Chu 1987). These winds are known as sea breezes and also form regularly at coastlines.

The presence of sea ice restricts the transfer of momentum from the atmosphere to the ocean, a process that drives ocean currents (Csanady 2001). At the sea ice edge this restriction is removed causing an increase in atmospheric wind stress upon the ocean away from the sea ice resulting in ocean jets along the sea ice edge (Fennel & Johannessen 1998). These ocean jets are a direct result of the changing atmospheric stress and are not due to the turbulence which causes the jets described in chapter 3. The ocean jets described by Fennel & Johannessen (1998) result in the OML moving rapidly across the ocean surface. The movement of the surface water can cause the up-welling of deeper water to replace it (Quadfasel et al. 1987). Ocean jets can also lead to instabilities resulting in the formation of eddies near the sea ice edge (Smith & Bird 1991).

Ice jet formation at the sea ice edge has been observed. Johannessen et al. (1983) presents a study of sea ice drift using observations from buoys tethered to sea ice floes. These observations are from the sea ice edge and MIZ north of Svalbard in the Arctic Ocean. The sea ice drift is observed to be parallel to the sea ice edge and aligned with strong winds (see figure 1.4). The ice drift at the extreme ice edge is shown to be the fastest with the drift speed decaying into the sea ice pack, reducing by half at 250 km from the sea ice edge. The formation of the jet has not been explained by the physics of the sea ice edge (Feltham (2005) for example, see section 2.3.1) and its possible influence upon the sea ice pack has yet to be explored.

## 1.4 Summary and Thesis Goals

Sea ice and the polar climate are complex and changing systems. The sea ice edge exists at the boundary between the sea ice pack and open ocean and has further influence upon the atmosphere and ocean. Atmospheric jets have been shown to form at coastlines, a comparable boundary between ocean and land. The theory of Hunt et al. (2004) has not previously been applied to the sea ice edge and could provide a physical explanation for the ice jets observed by Johannessen et al. (1983). The process of jet formation is due to

Figure 1.4: Daily average ice drift and surface current from ARGOS drifting buoys, and ship-measured wind on (a) 19 September, (b) 27 September, (c) 28 September, and (d ) 29 September 1979 (taken from Johannessen et al. (1983)).

the changing surface roughness between open ocean and sea ice. Understanding of this process, along with others discussed in chapter 2, is needed to improve the predictions of coupled climate models.

The aim of this thesis is to investigate the formation of atmospheric and oceanic jets at the sea ice edge. The dynamics of the sea ice is analysed to discover what effect jet formation has upon both the sea ice edge and sea ice pack. This is achieved through a modelling study. Methods of sea ice modelling and their application to the sea ice edge and MIZ are discussed in chapter 2.

Jet formation can be driven by a sharp change in surface roughness. This sharp change is apparent at

the sea ice edge. The model of Hunt et al. (2004) is used to investigate atmospheric jet formation at the sea ice edge in chapter 3. Literature on the state of the atmosphere and sea ice surface properties in the MIZ are considered in the calculation of the size and strength of these jets in section 3.2. The model is adapted to create a model of ocean jet formation underneath the sea ice edge and uses literature on the state of the ocean and surface properties of the underside of the MIZ. Only on-ice winds and ocean currents will be investigated. The jet perturbations investigated by Orr et al. (2005*a*) for off-land (or off ice for this thesis) are negative to the wind so have less potential to modify ice drift as slower winds and ocean currents result in a slower sea ice drift (Hibler 1986). Also the dynamical state of a dispersing sea ice edge is continually changing as the sea ice drifts out into the open ocean (Fujisaki & Oey 2011) and does not present a steady state. The steady state condition is essential for the construction of the analytical sea ice model in chapter 4. Mathematical notation used in the thesis is given in table 1 for clarity between the calculations in chapter 3 and 4.

A simplified dynamical sea ice model has been created to model the effects of jet formation upon the state of the sea ice edge. This model is solved analytically and is described in chapter 4 with results in chapter 5. The model shows how the sea ice responds to changes in wind and ocean current speed.

For comparison to the idealised and constrained sea ice edge presented in chapters 4 and 5, a numerical dynamic and thermodynamic sea ice model is used in chapter 6. This model is the Los Alamos sea ice (CICE) model which is used as a component of global climate models (see chapter 2). This model is designed to run on a global scale and has been adapted to focus on the ice edge. A uniform ice edge in a land free domain with a cyclic boundary is used to compare the CICE and analytical sea ice models. Using such a domain allows the model to be run at a high resolution.

The results of this thesis are discussed in chapter 7 and concluded in chapter 8. The results give predictions of winds and ocean currents at the ice edge which lead to predictions of sea ice drift through the analytical and numerical modelling. These predictions are compared to observations of the atmosphere, ocean and sea ice in the MIZ and at the sea ice edge. Global ice conditions and weather patterns are analysed to view areas where jets can form and what role they could play in the polar climate.

# CHAPTER 2

# SEA ICE MODELLING

In this chapter sea ice modelling is introduced. The role of modelling in sea ice and climate science is discussed in section 2.1 and numerical sea ice modelling techniques are introduced in section 2.2. A review of modelling efforts at the sea ice edge is presented in section 2.3 including sea ice, atmospheric, oceanic and coupled models.

---

Sea ice is difficult to observe in situ due to the extreme climate and remote location of the polar regions. Its characteristics on a global scale are also very difficult to recreate in a laboratory. The width of the polar ice caps (1000's of km) is many orders of magnitude greater than its thickness (1-10 m). Detailed observations of sea ice on a global scale are only available since the satellite era (from 1979). This period is of the same scale as many natural variations in global climate patterns so it is difficult to observe clear trends in the development of the sea ice cover due to climate change (Vinnikov et al. 1999, Holland et al. 2008). Partly due to the difficulties in observing sea ice, modelling is essential to the increased understanding of sea ice and its role in the global climate.

Figure 2.1: Arctic September sea ice extent ($10^6$ km$^2$) from observations (thick red line) and 13 Intergovernmental Panel on Climate Change fourth Assessment Report (IPCC AR4) climate models (see table 2.1 for description), together with the multi-model ensemble mean (solid black line) and standard deviation (dotted black line). Inset shows 9-year running means up to 2007. This figure is from Stroeve et al. (2007) modified to include observations up to 2012, see figure 1.2.

## 2.1 Sea Ice in Climate Models

Due to the importance of sea ice in the global climate (see section 1.1) sea ice physics are accounted for by many Global Climate Models (GCMs), see table 2.1. Climate models are compared to observations of global climate to give insight into climate processes and future predictions of climate change (Wang & Overland 2009). The Coupled Model Intercomparison Project (CMIP) is run by the Intergovernmental Panel on Climate Change (IPCC) which takes many modelling efforts from the international scientific community, see table 2.1 for a list of members who contributed to CMIP3 and the fourth assessment report (AR4) in 2007.

The Arctic sea ice extent is observed to be reducing (Maslanik et al. 2011). The IPCC AR4 shows that most models did not capture the speed of reduction in sea ice extent. In particular, the low sea ice extent of summer 2007 was over a standard deviation less than the mean modelled ice extent (see figure 2.1 from Stroeve et al. 2007). The mean ice extent of the GCMs in this figure does not reach the 2007 low for a further 40 years. The low Arctic sea ice extent of 2007 was partially due to the atmospheric conditions (Graversen et al. 2011) with warmer winds from the Pacific increasing the sea ice melt. Also the anomalous anticyclonic wind circulation in the period 2007-2011 has been shown to drive sea ice toward the Fram Strait and out of the Arctic Ocean leading to the low sea ice extent (Ogi & Wallace 2012).

Not all of the models in the CMIP3 have an accurate representation of sea ice physics (Zhang & Walsh 2006, Parkinson et al. 2006), see table 2.1. The climate models from the later CMIP5 are shown to perform better than those in CMIP3 although there is still an inconsistency between the models and rate of decline in Arctic sea ice extent in the models is still less than the observed trend (Stroeve et al. 2012). CMIP5 shows an improvement over CMIP3 in matching the state of arctic sea ice to historical observations due to improvements in the representation of sea ice within the models and a greater effort to tune the models to match observations (Stroeve et al. 2012). The models from CMIP5 on average predict an ice free Arctic summer earlier than the models from CMIP3. There is, however, a similar spread in predictions and thus a similar uncertainty for the future of Arctic sea ice extent in both the projects.

Maslowski et al. (2012) argue that inaccuracies in predicting the decline of Arctic sea ice extent is due to the misrepresentation of climate processes and feedbacks in many GCMs. For example the feedback process where winds and sea ice drift cause the advection of heat from the North Atlantic and Pacific and thus the warming of the Arctic Ocean water mass is often not captured in GCMs (Maslowski et al. 2012). In order to improve the representation of such processes, Maslowski et al. call for higher resolution models, improved coupling and more sophisticated parameterisations within GCMs. In order to achieve this a greater knowledge of sea ice processes is needed along with more observations for validation.

The models in CMIP5 on average show a decrease in Antarctic sea ice extent (Turner et al. 2013), with only 8 out of the 70 ensemble members recreating the observed increase in sea ice extent. The annual variability in sea ice extent of the models is also greater than the observed variability. During the February minimum extent sea ice is typically only found in the Weddell and Bellingshausen Seas either side of

the Antarctic Peninsula (Cavalieri & Parkinson 2008). The majority of CMIP5 models do not correctly reproduce the spatial pattern of minimum sea ice extent (Turner et al. 2013) leading to large relative errors in the minimum sea ice extent. The recent increase in Antarctic sea ice extent has been suggested to be due to a decrease of springtime stratospheric ozone (Turner et al. 2009) leading to the specification that the CMIP5 models include a realistic decline in stratospheric ozone. This inclusion has, however, not resulted in an accurate modelling of Antarctic sea ice extent leading to Turner et al. (2013) commenting that there are "failings in the representation of sea ice in the models or that a real trend in ocean conditions is behind the observed increase of sea ice". Another theory behind the increase in Antarctic sea ice extent is that of Holland & Kwok (2012) who present a data set of Antarctic sea ice drift and atmospheric circulation. The Antarctic sea ice drift is shown to correlate well with winds leading to the conclusion that wind-driven changes in ice advection along with wind-driven thermodynamic changes are the dominant driver of ice-concentration trends. Holland & Kwok (2012) comment that "surface winds and ice dynamics and thermodynamics must be accurately represented" within climate models to capture the recent increase in Antarctic sea ice extent.

The reasons behind climate model inaccuracy are not obvious. The global climate is a complex and chaotic system which, in order to be represented in a numerical model, needs to be simplified. Sea ice models also represent the changing sea ice cover using simplified numerical schemes. These schemes solve equations created by considering physical properties of the sea ice and observed phenomena (Hewitt et al. 2011). The resulting models of sea ice are forced by the atmosphere and ocean and can be run in a number of configurations: a stand alone model forced by observations or a precalculated data set (see section 2.1.2); coupled to an ocean model with both components forced by atmospheric observations (as with Rasmussen et al. (1999) in section 2.3.3); or in a fully coupled climate model (see section 2.1.1).

### 2.1.1 Coupled Modelling

In climate models, the atmosphere, ocean and sea ice are typically modelled in separate numerical components as in the Met Office Hadley Centre General Environment Model (HadGEM) (Collins et al. 2008). These components are coupled together in parameter space, meaning that they share parameters at selected time intervals. For instance the sea ice component is forced using output from the atmosphere and ocean models. This coupling system allows each component to run at a resolution best suited to it, balancing

| Model | Full Name | Sea Ice Physics |
|---|---|---|
| CCCMA CGCM | Canadian Centre for Climate Modelling and Analysis<br>Coupled Global Climate Model | No |
| CNRM CM | Centre National de Recherches Météorologiques (France)<br>Coupled global climate Model | Yes<br>GELATO |
| IPSL CM | Institut Simon Pierre Laplace (France)<br>Climate Model | No |
| MUIB ECHO | Meteorological Institute University of Bonn<br>ECmwf (European Centre for Medium-range Weather Forecasts)<br>HOpe (Hamburg Ocean Primitive Equation) model | Yes<br>Internal |
| MRI CGCM | Meteorological Research Institute (Japan)<br>Coupled General Circulation Model | No |
| UKMO HadGEM | UK Met Office<br>Hadley centre Global Environmental Model | Yes<br>CICE |
| BCCR BCM | Bjerknes Centre for Climate Research (Norway)<br>Bergen Climate Model | Yes<br>NERSC |
| GISS AOM | Goddard Institute for Space Studies (USA)<br>Atmosphere-Ocean Model | No |
| MIROC MedRes | Model for Interdisciplinary Research On Climate (Japan)<br>Medium Resolution version | No |
| MPI ECHAM | Max Planck Institute for meteorology (Germany)<br>ECmwf HAMburg model | Yes<br>Internal |
| NCAR CCSM | National Center for Atmospheric Research (USA)<br>Community Climate System Model | Yes<br>CICE |
| UKMO HadCM | UK Met Office<br>Hadley centre Coupled Model | No |

Table 2.1: Model acronyms from figure 2.1. The sea ice Physics column indicates whether the model considers the geophysics of sea ice. If yes the sea ice component is named. The sea ice components are the Global Experimental Leads and ice for ATmosphere and Ocean (GELATO) based upon the Nansen Environmental and Remote Sensing Center (NERSC) sea ice model. The Los Alamos sea ice model (CICE) is described in section 2.1.2. The sea ice components described as internal have schemes within the ocean model.

model accuracy and computer run time. While the model components can be used to reproduce observed trends within their individual system (see section 2.1.2), coupling the models together permits the various feedback mechanisms between them. For the sea ice this includes the albedo feedback mechanism described in chapter 1

A climate model can be used to test the evolution of global climate in different future scenarios (McLaren et al. 2006). For example to predict the dependance of climate change on the amount of carbon dioxide in the atmosphere. To ensure that the results of these changes are meaningful, the model must first accurately reproduce the current climate and fit well with observations. Such consistency is however not always achieved

(Ann Keen, UKMO Hadley Centre - *personal communication*). Some of the models included within the IPCC AR4 report (see figure 2.1) do not have such accuracy but this was not considered when creating the report and all the data was included (Stroeve et al. 2007).

Accuracy in all the mode components is achieved over the model development process. Test model runs are typically 50-100 years in model time and are performed to test new parameterisation schemes and show how the model performs (Hewitt et al. 2011). Shorter runs are then often repeated with adjusted model parameters that are assumed constant by the model until a realistic reproduction of the the global climate is produced. Parameters often used to tune the model to fit observations are the albedo and density of sea ice (see section 1.1 and Uotila et al. (2012)). This process requires detailed observations of the sea ice cover. Such observations are not readily available (Bitz et al. 2001) and model parameters are often not narrowly constrained (Hunke 2010). When the model is performing well it is matched to the current climate by using what is known as a spin up period. This period is given constant climate conditions and is longer than typical variations in climate (run for 100 model years for example). The spin up allows the modelled climate to approach an equilibrium and remove unnatural initial conditions.

A fully coupled atmosphere - sea ice - ocean GCM is the Met Office Hadley Centre's HadGEM3 model, an evolution of the HadGEM2 model in the IPCC AR4 (see figure 2.1 and table 2.1). This model has been shown to be scientifically credible and is widely used for investigation into the global climate (Hewitt et al. 2011). The atmospheric component is from the Met Office Unified Model. The ocean component is the NEMO model. The sea ice model is the CICE model described in section 2.1.2.

The coupling between the ocean and ice in the HadGEM3 model is through applied stresses from ice drift and ocean currents, freshwater and salinity fluxes, and a thermodynamic balance between the sea surface temperature and the bottom of the sea ice (Hewitt et al. 2011). For coupling with the sea ice-ocean system the atmospheric forcing is first split into the parts acting upon the ice and ocean separately. Atmospheric stresses, rainfall and snowfall are split between the sea ice and the ocean by considering the ice concentration. Heat fluxes and solar radiation levels are the same for both. Forcing for the atmospheric component is created by combining fluxes from the sea ice and ocean. The ocean current and sea ice drift velocities are combined. The sea ice concentration and thickness along with snow thickness is also considered along with the sea surface temperature.

### 2.1.2 Stand Alone Models

Observations of the atmosphere and ocean can be used to force a sea ice model. Such models are used to understand the geophysics of sea ice on a global scale without the added complexity of a fully coupled system. Single component models take less tuning than a fully coupled model and are thus easier to set up and run. A stand alone sea ice model also requires much less computing power than a fully coupled model and can be run on a desktop computer when a low resolution is used (Hunke & Lipscomb 2010). This increases the accessibility of the model as expensive high powered super computers are not required. The focus upon individual processes (such as melt pond formation - see below) allows the use of a standalone model to find errors with a coupled system because problems with the sea ice simulation within a coupled model could be due to the sea ice component not capturing the processes or due to incorrect forcing from the atmosphere and ocean (Ann Keen, *personal communication*).

Due to the ease of setting up and running a stand alone sea ice model it plays a key role in introducing new physics and parameterisations to a GCM. When the model is not coupled to the atmosphere or ocean, feedbacks are eliminated, simplifying the analysis of the impacts of new physics. For example melt pond formation was initially proposed as important feature in the albedo feedback mechanism (Fetterer & Untersteiner 1998, Curry et al. 1995). Melt ponds were investigated in a simple model (Taylor & Feltham 2004) before being parameterised into a numerical stand alone sea ice model (Flocco & Feltham 2007, Flocco et al. 2010). These studies allows for melt ponds to now be considered by a GCM (Flocco et al. 2012), with primary results giving Arctic ice melt that matches observations better than a model which does not consider melt ponds (summer 2007 given as a particular example with ice extent error reduced by 50%).

An example of a sea ice model is the Los Alamos numerical sea ice model (CICE). This model is widely used in GCMs including the HadGEM and NCAR models (see table 2.1 for model names). It is designed to work on a grid covering the entire globe. The model calculates the state of the sea ice from atmospheric and oceanic forcing, considering the thermodynamics and momentum of the sea ice (see Hunke & Lipscomb 2010). The model considers the ice state of Thorndike et al. (1975) (described in section 2.2.1). Thermodynamic changes to sea ice are those of Bitz & Lipscomb (1999) (section 2.2.2) and the dynamics are similar to those of Hibler (1979) (section 2.2.3) using a numerical implementation of the viscous plastic

rheology in appendix A.

## 2.2 Sea Ice Modelling Techniques

Sea ice in a numerical model can be assumed to be continuous (Hunke & Lipscomb 2010). When viewing sea ice on a scale similar to individual ice floe size (1-30 km) the ice appears to be a discrete medium with a vast difference in ice state between the ice floe interior and edges (Lu et al. 2008). At a larger length scale the ice state can be represented as a continuously varying medium by averaging over the floes. Many techniques have been used to make this approximation accurately reproduce the geophysics of sea ice on a global scale (Feltham 2008).

### 2.2.1 The Thickness Distribution of Sea Ice

The thickness of the sea ice cover in most basin scale continuum sea ice models is given by the thickness distribution which evolves according to the thickness distribution equation (Hunke & Lipscomb 2010). This equation balances the state of the sea ice pack against thermodynamic and redistributive modifications (due to sea ice drift causing ridging for example). Thorndike et al. (1975) considers a probability density thickness distribution function $G(h,t)$ which gives the amount of ice of thickness $h$ at time $t$ that occupies a point in Eulerian space. The function is over the unit interval such that integrating from zero ice thickness to the maximum ice thickness $h_{\text{max}}$ gives

$$\int_0^{h_{\text{max}}} G(h)dh = 1,$$

and the result $G(h_{\text{example}}) = 0.6$ means that there is a probability of 0.6 that sea ice that has thickness in the interval $h_{\text{example}}$ to $h_{\text{example}} + dh$ exists at the defined point. The concept of different thickness of sea ice occupying the same point is not physically possible but the continuum is easier to use mathematically. In numerical models the function is solved over discrete gird cells rather than at all points. In this case the result $G(h_{\text{example}}) = 0.6$ means that 60% of the given grid cell is of thickness $h_{\text{example}}$. For a simple numerical model the ice thickness distribution gives two categories for ice thickness, zero thickness (open ocean) and a given greater thickness. As the complexity of a sea ice model is increased, more thickness

categories can be considered.

The rate of thermodynamic change to the ice thickness is given as the ice growth rate $f$. Considering sea ice of thickness $h$ growing at rate $f$ over the time interval $dt$ to a new thickness of $h + dh$ gives the relation $\partial G/\partial t = -\partial/\partial h(fG)$. The redistributive modifications are split into those due to moving ice and mechanical ice deformation such as ridging. Considering the velocity of the ice $\mathbf{u}$ and fluxes of ice in and out of a given region, Thorndike et al. related the time change in thickness distribution to the divergence of the ice flux given as $\nabla \cdot (G\mathbf{u})$. The mechanical modifications are parameterised in a redistribution function $\psi$ giving a governing equation of

$$\frac{\partial G}{\partial t} = -\nabla \cdot (G\mathbf{u}) - \frac{\partial}{\partial h}(fG) + \psi. \tag{2.2.1}$$

The function $\psi$ models how the ice deforms under compression, tension and shear forces. Pressure ridging for example, increases the ice thickness (Bourke & Garrett 1987).

Alternatively the ice concentration can be modelled alongside the thickness distribution. The ice concentration $A$, can be modelled as a non - dimensional variable with $0 \leq A \leq 1$ where $A = 0$ is for open ocean, and $A = 1$ is for a complete ice cover. This method can be compared to the thickness distribution with $1 - A = G(0)$. Gray & Morland (1994) introduce a model of the ice thickness and concentration in multi floe pack ice which balances mass along with more specific modifications with

$$\begin{aligned} \frac{\partial A}{\partial t} + \mathbf{u} \cdot \nabla A + A\xi\{1 - \alpha^I H(-\xi)\} &= \frac{k^I}{\rho_I}, \text{ and} \\ \frac{\partial h}{\partial t} + \mathbf{u} \cdot \nabla h + h\xi\alpha^I H(-\xi) &= q^I - b^I. \end{aligned} \tag{2.2.2}$$

The divergence of the horizontal velocity field $\xi = \frac{\partial u_i}{\partial x_i}$ is considered along with $\alpha$, the ratio of vertical flux of ice redistribution through ridging to the horizontal flux of ice implied by the horizontal velocity field. When the ice converges ridging causes an increase in thickness through $h\xi\alpha H(-\xi)$ and a decrease in concentration through $A\xi\{1 - \alpha H(-\xi)\}$. $H$ is the Heaviside step function (with $H(x \leq 0) = 0$ and $H(x > 0) = 1$) which makes the ridging irreversible. Thermodynamic modifications are separated into $k^I$ the mass transfer to ice from the water in the leads, $q^I$ the volume flux of surface accumulation and $b^I$ the

volume flux of basal melt. $\rho_I$ is the density of sea ice.

### 2.2.2 Thermodynamics

To calculate thermodynamic changes to sea ice the thermal and salinity characteristics need to be considered. This is done across the vertical profile of the sea ice. Bitz & Lipscomb (1999) presented a model of the thermodynamics of sea ice where the temperature profile is governed by the modified heat equation

$$\rho c_T \frac{\partial T}{\partial t} = \frac{\partial}{\partial z} k_B \frac{\partial T}{\partial z} + \kappa I_0 e^{-\kappa z},$$

where $c_T$ the thermal capacity, $T$ the temperature at vertical position $z$ and $k$ the conductivity of the sea ice. $I_0$ is the solar radiation that penetrates the upper surface of the ice cover with $\kappa_B$ the extinction coefficient in Beer's law. The thermal capacity $c_T$ and the conductivity $k$ are given as functions of temperature and salinity and consider the effects of brine pocket formation within the ice. The model is specifically designed to balance energy leading Bitz & Lipscomb to state that solving the equation continuously through the vertical profile of the sea ice is essential. This is achieved by splitting the ice into several layers and solving the equations of state for each layer. An extra layer of snow is added to the top of the sea ice.

At the upper surface of the sea ice radiation and sensible and latent heat from the atmosphere are considered. These can alter temperature of the sea ice and cause ice growth or melting. The growth and melting of sea ice is dependent upon $q$, the energy of melting of sea ice, a function of the ice temperature and salinity. This function is analogous to the enthalpy per unit volume of the sea ice with

$$q(S,T) = \rho_I c_{Io}(T_m - T) + \rho_I L_o \left(1 + \frac{\mu_m S}{T}\right),$$

where $c_{Io}$ is the heat capacity, $L_o$ is the latent heat of fusion of fresh ice and $\mu$ is an empirical constant relating the melting temperature $T_m$ and salinity $S$ of sea ice wih $T_m = -\mu_m S$. The lowest layer of the sea ice grows or melts to hold the bottom surface of the sea ice at the freezing point of sea water.

Bitz & Lipscomb use a prescribed salinity profile for their model which has fresh ice at the surface due to contact with snow which is assumed to be fresh. The salinity increases with depth using a least

squares fit to observations. The salinity of the ice in contact with the ocean is assumed to be at $3.2‰$(Bitz & Lipscomb 1999).

### 2.2.3 Sea Ice Dynamics

The movement of sea ice as a continuum can be modelled using a momentum balance. The simplest consideration of sea ice dynamics is that of free drift. Assuming a low ice concentration removes the importance of ice floe interaction towards the ice drift. The momentum of the drifting sea ice can thus be accounted for by applied stresses giving a momentum balance of

$$m(\frac{\partial \mathbf{u}}{\partial t} + \mathbf{u} \cdot \nabla \mathbf{u}) = -mf_c \mathbf{k} \times \mathbf{u} + \tilde{\boldsymbol{\tau}}^a + \tilde{\boldsymbol{\tau}}^o, \tag{2.2.3}$$

where $m$ is the mass of the sea ice, $\mathbf{u}$ is the velocity vector of the sea ice drift (giving the left hand side of the equation as the rate of change of momentum), $f_c$ is the Coriolis parameter and $\tilde{\boldsymbol{\tau}}^{\boldsymbol{a}}$ and $\tilde{\boldsymbol{\tau}}^{\boldsymbol{o}}$ are applied stresses from the atmosphere and ocean. This momentum balance is used for many models of sea ice drift at the sea ice edge (for example Chu 1987) which are discussed in section 2.3.1.

The momentum balance used in the analytical model described in chapter 4 considers both the sea ice and ocean. It was developed by Gray & Morland (1994) by considering the surface layer of the ocean. The sea-ice ocean mixture layer contains the ice floes and the ocean between them down to the depth of the floes. The interactions between the ice floes and the ocean between them is described as a continuum, over a length scale greater than individual floe dimensions. The momentum balance for the sea ice and ocean mixture layer is constructed by considering momentum balances for both the ice and the ocean, and integrating over the layer. The rate of change of momentum of the layer is balanced by

$$m(\frac{\partial \mathbf{u}}{\partial t} + \mathbf{u} \cdot \nabla \mathbf{u}) = -mf_c \mathbf{k} \times \mathbf{u} + A\tilde{\boldsymbol{\tau}}^a + A\tilde{\boldsymbol{\tau}}^o + \mathbf{S} + \nabla \cdot \boldsymbol{\sigma}, \tag{2.2.4}$$

where $\mathbf{u}$, $f_c$, $\tilde{\boldsymbol{\tau}}^{\boldsymbol{a}}$ and $\tilde{\boldsymbol{\tau}}^{\boldsymbol{o}}$ are as described for the free drift momentum, $m$ is the mass per unit area of the mixture layer, $\mathbf{S}$ is the ocean surface tilt force and $\boldsymbol{\sigma}$ is the ice stress tensor.

The applied stresses in the balance are dependent upon the ice concentration $A$. The ice concentration

dependance applies the external stresses to only the ice in the layer. The internal stresses are derived from a sea ice rheology. A rheology is a description of how a medium deforms or moves under the influence of external stresses, for example the viscous plastic rheology described in appendix A. Sea ice is constantly moving and deforming due to winds and ocean currents so a mathematical description of its rheology is essential for modelling efforts. In a large scale numerical model the sea ice rheology is linked to the formation of leads and pressure ridges. For instance the CICE model records the distribution of ridged ice which alters the thickness distribution of the ice pack.

## 2.3 Models of the Sea Ice Edge

The sea ice edge and MIZ have been been considered in modelling studies. The characteristics of this region are unique and present a physical system of particular interest. The sea ice edge can be viewed as a step change along a straight boundary. This easily allows for the creation of an idealised domain with one horizontal dimension extending from the open ocean to the sea ice pack.

### 2.3.1 Sea Ice Models

The sea ice within the MIZ is often observed to be in a different state to the sea ice within the ice pack (smaller floe size for example, see section 1.3). The dynamics of sea ice when in this altered state have been considered in many modelling studies. Simple models of free drifting ice have successfully predicted the movement of sea ice with a low concentration. The natural divergence of the sea ice edge can be accounted for by free drifting ice driven by an off-ice sea breeze formed by the thermal changes in the atmosphere (Chu 1987). The free drifting movement of ice away from the ice pack can lead to ice bands. Fujisaki & Oey (2011) use a coupled free drifting ice and ocean model to investigate the formation of ice bands at the sea ice edge. The band formation is shown to be driven by the stresses between the atmosphere, ocean and ice rather than floe collisions or other ice stresses.

Non free drifting ice has also been considered. Adding complexity to the ice movement has been achieved by considering internal ice stresses due to plasticity (Lepparanta & Hibler 1985), internal ice pressure (Flato & Hibler 1989) and floe collisions (Lu et al. 1989) leading to a granular rheology (Feltham 2005).

Lepparanta & Hibler (1985) applied the viscous plastic rheology of Hibler (1979) (as described in appendix A) to an idealised ice edge. Numerical and analytical solutions were investigated in order to see how the ice motion is driven by internal stresses and, in particular, if the sea ice jets observed by Johannessen et al. (1983) (see figure 1.4) can be explained by viscous-plastic sea ice deformation. Lepparanta & Hibler argue that ice jets are unlikely to form due to ice dynamics and a coupling between the ice, atmosphere and ocean is required.

In accordance with observations of sea ice dynamics, an internal ice pressure in the MIZ has been considered by Flato & Hibler (1989). Internal pressure resists compression of the sea ice cover by modelling the sea ice as a cavitating fluid. This method describes the sea ice as a two-phase system, sea ice in free drift, and sea ice which resists compression when its compactness has reached a certain threshold. This is done in a numerical model on an idealised grid of the ice and MIZ. The internal ice pressure is shown to disperse the ice edge and restrict the unrealistic ice build up observed in pure free drift models despite the dispersion component of the momentum balance being small compared to wind and ocean current stresses.

The MIZ typically contains little compressive ice deformation such as ridges leading to the assumption that the internal ice stress is due to floe collisions. Shen et al. (1987) develops a regime based upon a system of ice discs floating in the ocean. These discs randomly collide and their kinetic energy is dissipated. This dissipation is considered along with the averaged velocity and separation of the discs to calculate the internal stresses of the sea ice pack. The stress regime is shown to be dissimilar to a viscous plastic rheology. The study of Lu et al. (1989) compares sea ice in the MIZ with no internal stress regime (free drifting), a collisional rheology and a viscous plastic rheology in a numerical model on an idealised grid. When applied to the MIZ and sea ice edge the free drifting and collisional sea ice have velocities that are almost parallel to the applied wind field that is either on-ice, off-ice or parallel to the sea ice edge. The viscous plastic regime gives sea ice drift with a greater turning angle against the applied forcing due to the internal ice stress. A collisional rheology for sea ice is mathematically complex and numerical solving techniques are essential for its use.

Furthermore, sea ice can be treated as a two dimensional granular medium even if collisions are unimportant. This has been considered in the sea ice pack by Shen et al. (1986) and at the sea ice edge by Feltham (2005). Granular dynamics considers the floe or grain size distribution, the random motion and kinetic en-

ergy of the grains or their granular temperature and the friction between the grains. Feltham (2005) used boundary layer theory for the extreme ice edge to show how granular dynamics can lead to jet formation. This jet formation is on a small scale (over approximately 1 km) compared to the extent of the MIZ (typically 100 km). Feltham showed that the collisional stresses are only significant over the length scale of the jet when the ice concentration is low, and not over the MIZ zone width.

The stress regimes described here are all isotropic. An isotropic medium deforms in the same way in all directions. Observations of sea ice, for instance long kinematic features, imply that sea ice has a directional memory and deforms anisotropicaly. There has yet to be a dedicated study of anisotropy at the sea ice edge, although an anisotropic sea ice rheology has been developed (Tsamados et al. 2012).

The role of wave-ice interation in the MIZ has been widely studied as discussed in section 1.3. Models of this interaction have been created (for example Kohout & Meylan 2008). Details of this modelling process will not be included in this summary due to their complexity. Wave interaction plays a large role in this thesis as it accounts for the smaller ice floes and increased form drag in the MIZ (Birnbaum & Lupkes 2002). The formation of atmospheric or oceanic jets could possibly increase the wave size in the MIZ and cause the breaking of sea ice floes and an increase in applied drag coefficients through form drag (Birnbaum & Lupkes 2002). The parameterisation of Birnbaum & Lupkes (as discussed in section 2.3.2) shows that the increase in drag will be small and would only create a small increase in jet strength. Any link between wave interaction and jet formation will not be investigated as other processes are more important (ice drift speed for example). The increase in drag is assumed to be constant in time and the thesis focusses upon jet formation and sea ice dynamics.

During freezing events the sea ice pack increases in size. The formation of new ice takes place at the sea ice edge and in the MIZ. Pedersen & Coon (2004) model amounts of pancake and frazil ice formed in the MIZ of the Greenland Sea. Ice concentration data from satellite observations and wind speed data from the ECMWF are used to calculate the sea ice drift and areas of ice growth and melting. Known characteristics of frazil and pancake ice allow for the modelling of the state of the new ice, its thickness, concentration and salinity. The MIZ is shown to have a great extent during freezing events, with a complex and developing ice profile as the different forms of new ice are redistributed causing melting or consolidation into pack ice.

### 2.3.2 Atmosphere and Ocean Models

Models of the atmosphere above the sea ice edge have been produced. These models give further insight into observations and investigate links between atmospheric processes and the changing sea ice cover. Observations of the atmosphere from the Earth's surface or from aircraft are often incomplete in time and space. Vihma & Brummer (2002) match observations of wind speed, temperature and humidity to a dynamic atmosphere modelling the wind speed, air temperature and humidity. The model is applied to the atmosphere over the sea ice edge through its representation as a step change in surface temperature. The model balances changes in momentum, potential temperature, water vapour mixing and sensible and latent heat, and gives the state of the atmosphere up to 800 m above the Earths surface. Both on-ice and off-ice winds are considered, giving a stable Atmospheric Boundary Layer (ABL) in both cases and low level jet formation for on-ice winds.

The ABL over the MIZ has been considered in fully theoretical models. Kantha & Mellor (1989), Glendening (1994) and Tisler et al. (2008) use similar balance laws to Vihma & Brummer (2002) over a laterally invariant sea ice edge. This allows the use of one horizontal dimension along with the vertical. The models are numerical with 2 km horizontal resolution and variable vertical resolution to give greater accuracy (5 m resolution) at the Earth's surface and at the top of the ABL. The boundary conditions for the models are from geostrophic winds above and surface conditions below the ABL and the model is initialised with expected atmospheric conditions. Kantha & Mellor use prescribed geostrophic winds to test on-ice and off-ice winds conditions. Glendening calculates the strength of the geostrophic winds within the ABL model. The conditions set by Tisler et al. are more sophisticated using the output from an Arctic wide atmospheric model (the HIgh Resolution Limited Area Model) to focus upon the MIZ north of the Fram Strait and to correlate the results with observations of the ABL. The surface conditions in the models are prescribed assuming a stationary sea ice edge with a step change in surface roughness and temperature conditions. Tisler et al. use more sophisticated temperature conditions considering the thermal properties of sea ice and any snow on top of it.

The results of these models show the importance of ice edge location toward the state of the ABL. There is often a step change in atmospheric conditions such coastal fronts or cloud formation at the sea ice

edge. Kantha & Mellor and Tisler et al. focus upon the thermal conditions of the ABL so are not of direct importance to this thesis, however the modeling techniques, in particular the use of a laterally invariant system has direct parallels to the methods used in chapters 3 and 4. Glendening analyses the changing direction of the geostrophic winds upon the ABL formation of the sea ice edge. Atmospheric jets are shown to form, although they are of a different structure to the calculations in chapter 3.

A three dimensional model of the ABL has been used by Liu et al. (2006). This model is the Cloud Resolving Storm Simulator (CReSS) developed at Nagoya University and is applied to the MIZ to observe cloud formation. Application to the MIZ is performed by using differing surface roughness lengths. Sea ice is given a higher surface roughness (0.001 m) than the open ocean (roughness dependant upon wind speed and approximately 0.0001 m). As the model is of high resolution (500 m grid cells) and has two horizontal dimensions the MIZ can be represented by a mixture of sea ice and open ocean grid cells. The sea ice state is fixed. The model gives a detailed image of cloud formation during off-ice winds.

The surface conditions in the previously mentioned models are given as a step change between the ocean and sea ice. The MIZ is observed to develop over large distances into the sea ice pack (Lu et al. 2008) so this method could be seen to be inaccurate. Birnbaum & Lupkes (2002) present a parameterisation of surface drag over the MIZ that considers ice floe size and concentration. The surface drag is made of skin drag from the flat top of the ice floes and ocean surface, form drag from the vertical edges of the floes and turbulence around the ice floes. This parameterisation is used in a simple model of the ABL similar to that of Kantha & Mellor (1989). The surface stress to the atmosphere is given as a function of frictional velocity (dependant upon surface turbulence and skin drag) and form drag inversely weighted by the ice concentration. The improved drag laws give a better fit with observations of surface wind stress and allow the state of the ABL (density and wind direction in particular) to alter the surface stress.

The ocean mixed layer underneath the MIZ and sea ice edge has also been modelled. Markus (1999) uses a mixed layer model of the of the southern ocean forced from below by the deep ocean temperature and salinity and from above by atmospheric wind speed and temperature, cloud conditions, sea ice concentration and the thickness of the snow upon it. The model has a resolution of 25 km and considers the mixed layer and single layer of variable depth (known as a bulk model). Within the mixed layer the temperature, salinity and layer depth are balanced with various temperature and turbulent fluxes. As with the atmospheric models,

this model shows that the state of the ocean mixed layer is very sensitive to the location of the sea ice edge.

A more complex mixed layer which varies with depth is considered in the analytical model of Fennel & Johannessen (1998). This model looks at the ocean response to atmospheric stress modified by the presence of the sea ice edge. Caclulations are performed over a one dimensional laterally invariant sea ice edge giving analytical solutions for the ocean velocity beneath. Several different ice edges are considered with differing stress characteristics and ice drift speeds. The model predicts ocean jet formation due to the sharp change in applied stress from the atmosphere to the ocean due to the presence of sea ice.

### 2.3.3 Coupled Systems

Due to the feedback mechanisms between the ocean, ice and atmosphere they are often modelled in a coupled system. The simplest of such models is that of Roed & O'Brien (1983). This model uses a bulk ocean mixed layer model similar to that of Markus (1999) along with a dynamic sea ice model similar to Hibler (1979) but with a simplified rheology. The system is over one dimension with a laterally invariant sea ice edge. The ice and ocean are coupled using a stress regime that considers both the ice to ocean interface below and atmosphere to ice or ocean interface above. The model is forced by atmospheric stresses and shows how upwelling of water into the mixed layer is a result of ice and ocean movement as a coupled system.

This two layer system has been extended to two dimensions by Smith & Bird (1991) to investigate the formation of eddies along the sea ice edge. The momentum balance of the ocean mixed layer is coupled to a free drifting ice edge (as described in equation (2.2.3)) using an sea ice to ocean interface stress regime similar to that of Roed & O'Brien (1983). The model is solved numerically with a resolution of 2 km. The domain used allows for different slopes on the ocean floor and different prescribed vorticity rates in the mixed layer. Large eddies (10-100 km in diameter) are shown to form and travel along the sea ice edge pulling the ice out into the open ocean through the applied oceanic stress.

The coupling of ice and ocean has been expanded to the entire ocean depth rather than just the mixed layer. Rasmussen et al. (1999) present a full three dimensional ocean model of the basin between Greenland, Iceland and Norway forced by observed atmospheric conditions. The model balances mass, salinity and temperature profiles with the ocean velocity and pressure. The sea ice above is modelled with the viscous-plastic scheme described by Lu et al. (1989). The model is numerical and has a 20 km horizontal resolution

and a 50 m vertical resolution. The coupling between the ice and ocean is done by equating surface shear stresses and a thermodynamic and salinity balance in the ocean mixed layer. Due to complex bathymetry of the non- idealised domain the model required a spin up period using just the ocean component. The study shows the importance of ice-ocean coupling toward the modelling of salinity and temperature profiles.

### 2.3.4 Summary

In this chapter many modelling methods have been presented. To investigate the jet formation described by Hunt et al. (2004) atmospheric and oceanic models are described in the next chapter. The atmospheric model used by Hunt et al. is not as complex as the atmospheric models described in section 2.3.2 as it is a bulk model of the ABL which only considers wind speed perturbations. To apply this model to the sea ice edge the atmospheric drag over sea ice needs to be investigated for which the study of Birnbaum & Lupkes (2002) is of particular interest. To apply the theory of jet formation to the ocean mixed layer a bulk model which considers perturbations to the ocean current is required. The model of Roed & O'Brien (1983) is similar to the oceanic model required.

To investigate the effect that jet formation has upon the sea ice edge a dynamic sea ice model is described in chapter 4. This model needs to be able to calculate the sea ice drift due to applied stress from the ocean and atmosphere and be applied to the sea ice edge. The consideration of ice concentration within the momentum balance of Gray & Morland (1994) makes it ideal for this task. The sea ice edge can be given as the locus of points of zero ice concentration. To use this momentum balance a rheology is required to calculate the internal ice stresses. Gray & Morland use the viscous plastic rheology of Hibler (1979) in their study. The alternate collisional and granular rheologies discussed in section 2.3.1 are not shown to give a better description of ice dynamics within the MIZ and are mathematically complex to use (Lu et al. 1989, Shen et al. 1986, Feltham 2005). The viscous plastic rheology shall be used along with free drift dynamics for low ice concentrations. This allows comparison with numerical sea ice models which use this same rheology (such as the CICE model).

# CHAPTER 3

# ATMOSPHERIC AND OCEANIC JET FORMATION

An application of the theory of Hunt et al. (2004) (*Coriolis effects in mesoscale flows with sharp changes in surface= conditions*) to the sea ice edge is presented in this chapter. The theory and modelling of atmospheric jet formation is described in section 3.1 and appied to the sea ice edge using observations of the ice cover and atmosphere in the marginal ice zone. The theory of jet formation is adapted for application to the ocean underneath the ice cover in section 3.2 using observations of the ocean and ice cover in section 3.2.4.

---

The formation of atmospheric jets has been modelled over coastlines (Hunt et al. (2004), hereafter known as HORC). This formation is due to the Coriolis effect on flows over a sharp change in surface roughness. The jets are able to form during low Froude number flows in a stably stratified atmosphere. The Froude number condition is discussed in section 3.1.4 and the stratification of the atmosphere over the sea ice edge is shown to be stable in section 1.3. The sharp change in surface roughness is present in the Marginal Ice Zone (MIZ). The change in roughness is present for the atmosphere flowing from the open ocean to the rough broken sea ice, and also for ocean flowing underneath the sea ice. The calculations of HORC are applied to winds over the MIZ and the theory is adjusted to represent the ocean flowing underneath it.

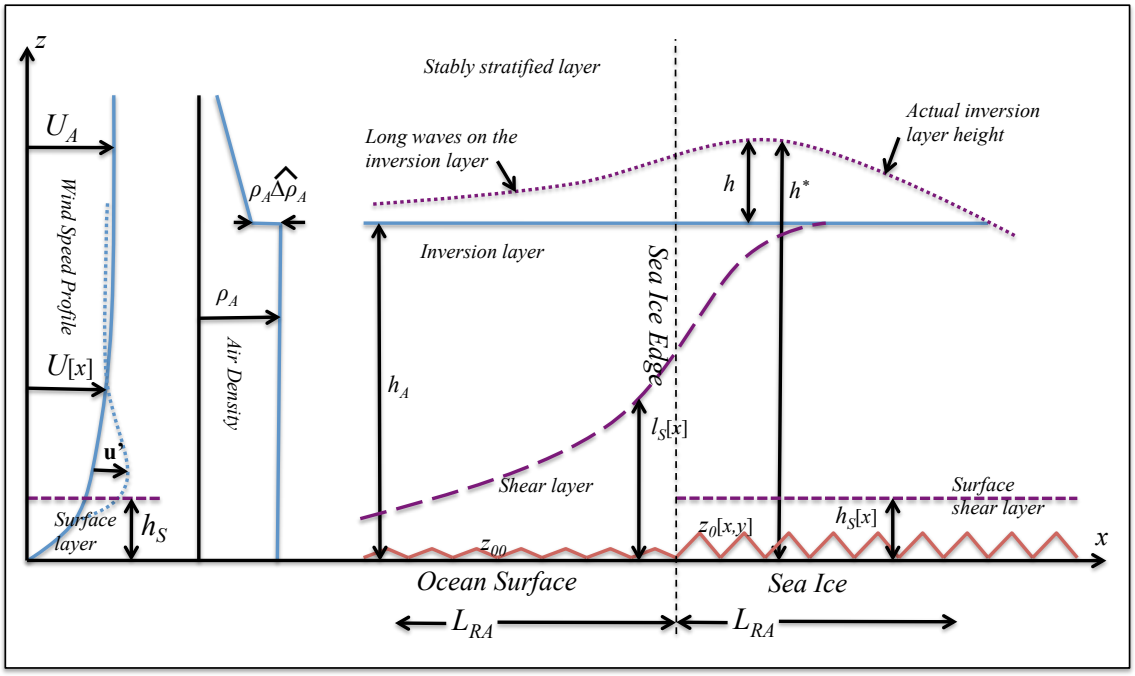


Figure 3.1: Vertical profile of the Atmospheric Boundary Layer with velocity ($U[x]$ and perturbation $\mathbf{u}'$) and density ($\rho_A$) as a shallow layer perturbed flow.

## 3.1 Atmospheric Jets

The theory of HORC is explained (section 3.1.1) and applied to the sea ice edge. Characteristic values for the winds and ice edge are derived and used to calculate the jet size and shape (section 3.1.4). Mathematical notation for this chapter is explain below and listed in table 1.

### 3.1.1 Shallow-Layer Model Equations

Figure 3.1 illustrates the shallow layer flow over a sharp change in surface roughness. An atmospheric flow of speed $U_A$ approaches a change in surface roughness length from $z_{00}$ to $z_0$. There is a lower layer of thickness $h_A$. This layer has density $\rho_A$ and is known as the Atmospheric Boundary Layer (ABL). A step change in air density of magnitude $\rho_A\widehat{\Delta\rho_A}$ (where $\widehat{\Delta\rho_A}$ is the non-dimensional part) exists between the ABL and the upper atmosphere with the ABL of higher density. $\Delta g_A = g\widehat{\Delta\rho_A}$ is the reduced gravitational

acceleration of the flow. Upwind conditions at $x \to -\infty$ are assumed to be steady and uniform in the horizontal plane. The mean velocity profile is $U[z]$, $V[z]$, shear Reynolds stresses (the vertical variation of horizontal turbulence stress) are $(-\overline{u"w"})_0$, $(-\overline{u"v"})_0$, pressure profile is $P[z]$ and density is $\rho_A\rho[z]$ (note that double prime indicates turbulent fluctuations). The development of the flow is modelled using perturbations to the mean values. These are given as $u'$, $v', w'$ for velocity, $\Delta(-\overline{u"w"})[z]$, $\Delta(-\overline{u"v"})[z]$ for Reynolds stresses, and $p$ for pressure, and are assumed to be uniform over the lower layer. The inversion layer height $h_A$ and its perturbation $h$ are also considered in the model. The scaling values for the flow are the Froude number $\mathcal{F}_A = U_A/\sqrt{\Delta g_A h_A}$, and the atmospheric Rossby radius $\mathcal{L}_{RA} = \sqrt{\Delta g_A h_A}/f_c$ where $f_c = 2\Omega \sin\theta$ is the Coriolis parameter for latitude $\theta$ and the Earth's rotational speed $\Omega$.

The change in roughness length $z_0$ creates a shear surface layer of thickness $h_s$. The shear layer depth $l_s$ increases in the direction parallel to the wind over the change in roughness. For subcritical flows where $\mathcal{F}_A < 1$, turbulent effects cause this change to be transferred to the inversion layer height $h^*$ over a horizontal distance of over 10 km. This structure has been observed over the MIZ (Kantha & Mellor 1989, Tisler et al. 2008) and has been reproduced by high resolution atmospheric models (Kantha & Mellor 1989). This model of the ABL is valid for all subcritical flows with $\mathcal{F}_A < 1$ and is unable to give solutions for supercritical flows with $\mathcal{F}_A > 1$. The possibility of atmospheric jet formation for supercritical flows is not conclusive from this theory.

The components of the linearised momentum balance for the perturbations to the flow field are given as

$$\begin{aligned} Du' =& -p_x + f_c v' + F[x, y, t] \text{ and} \\ Dv' =& -p_y - f_c u' + G[x, y, t], \end{aligned} \tag{3.1.1}$$

where $D = \partial/\partial t + U_A \partial/\partial x$ is the total derivative, $F$ and $G$ are the along and across effective body forces determined by the vertical gradient of turbulent shear stress or by buoyancy forces.

The vertical perturbation velocity, $w'$, at the inversion and the perturbation to the inversion height, $h$, are linked to $\bar{u}$ and $\bar{v}$, the horizontal perturbation velocities $(u', v')$ averaged over the lower layer, using the continuity equation so that at $z = h_A$

$$Dh = w[z = h_A] = -(\bar{u}_x + \bar{v}_y)h_A. \tag{3.1.2}$$

The horizontal gradients of the pressure perturbation are given by HORC (through the linearisation of pressure fluctuations) as a function of $h$ with

$$p_x = \Delta g_A h_x \text{ and } p_y = \Delta g_A h_y. \tag{3.1.3}$$

Equations (3.1.1) and (3.1.3) can be combined with $(\bar{u}, \bar{v})$ and the body forces averaged over the layer $(\overline{F}, \overline{G})$ to give

$$\begin{aligned} D\bar{u} &= -\Delta g_A h_x + f_c \bar{v} + \overline{F} \text{ and} \\ D\bar{v} &= -\Delta g_A h_y - f_c \bar{u} + \overline{G}. \end{aligned} \tag{3.1.4}$$

Equations (3.1.2) and (3.1.4) can be combined to give an equation to be solved for $h$ with

$$D\left[\nabla^2 h - \frac{h}{\mathcal{L}_{RA}^2} - \frac{\mathcal{F}_A^2}{U_A^2} D^2 h\right] = \mathcal{F}_A \frac{h_A}{U_A}\left[\frac{1}{\mathcal{L}_{RA}}(\overline{G}_x - \overline{F}_y) + \frac{\mathcal{F}_A}{U_A} D(\overline{F}_x + \overline{G}_y)\right]. \tag{3.1.5}$$

For the steady state $(\partial/\partial t = 0)$ this equation can be integrated in the $x$ direction and scaled to give

$$\widehat{\nabla}^2 \widehat{h} - \mathcal{F}_A^2 \widehat{h}_{XX} - \widehat{h} = \widehat{R}[X, Y] \tag{3.1.6}$$

where

$$\begin{aligned} \widehat{R}[X, Y] &= (\pm) \int_{\mp\infty}^{X} (\widehat{G}_X - \widehat{F}_Y)[X'] dX' + \mathcal{F}_A(\widehat{F}_X + \widehat{G}_Y) \\ &= \widehat{R}^{(0)} + \mathcal{F}_A \widehat{R}^{(1)}, \end{aligned} \tag{3.1.7}$$

with $(\widehat{F}, \widehat{G}) = (\mathcal{L}_{RA}\mathcal{F}_A/U_A^2)(\overline{F}, \overline{G})$. The sign of the integral and the limit of integration relate to the choice of constant of integration to achieve a definite integral. The scaling is done horizontally over the Rossby radius $(\mathcal{L}_{RA})$ and vertically over the lower layer $(h_A)$ with $\widehat{h} = h/h_A$, $(X, Y) = (x, y)/\mathcal{L}_{RA}$ and $\partial/\partial X = \mathcal{L}_{RA}\partial/\partial x$. The forcing function $\widehat{R}[X, Y]$ is split into a series in the Froude number. This allows the system to be solved for the leading order, $\widehat{R}^{(0)}$, and first order, $\widehat{R}^{(1)}$, forcing functions.

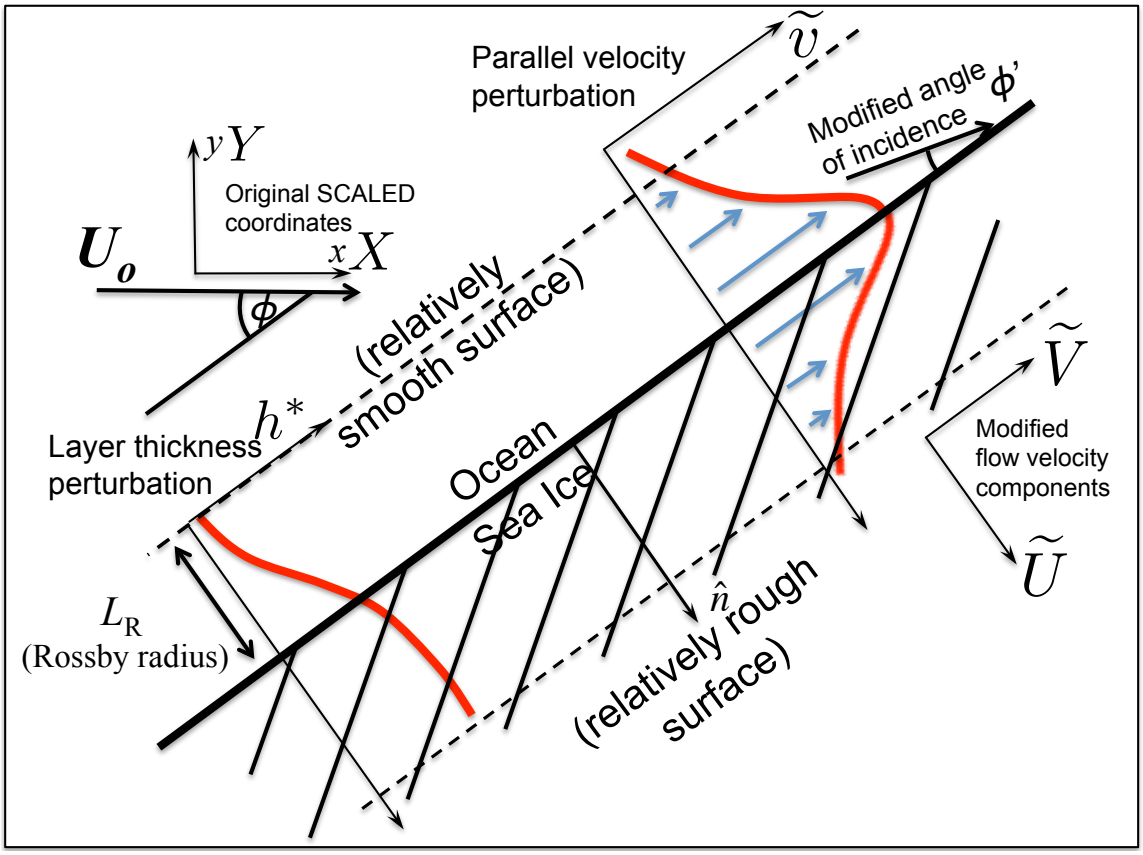


Figure 3.2: Shallow surface layer flow over a sharp change in surface roughness at angle $\phi$ to the flow. The sharp change in surface roughness modifies the layer thickness and flow velocity at right angles to change in roughness. This modifies the flow direction to be at angle $\phi'$.

Equations (3.1.2) and (3.1.4) can also be combined to give $(\widehat{u},\widehat{v}) = (\bar{u},\bar{v})/U_A$ in terms of $\widehat{h}$ with

$$\begin{aligned} \widehat{u}_{XY} + \frac{\widehat{u}_X}{\mathcal{F}_A} &= -\left(\frac{\partial}{\partial Y} + \mathcal{F}_A\right)\frac{\widehat{h}_X}{\mathcal{F}_A^2} + \frac{\widehat{F}_Y}{\mathcal{F}_A} \text{ and} \\ \widehat{v}_{XX} - \frac{\widehat{v}_Y}{\mathcal{F}_A} &= -\left(\frac{\partial}{\partial Y} - \mathcal{F}_A\right)\frac{\widehat{h}_X}{\mathcal{F}_A^2} + \frac{\widehat{G}_X}{\mathcal{F}_A}. \end{aligned} \tag{3.1.8}$$

### 3.1.2 Forcing

The body forces $(F, G)$ and the averaged and scaled functions $(\widehat{F}, \widehat{G})$ are dependent upon surface drag, elevation change and heating and cooling effects. This thesis focuses upon the surface drag. These components

are equal to the vertical gradients of the perturbation shear stress terms, $\partial(-\overline{u'w'})/\partial z$ and $\partial(-\overline{u'v'})/\partial z$. These terms are parameterised using the perturbation functions $\Delta C_F$, $\Delta C_G$ with

$$\begin{aligned}\overline{F} &= -\frac{\Delta C_F U_0^2}{h_A} \text{and} \\ \overline{G} &= -\frac{\Delta C_G U_0^2}{h_A}.\end{aligned} \tag{3.1.9}$$

In the along-wind direction the perturbation $\Delta C_F$ is given as

$$\Delta C_F = \Delta_0[z_0] + \Delta_u[\bar{u}], \tag{3.1.10}$$

where $\Delta_0 \approx \kappa^2\{1/\ln^2(h_S/z_0) - 1/\ln^2(h_S/z_{00})\}$ is dependent upon the change in roughness length. For large changes in surface roughness, where $z_0 >> z_{00}$, $\Delta_0 \approx \kappa^2/\ln^2(h_S/z_0)$, where $\kappa(\approx 0.4)$ is von Kármán's constant. $\Delta_u = C_F(2\bar{u}/U_A - h/h_A)$, is dependent upon the velocity perturbation, with $C_F = \kappa^2/\ln^2(h_S/z_{00})$. Through scaling HORC shows how the velocity dependent component ($\Delta_u$) can be neglected for typical mesoscale atmospheric flows over sharp changes in surface roughness. The drag coefficient in the across wind direction is given as $\Delta C_G \approx C_F\bar{v}/U_0$, shown by HORC to be insignificant compared to the along wind drag. This simplifies the calculations.

To model the interaction between the atmospheric flow and the sea ice edge, the forcing functions ($\Delta C_F, \Delta C_G$) are given as step functions using the Heaviside Step function $\mathcal{H}[\widehat{n}]$ and its derivative the Dirac Delta function $\delta[\widehat{n}]$ (as shown in *Roughness boundaries at arbitrary angle to the wind* - HORC section 3(c)). These step functions depend on the angle ($\phi$) between the ice edge and the ocean current, see figure 3.2, giving

$$\Delta C_F = \{\Delta C_F\}\mathcal{H}[\widehat{n}], \tag{3.1.11}$$

where $\widehat{n} = (x\sin\phi - y\cos\phi)/\mathcal{L}_{RA}$ is the non-dimensional distance normal to the ice edge and $\{\Delta C_F\}$ is the magnitude of $\Delta C_F$. In order to solve equation (3.1.6), equations (3.1.9) and (3.1.11) are combined. As the forcing components $\widehat{R}^{(0,1)}$ both experience a step change at the same location the calculations can be

simplified through their relation to the same function $\Phi[X,Y]$ where

$$\begin{aligned}\Delta C_F =& \{\Delta C_F\}\Phi_X[X,Y],\\ \widehat{F} =& -\widehat{\Delta C_F}\Phi_X[X,Y],\\ \widehat{R}^{(0)} =& \widehat{\Delta C_F}\Phi_Y[X,Y] \text{ and}\\ \widehat{R}^{(1)} =& -\widehat{\Delta C_F}\Phi_{XX}[X,Y],\end{aligned} \tag{3.1.12}$$

with $\widehat{\Delta C_F} = \{\Delta C_F\}\mathcal{L}_{RA}\mathcal{F}_A/h_A$. Setting $\Phi_X[X,Y] = \mathcal{H}[\widehat{n}]$, the forcing functions become

$$\widehat{R}^{(0)} = -\widehat{\Delta C_F}\frac{\mathcal{H}[\widehat{n}]}{\tan\phi} \text{ and } \widehat{R}^{(1)} = -\widehat{\Delta C_F}\frac{\delta[\widehat{n}]}{\sin\phi}. \tag{3.1.13}$$

### 3.1.3 Solutions

Firstly a solution for the inversion layer height $\widehat{h}$ is obtained. Substituting equations (3.1.13) and (3.1.7) into equation (3.1.6) gives an equation for $\widehat{h}$ that be solved in the form $\widehat{h} = \widehat{h}^{(0)} + \mathcal{F}_A\widehat{h}^{(1)}$ where

$$\widehat{h}^{(0)} = \Delta\widehat{C_F}\frac{J^{(0)}[\widehat{n}]}{\tan\phi} \text{ and } \widehat{h}^{(1)} = \Delta\widehat{C_F}\frac{J^{(1)}[\widehat{n}]}{\sin\phi}, \text{ with} \tag{3.1.14a}$$

$$\begin{aligned}J^{(0)}[\widehat{n}] =& \frac{1}{2}\{e^{\widehat{n}}\mathcal{H}[-\widehat{n}] + (2-e^{-\widehat{n}})\mathcal{H}[\widehat{n}]\} \text{ and}\\ J^{(1)}[\widehat{n}] =& \frac{1}{2}e^{-|\widehat{n}|}.\end{aligned} \tag{3.1.14b}$$

For the northern hemisphere, solutions give an increasing on-ice mixed layer thickness over the scale of $\mathcal{L}_{RA}$ for $0 < \phi < \pi/2$, and decreasing mixed layer thickness for $\pi/2 < \phi < \pi$. This is reversed for the southern hemisphere. The leading order term $(\widehat{h}^{(0)})$ gives a monotonic solution across the roughness change. The 1st order solution adds a localised peak centred over the roughness change (see figure 3.3(a)).

Equations (3.1.8) can now be used to give solutions for $\widehat{u} = \widehat{u}^{(0)} + \mathcal{F}_A\widehat{u}^{(1)}$ and $\widehat{v} = \widehat{v}^{(0)} + \mathcal{F}_A\widehat{v}^{(1)}$. To leading order in $\mathcal{F}_A$, equations (3.1.8) can be simplified. This is due to the low Froude number conditions

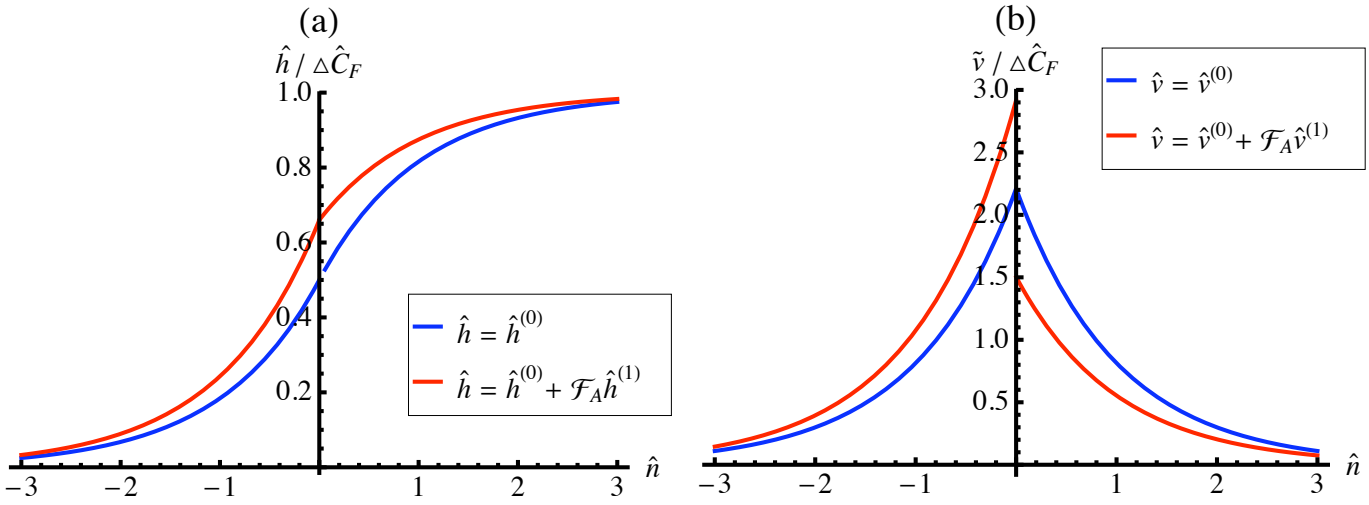


Figure 3.3: Shape of a jet formed by roughness change for angle $\phi = \pi/4$ and Froude number $\mathcal{F}_A = 0.3$ in the northern hemisphere at a latitude of 70° N. The blue solutions are for the leading order, the red solutions are for the first order correction. Plot (a) is for the mixed layer thickness perturbation, plot (b) is for the velocity perturbation parallel to the ice edge. These figures are independent of the magnitude of roughness change $\Delta\widehat{C_F}$ (derived in section 3.1.4) plotting $\widehat{h}/\widehat{\Delta C_F}$ and $\widetilde{v}/\widehat{\Delta C_F}$.

$\mathcal{F}_A < 1$ assumed in the formation of the model. The equations reduce to

$$\widehat{u} = -\frac{\widehat{h}_Y}{\mathcal{F}_A} \text{ and } \widehat{v} = \frac{\widehat{h}_X}{\mathcal{F}_A},$$

which give $\widehat{u}$ and $\widehat{v}$ as

$$\begin{aligned} \widehat{u} &= \frac{\widehat{\Delta C_F}}{\mathcal{F}_A}\cos\phi\left(J^{(0)'}[\widehat{n}] + \mathcal{F}_A\frac{J^{(1)'}[\widehat{n}]}{\cos\phi}\right) \text{ and} \\ \widehat{v} &= \frac{\widehat{\Delta C_F}}{\mathcal{F}_A}\frac{\cos^2\phi}{\sin\phi}\left(J^{(0)'}[\widehat{n}] + \mathcal{F}_A\frac{J^{(1)'}[\widehat{n}]}{\cos\phi}\right), \end{aligned} \tag{3.1.15}$$

where $J^{(0)'}[\widehat{n}] = \partial/\partial\widehat{n}(J^{(0)}) = (1/2)e^{-|\widehat{n}|}$ and $J^{(1)'}[\widehat{n}] = \partial/\partial\widehat{n}(J^{(1)}) = -(1/2)e^{-|\widehat{n}|}\text{sgn}(\widehat{n})$. These perturbation terms are aligned with the wind ($(x, y)$ coordinates). The perturbation parallel to the change in roughness is $\widetilde{v} = \widehat{v}\sin\phi + \widehat{u}\cos\phi$ and can be seen in figure 3.3(b) with approach angle $\phi = \pi/4$ and Froude number $\mathcal{F}_A = 0.3$ at a latitude of 70° N. The leading order terms $(\widehat{u}^{(0)}, \widehat{v}^{(0)})$ give a symmetrical solution about the change in roughness which decays over a distance of order $\mathcal{L}_{RA}$. The first order terms give an antisymmetrical correction, again centred about the roughness change. The correction is greater for a higher Froude number. For the northern hemisphere, the first order terms give an enhanced jet on the smoother side

of the roughness change for $0 < \phi < 90°$, and on the rougher side for $90° < \phi < 180°$, see figure 3.3(b). This is reversed for the southern hemisphere. The strength of the jet is dependent upon the parameter $\widehat{\Delta C_F}$ which in turn depends upon the magnitude of change in roughness (equation (3.1.10)) which is derived in section 3.1.4.

The perturbation perpendicular to the change in roughness (parallel to $\widehat{n}$), $\widetilde{u} = -\widehat{u}\sin\phi + \widehat{v}\cos\phi$, is always zero as $\widehat{u}\cos\phi \equiv \widehat{v}\sin\phi = \widehat{\Delta C_F}/\mathcal{F}_A \cos^2\phi(\cdots)$ for $0 < \phi < 180°$ (see equation (3.1.15)). As the perturbation to the flow is purely parallel to the ice edge, the jet bends the wind to flow on a bearing closer to parallel to the ice edge. The effective angle between the perturbed wind and the ice edge $\phi'$ will be closer to parallel than the original angle $\phi$. This can be seen in figure 3.4(b).

### 3.1.4 Application to the Sea Ice Edge

In order to apply the jets to the atmosphere over the MIZ, numerical values need to be found for the controlling equations, namely (3.1.10), (3.1.15), and the Froude number and Rossby radius. The Froude number and Rossby radius are dependent upon the thickness of the ABL and the strength of the inversion at the top of it. There are observations of atmospheric processes over sea ice from which these values can be taken.

The ABL height over the MIZ is widely documented. The inversion height is low, varying from 200 m (Vihma et al. 2003, Brümmer et al. 1994) to 500 m (Guest et al. 1995, Andreas et al. 1984). Considering the modification to the inversion height in section 3.1.3 and observations of the ABL height over the ocean near the sea ice edge (500 m, Fairall & Markson 1987), a value of $h_A = 400$ m is used in these calculations.

The inversion strength at the top of the ABL is less widely documented. This is due to the difficulty in observing such a change. The most common observations are in the form of a step change in potential temperature. This change ranges from 5°C (Guest et al. 1995, Kantha & Mellor 1989) to 10°C (Tjernström 2005, Andreas et al. 1984). The change in potential temperature can be equated to the inversion layer strength (dimensionless quantities) defined by $\widehat{\Delta\rho_A} = \Delta T/T_A$ (Garratt 1994) where $\Delta T$ is the change in potential temperature and $T_A$ is the atmospheric potential temperature in degrees Kelvin. The range of observed values give $0.18 < \widehat{\Delta\rho_A} < 0.35$ (dimensionless). A typical value of 0.3 is used here.

The selected values of $\widehat{\Delta\rho_A}$ and $h_A$ give the internal wave speed (speed of perturbations along the inversion layer) as $\sqrt{\Delta g_A h_A} \approx 10.9$ m s$^{-1}$. From section 3.1.1 this leads to a Rossby radius of $\mathcal{L}_R \approx 75$

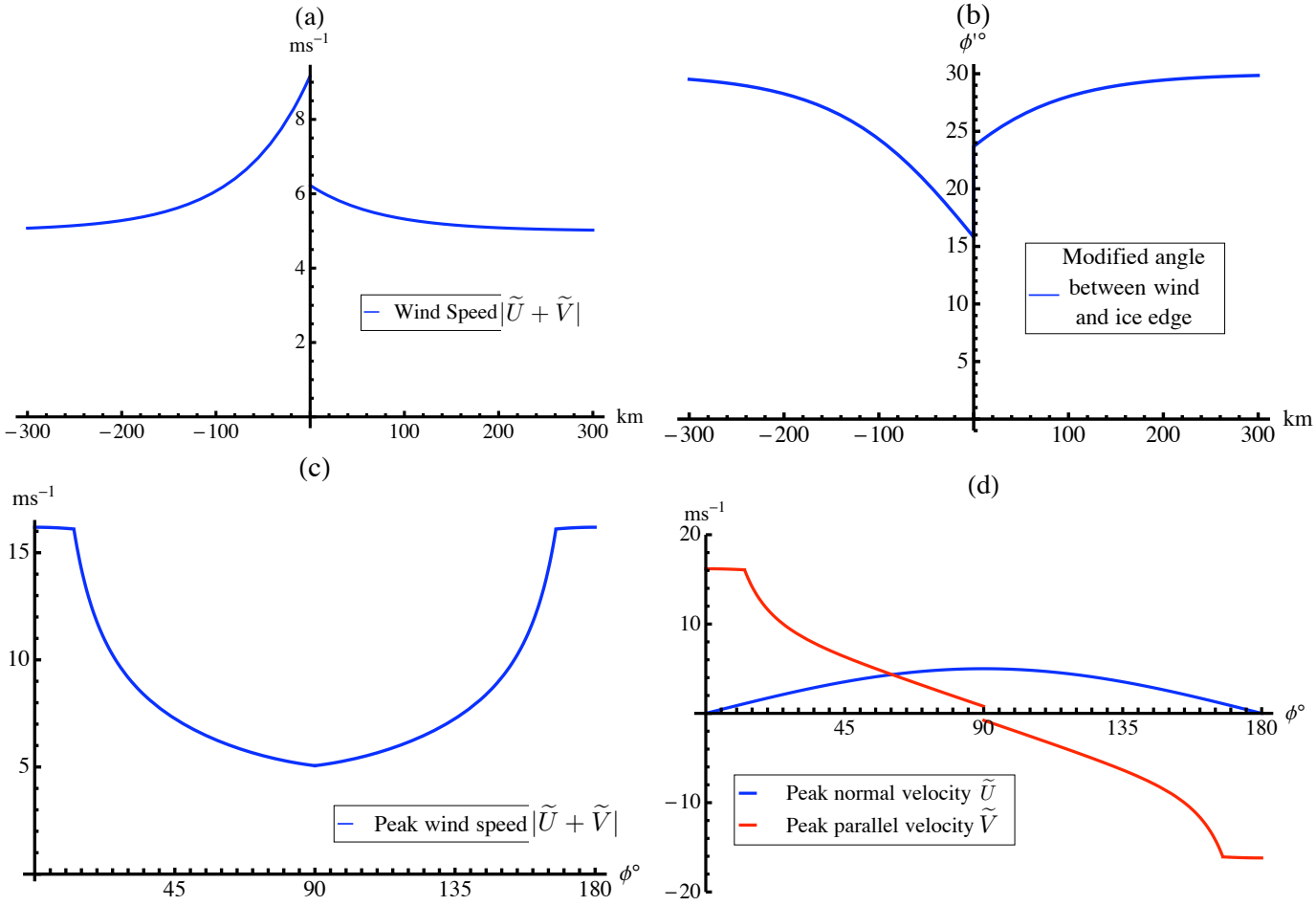


Figure 3.4: Atmospheric jet for $U_A = 5$ m s$^{-1}$ in the northern hemisphere. Plots (a) and (b) are for winds at an angle $\phi = 30°$ to the ice edge. Plot (a) is the modified wind speed, (b) is $\phi'$, the modified angle between the wind and the ice edge (see figure 3.2). The horizontal axes are the normal distance from the ice edge (at 0 km) with positive distance into the ice pack. Plots (c) and (d) are the maximum wind velocity for varying $\phi$. Plot (c) is the wind speed $\underline{\mathbf{u}}_{\widehat{n}}[x = 0]$, (d) is the velocity component normal (blue, $u_{\widehat{n}}[x = 0]$) and parallel (red, $v_{\widehat{n}}[x = 0]$) to the ice edge.

km. The condition for low Froude number flows ($\mathcal{F}_A < 1$) is that $U_A < 10.9$ m s$^{-1}$.

The surface roughness of sea ice is a controlling parameter in atmospheric models with a standard value of $z_0 = 0.001$ m (Vihma et al. 2003). The concept of "roughness length" is an abstract one that has little relationship to any physical measurement (Csanady 2001). Roughness length values are often a product of sensitivity studies in numerical models. The value associated with the sea ice pack is too low for the broken MIZ as shown by Birnbaum & Lupkes (2002) and discussed below. Tisler et al. (2008) investigates

this parameter and uses a value of $z_0 = 0.01$ m for rougher ice. The thickness of the shear layer $h_s$ is an observed and modelled value for the MIZ. It is consistent over several studies at approximately 20 m (Tisler et al. 2008, Kantha & Mellor 1989). These values give $\Delta C_F \approx 3 \times 10^{-3}$ (equation (3.1.10)). This value is comparable to drag coefficients that have been measured over the MIZ. Anderson (1987) measured $C_{10} \approx 3.5 \times 10^{-3}$ (10 m drag coefficient) using direct eddy flux measurements. This is in agreement with Bennett Jr & Hunkins (1986) who analysed the expedition of Andreas et al. (1984). It is also in agreement with the summary of Guest et al. (1995) and the drag modelling of Birnbaum & Lupkes (2002). The study of Birnbaum & Lupkes analyses various drag laws including form drag (the drag from floes edges). They introduce a parameterisation of atmospheric drag over sea ice with a dependance upon the sea ice concentration (see section 2.3.2 for a detailed description). The value of $\Delta C_F \approx 3 \times 10^{-3}$ fits well with the maximum 10 m drag given at 80 % ice concentration.

The perturbation to the flow can now be calculated in dimensional units. The dimensional values for the velocity components perpendicular, $\widetilde{U}$, and parallel, $\widetilde{V}$, to the ice edge are

$$\widetilde{U} = U_A \sin\phi \text{ and} \tag{3.1.16a}$$

$$\widetilde{V} = U_A \cos\phi + U_A \frac{\Delta C_F \mathcal{L}_{RA}}{h_A \tan\phi} \left( J^{(0)'}[\widehat{n}] + \mathcal{F}_A \frac{J^{(1)'}[\widehat{n}]}{\cos\phi} \right). \tag{3.1.16b}$$

The modified wind speed can be seen in figure 3.4(a) and (b) for an approach wind of $U_A = 5$ m s$^{-1}$ at an angle of $\phi = 30°$ to the sea ice edge. The jet formed is approximately 200 km wide, with smaller perturbations covering 600 km. The jet is more intense for the ocean side of the roughness change. This is reversed for $90° < \phi < 180°$ due to the antisymmetrical first order correction in equation (3.1.15), which depends upon which hemisphere the ice edge is in (see section 3.1.3). The wind speed increases about the ice edge (figure 3.4(a)), causing a change in wind direction (figure 3.4(b)). The change in wind direction turns the wind to a bearing closer to parallel to the ice edge for all values of $\phi$ and in both hemispheres. For faster wind speeds, the Froude number increases, creating a larger antisymmetry in the jet, and faster peak wind speeds due to the $\mathcal{F}_A$ dependance upon the $J^{(1)'}[\widehat{n}]$ function in equation (3.1.16b). The solutions presented give a constant wind velocity over the height of the ABL. This constant is comparable to observed 10 m wind velocities.

The parallel component increases rapidly as the upstream flow has a bearing that approaches parallel to the ice edge ($\phi \to 0^\circ$ or $\phi \to 180^\circ$) see figures 3.4(c) and 3.4(d). This increase is due to the inverse $\tan\phi$ relationship in equation (3.1.16b). This increase is not realistic as a flow parallel to the ice edge requires a different mathematical analysis than that which was used in sections 3.1.2 and 3.1.3. Parallel flows are continually accelerated as they flow along the edge. The maximum perturbation to the flow depends on the length of the ice edge. For parallel flows, HORC (*Elongated strips of rough elevated terrain aligned parallel to the wind*, equation (17b)) give the relationship between the maximum dimensional parallel perturbation and edge length as

$$\bar{v} = U_A \frac{\Delta C_F d}{2h_A} \tag{3.1.17}$$

where $d$ is the dimensional length of the ice edge. A length of $d = 250$ km is used in these calculations to represent the persistence of winds that can form parallel to the ice edge. This is in accordance with the winds and ice edge state observed during on-ice winds (Massom et al. 2006, Massom et al. 2008, King et al. 2010). Another limiting factor is the straightness of the ice edge. The edge of the ice pack is unlikely to form a straight edge and is more likely to meander and appear rough. A purely parallel flow is unlikely to persist for longer than a Rossby Radius. An angle limit of $5^\circ$ will be used in these calculations, limiting the size of the perturbation for angles of $0^\circ \leq \phi \leq 5^\circ$ and $175^\circ \leq \phi \leq 180^\circ$. The maximum perturbation and angle limit cause the cut off seen in figures 3.4(c) and (d).

## 3.2 Oceanic Jets

The atmospheric jet theory of HORC can also be applied to ocean currents underneath the MIZ as the ocean mixed layer also presents a stratified flow. The theory does however need to be refined. The controlling processes are similar and are analogous to the processes in the atmosphere. The interaction between the surface shear layer and inversion layer heights that leads to atmospheric jet formation for subcritical winds speeds (see figure 3.1) is assumed to occur within the ocean mixed layer for subcritical current speeds. This assumption leads to a model of ocean jet formation.

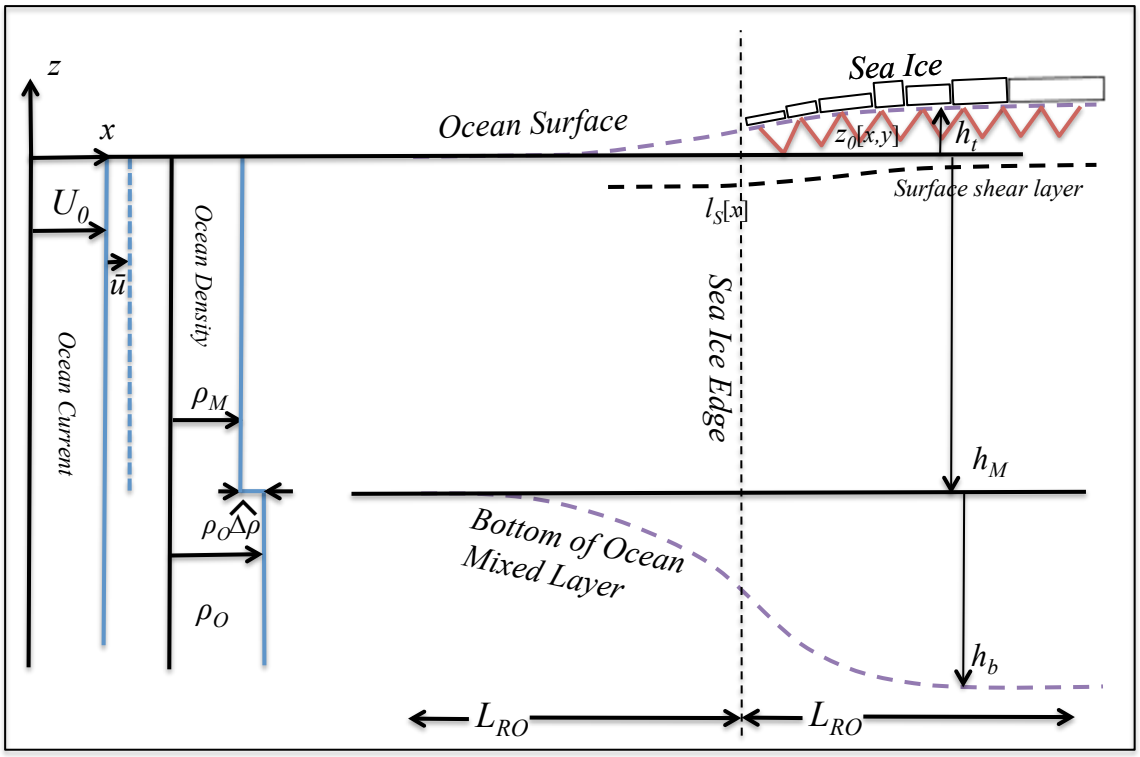


Figure 3.5: Vertical profile of velocity ($U[x]$, $\mathbf{u}$) and density ($\rho_0$) of a shallow layer perturbed flow.

### 3.2.1 Mixed-Layer Model Equations

The ocean mixed layer of density $\rho_M$ and thickness $h_M$ sits above the ocean of higher density $\rho_O$ as illustrated in figure 3.5. The normalised step change in density is $\widehat{\Delta\rho_O} = (\rho_O - \rho_M)/\rho_O$. A uniform current of strength $U_O$ encounters the ice with roughness length $z_0$. This causes perturbations to the velocity $(\bar{u}, \bar{v})$, pressure $p$, mixed layer depth $h_b$, and sea surface height $h_t$. This simple formulation of the mixed layer is similar to that used by Roed & O'Brien (1983).

As with HORC and the equations in section 3.1.1, modifications to the ocean current within the mixed layer are modelled using a linearised momentum balance for the perturbations to the flow field, equation (3.1.1). As in section 3.1.1 expressions for pressure $(P + p)$, layer thickness perturbation $(h = h_t + h_b)$, and body forces $(F, G)$ are obtained. The scaling values for the flow are the oceanic Froude number $\mathcal{F}_O = U_O/\sqrt{\Delta g_O h_M}$, and the oceanic Rossby radius $\mathcal{L}_{RO} = \sqrt{\Delta g_O h_M}/f_c$ where $\Delta g_O = g\widehat{\Delta\rho_O}$.

The perturbation velocity, $w$, at the top and bottom of the mixed layer is equated to the change in layer thickness with

$$\begin{aligned} Dh_t = &\quad w[z = h_t] \text{ and} \\ Dh_b = &- w[z = -(h_M + h_b)]. \end{aligned}$$

The overall change in layer thickness is the sum of these ($Dh = Dh_t + Dh_b$), which can be approximated by the velocity perturbation by integrating the continuity equation over the mixed layer giving

$$Dh = w[z = ht] - w[z = -(h_M + h_b)] = \int_{-(h_M+h_b)}^{h_t} w_z dz \approx -(\bar{u}_x + \bar{v}_y)h_M. \tag{3.2.1}$$

The total pressure in the upper layer at position $(x, z)$ is

$$\begin{aligned} (P + p)[x, z] &= (P + p)[x, h_t] + g(1 - \widehat{\Delta\rho_O})(h_t - z) \text{ and} \\ (P + p)[x \to -\infty, z] &= (P + p)[x \to -\infty, 0] - g(1 - \widehat{\Delta\rho_O})z, \end{aligned}$$

at $x \to -\infty$ far from the sea ice edge. The sea surface pressure is taken to be independent of position with

$$(P + p)[x, h_t] = (P + p)[x \to -\infty, 0] = P_s.$$

Furthermore, pressure at equal depths is assumed to be equal throughout the model with

$$\begin{aligned} (P + p)[x \to -\infty, z = -(h_M + h_b)] &= (P + p)[x, z = -(h_M + h_b)] \\ P_s + g(1 - \widehat{\Delta\rho_O})h_M + gh_b &= P_s + g(1 - \widehat{\Delta\rho_O})(h_t + h_M + h_b), \text{ which gives} \\ \widehat{\Delta\rho_O}h_b &= (1 - \widehat{\Delta\rho_O})h_t. \end{aligned} \tag{3.2.2}$$

Thus the thickness of the mixed layer is linked to the raised sea surface with $h = h_t/\widehat{\Delta\rho_O}$. As the density inversion is of order $10^{-3}$ and the mixed layer is of order 10 m thick, the change in sea surface level $h_t$ will be of order $10^{-2}$ m. This change happens over a Rossby radius ($10^4$ m) and will be almost undetectable.

See section 3.2.4 for derivation of numerical values.

The pressure perturbation can now be given by

$$(P+p)[x,z] - (P+p)[x \to -\infty, z] =$$
$$p[z] = g(1 - \widehat{\Delta\rho_O})h_t \approx \Delta g_O h$$

to leading order. The horizontal pressure gradients are

$$\begin{aligned} p_x =& \Delta g_O h_x \text{ and} \\ p_y =& \Delta g_O h_y. \end{aligned} \tag{3.2.3}$$

Combining the pressure perturbations and body forces in equations (3.1.1) and (3.2.3) and averaging over the mixed layer $(-(h_M + h_b) < z < h_t)$ we get

$$\begin{aligned} D\bar{u} =& -\Delta g_O h_x + f_c \bar{v} + \overline{F} \text{ and} \\ D\bar{v} =& -\Delta g_O h_y - f_c \bar{u} + \overline{G}, \end{aligned} \tag{3.2.4}$$

where $(\overline{F}, \overline{G})$ are the body forces averaged over the mixed layer. This is analogous to equation (3.1.4).

Equations (3.2.1) and (3.2.4) can be combined to give an equation to be solved for $h$ with

$$D\left[\nabla^2 h - \frac{h}{\mathcal{L}_{RO}^2} - \frac{\mathcal{F}_O^2}{U_O^2} D^2 h\right] = \mathcal{F}_O \frac{h_M}{U_O}\left[\frac{1}{\mathcal{L}_{RO}}(\overline{G}_x - \overline{F}_y) + \frac{\mathcal{F}_O}{U_A} D(\overline{F}_x + \overline{G}_y)\right]. \tag{3.2.5}$$

As with equation (3.1.5) the steady state, $(\partial/\partial t = 0)$, gives equations (3.1.6) and (3.1.7) with the oceanic Froude number $\mathcal{F}_O$, rather than atmospheric Froude number $\mathcal{F}_A$. The scaling is this time horizontally over the oceanic Rossby radius $(\mathcal{L}_{RO})$ and vertically over the mixed layer $(h_M)$ with $\widehat{h} = h/h_M$, $(X, Y) = (x, y)/\mathcal{L}_{RO}$ and $\partial/\partial X = \mathcal{L}_{RO}\partial/\partial x$. The forcing functions are similarly scaled with $(\widehat{F}, \widehat{G}) = (\mathcal{L}_{RO}\mathcal{F}_O/U_O)(\overline{F}, \overline{G})$ as in equation (3.1.7).

### 3.2.2 Forcing

The body forces $(F, G)$ and the averaged and scaled functions $(\widehat{F}, \widehat{G})$ are dependent upon the stress applied to the ocean currents by the underside of the broken sea ice. The corollary to this drag, the drag experienced by sea ice in the ocean, is

$$\tilde{\boldsymbol{\tau}}^o = \rho_o C_o |\mathbf{U}_g^o - \mathbf{u}| \left[ (\mathbf{U}_g^o - \mathbf{u}) \cos\theta + \mathbf{k} \times (\mathbf{U}_g^o - \mathbf{u}) \sin\theta \right] \tag{3.2.6}$$

(e.g. Feltham 2005), where $\mathbf{U}_g^o$ is the ocean velocity, $\mathbf{u}$ is the ice velocity, $\theta$ is a turning angle, $\rho_o$ is the density of sea water and $C_o$ is a constant associated with the drag between the ocean and ice. The turning angle is associated with the Ekman turning of the water column underneath the ice. As this water column is considered in this model, $\theta$ can be set to zero. The ice velocity is of the same order as the ocean velocity (Johannessen et al. (1983) for example and the results in chapters 5 and 6) so forcing terms similar to equations (3.1.9) cannot be used for the ocean. The flow velocity term in these equations needs to be replaced with relative difference in velocity between the ocean and ice. This is done by introducing $u_{\text{diff}}^2 = |\widehat{\mathbf{U}}_O - \widehat{\mathbf{U}}_I|^2$ where $\widehat{\mathbf{U}}_{O,I}$ are the non-dimensional velocities of the ocean and sea ice at the sea ice edge, giving the body forces as

$$\begin{aligned} \overline{F} =& \overline{F}_D = -\frac{\Delta C_F U_O^2 u_{\text{diff}}^2}{h_M} \text{ and} \\ \overline{G} =& \overline{G}_D = -\frac{\Delta C_G U_O^2 u_{\text{diff}}^2}{h_M}, \end{aligned} \tag{3.2.7}$$

selecting appropriate values for $\Delta C_F$ and $\Delta C_G$.

Substituting equation (3.2.7) into equation (3.1.7) the forcing functions become

$$\widehat{R}^{(0)} = -\widehat{\Delta C_F} u_{\text{diff}}^2 \frac{\mathcal{H}[\widehat{n}]}{\tan\phi} \text{ and } \widehat{R}^{(1)} = -\widehat{\Delta C_F} u_{\text{diff}}^2 \frac{\delta[\widehat{n}]}{\sin\phi}, \tag{3.2.8}$$

where $\widehat{\Delta C_F} = \Delta C_F \mathcal{L}_{RO} \mathcal{F}_O / h_M$ and $\widehat{n} = (x \sin\phi - y \cos\phi)/\mathcal{L}_{RO}$.

### 3.2.3 Solutions

As with the atmospheric jet in section 3.1.3, equations (3.2.8) give a series solution to equation (3.1.6) (replacing $\mathcal{F}_A$ with $\mathcal{F}_O$) with $\widehat{h} = \widehat{h}^{(0)} + \mathcal{F}_O \widehat{h}^{(1)}$ where

$$\begin{aligned} \widehat{h}^{(0)} &= \widehat{\Delta C_F} u_{\text{diff}}^2 \frac{J^{(0)}[\widehat{n}]}{\tan\phi} \text{ and} \\ \widehat{h}^{(1)} &= \widehat{\Delta C_F} u_{\text{diff}}^2 \frac{J^{(1)}[\widehat{n}]}{\sin\phi}, \end{aligned}$$

where $J^{(0)}$ and $J^{(1)}$ are given by (3.1.14b).

For the northern hemisphere these solutions give an increasing mixed layer thickness in the on-ice direction over the scale of $\mathcal{L}_{RO}$ for $0° < \phi < 90°$, and decreasing for $90° < \phi < 180°$. The opposite is true for the southern hemisphere. The leading order term $\widehat{h}^{(0)}$ gives a monotonic solution across the roughness change. The first order solution supplies a localised peak centred over the roughness change. This can be seen in figure 3.3(a), with an increase in mixed layer thickness (shown), causing a deepening of the density step change (at $z = -(h_M + h_b)$).

The solutions for $\widehat{u} = \widehat{u}^{(0)} + \mathcal{F}_O \hat{u}^{(1)}$ and $\widehat{v} = \widehat{v}^{(0)} + \mathcal{F}_O \widehat{v}^{(1)}$ also take a similar form to the atmospheric perturbations (equations (3.1.15)) with

$$\begin{aligned} \widehat{u} &= \frac{\widehat{\Delta C_F} u_{\text{diff}}^2}{\mathcal{F}_O} \cos\phi \left( J^{(0)'}[\widehat{n}] + \mathcal{F}_O \frac{J^{(1)'}[\widehat{n}]}{\cos\phi} \right) \text{ and} \\ \widehat{v} &= \frac{\widehat{\Delta C_F} u_{\text{diff}}^2}{\mathcal{F}_O} \frac{\cos^2\phi}{\sin\phi} \left( J^{(0)'}[\widehat{n}] + \mathcal{F}_O \frac{J^{(1)'}[\widehat{n}]}{\cos\phi} \right), \end{aligned} \tag{3.2.9}$$

where $J^{(0)'}[\hat{n}] = \partial/\partial\hat{n}(J^{(0)}) = (1/2)e^{-|\hat{n}|}$ and $J^{(1)'}[\hat{n}] = \partial/\partial\hat{n}(J^{(1)}) = -(1/2)e^{-|\hat{n}|}\text{sgn}(\hat{n})$. These perturbation terms are aligned with the ocean current ($(x, y)$ coordinates). The perturbation parallel to the change in roughness is analogous to the atmospheric jet with $\tilde{v} = \hat{v}\sin\phi + \hat{u}\cos\phi$, and can be seen in figure 3.3(b). The solutions are of the same form, decaying over the oceanic Rossby radius $\mathcal{L}_{RO}$ with an added first order peak dependent upon the Froude number $\mathcal{F}_O$. Again the strength of the jet depends upon $\widehat{\Delta C_F}$ and the change in surface roughness. The perpendicular perturbation is of the same form, $\widetilde{u} = -\widehat{u}\sin\phi + \widehat{v}\cos\phi$, and is identically zero.

### 3.2.4 Application to the Sea Ice Edge

The strength and size of the ocean jets are dependent upon a number of numerical values associated with the flow. The characteristic scales associated with the flow $(\mathcal{L}_{RO}, \mathcal{F}_O)$ are calculated from the density inversion and mixed layer thickness. These two values can be taken from observations of ocean temperature and salinity. The equation of state for seawater is

$$\rho = \rho_0(1 - \alpha T + \beta S) \tag{3.2.10}$$

(from Thorpe 2005), where $\rho_0$ is a reference ocean density, $T$ is the change in temperature and $S$ is the change in salinity. $\alpha$ and $\beta$ are constants based on the expansion of water and are specified at reference values for $S$ and $T$ and vary with depth. For the mixed layer at the sea ice edge we use equation (3.2.10) to calculate $\widehat{\Delta\rho_O}$ from salinity and temperature changes giving $\widehat{\Delta\rho_O} = -\alpha\Delta T + \beta\Delta S$. $\alpha$ and $\beta$ are taken as $52 \times 10^{-6}$ °K$^{-1}$ and $0.82$ psu$^{-1}$ respectively for seawater near it's freezing temperature of $-1.8$°C. For the OML in polar regions the change in salinity contributes most to the change in ocean density. Sea ice growth causes a release of salt into the OML and sea ice melt a release of freshwater. This gives a relatively large value of $\beta\Delta S$ compared to $\alpha\Delta T$ as the ocean temperature remains close to freezing throughout the year.

Measurements of mixed layer depth vary by some degree. For the sea ice pack far from the open ocean, the mixed layer is typically 20-30 m deep, and rarely exceeds 50 m (Toole et al. 2010, McPhee et al. 2005). For the MIZ it is more variable. Values can vary from 25 m (Fer & Sundfjord 2007, Williams et al. 2008, Quadfasel et al. 1987) to as high as 150 m (Markus 1999, Padman & Dillon 1991).

This variability in the mixed layer depth makes selection of a value for $h_M$ challenging. There is often a seasonal variation in the depth (Markus 1999), which could be included in longer time series coupled models. There is a fairly good correlation between the depth of the mixed layer and the change in salinity. For a shallow mixed layer the salinity change was between 1.5 and 3 psu (Quadfasel et al. 1987, Toole et al. 2010, McPhee et al. 2005). Whereas for a deeper mixed layer it was lower at 1psu (Padman & Dillon 1991). The change in temperature across the layer was between $0.5 - 1$°C for all studies.

Average values of $h_M = 40$ m, $T = 0.5$°C and $S = 2.5$ psu are taken. This gives a density change of $\rho_O\widehat{\Delta\rho_O} \approx 2$ kg m$^{-3}$ which correlates well with values given by McPhee et al. (1987) and Toole et al.

(2010). These values give an internal wave speed of $\sqrt{\Delta g h_M} \approx 0.9$ m s$^{-1}$ which results in a Rossby radius of $\approx 6$ km. The value of $\sqrt{\Delta g h_M}$ is high enough for low Froude number conditions for $U_0 < 0.9$ m s$^{-1}$. This is true for all but the most extreme ocean currents (Fer & Sundfjord 2007).

The effect the roughness change has upon the flow depends upon the values of $z_0$, the roughness length, and $l_S$, the surface shear layer. There has been little study into the surface roughness of the underside of the MIZ. Shaw et al. (2008) conducted a study of roughness length measurements under the central Arctic pack ice: the typical roughness lengths were of 5 mm$< z_0 <$30 mm. A value of $z_0 = 20$ mm and a shear layer depth of $l_S = 4.5$ m gives a value of $\Delta C_F \approx 0.0055$ (equation (3.1.10)). This is equal to the value of $C_O$ (see equation (3.2.6) in section 3.2.2) used by Feltham (2005). Shaw et al. (2008) also recorded roughness lengths of up to $z_0 = 150$ mm for a rougher sea ice due to the presence of pressure ridges. As the the broken floes of the MIZ suggest a rougher surface than that of the sea ice pack, a value of $z_0 = 100$ mm shall be used giving $\Delta C_F \approx 0.011$.

The dimensional perturbations can now be calculated. They are of a similar form to the atmospheric perturbation in equation (3.1.16) with

$$(U+u)_{\widehat{n}} = U_O \sin\phi \text{ and} \tag{3.2.11a}$$

$$(V+v)_{\widehat{n}} = U_O \cos\phi + U_O \frac{\Delta C_F \mathcal{L}_{RO} u_{\text{diff}}^2}{h_M \tan\phi} \left( J^{(0)'}[\widehat{n}] + \mathcal{F}_O \frac{J^{(1)'}[\widehat{n}]}{\cos\phi} \right), \tag{3.2.11b}$$

with one major difference in the addition of the $u_{\text{diff}}^2$ term. Knowledge of the sign and size of $u_{\text{diff}}^2$ is essential to modelling the ocean jets. If the sea ice and ocean are moving wight he same velocity, the ocean will experience no relative velocity to the change in surface roughness and no jet will form. However if the ice is still there will be a large relative velocity and a strong jet will form. A simplified relationship between the ocean and ice is used here, so to give a demonstration of the size and shape of the oceanic jet. Figure 3.6 contains demonstration calculations for an approach ocean current speed of $U_O = 0.2$ m s$^{-1}$ at an angle of $\phi = 30^\circ$ to the sea ice edge and shows the changing jet strength for varying $\phi$.

The sea ice edge is assumed to be compacted. The ice can move freely parallel to the edge, but not normal to the edge. For the purpose of illustration the parallel ice velocity is taken to be $3/4$ of the parallel component of the far field ocean speed, and $u_{\text{diff}}^2$ is calculated from the ice velocity ($\widehat{U}_{I(1,2)}$ components of

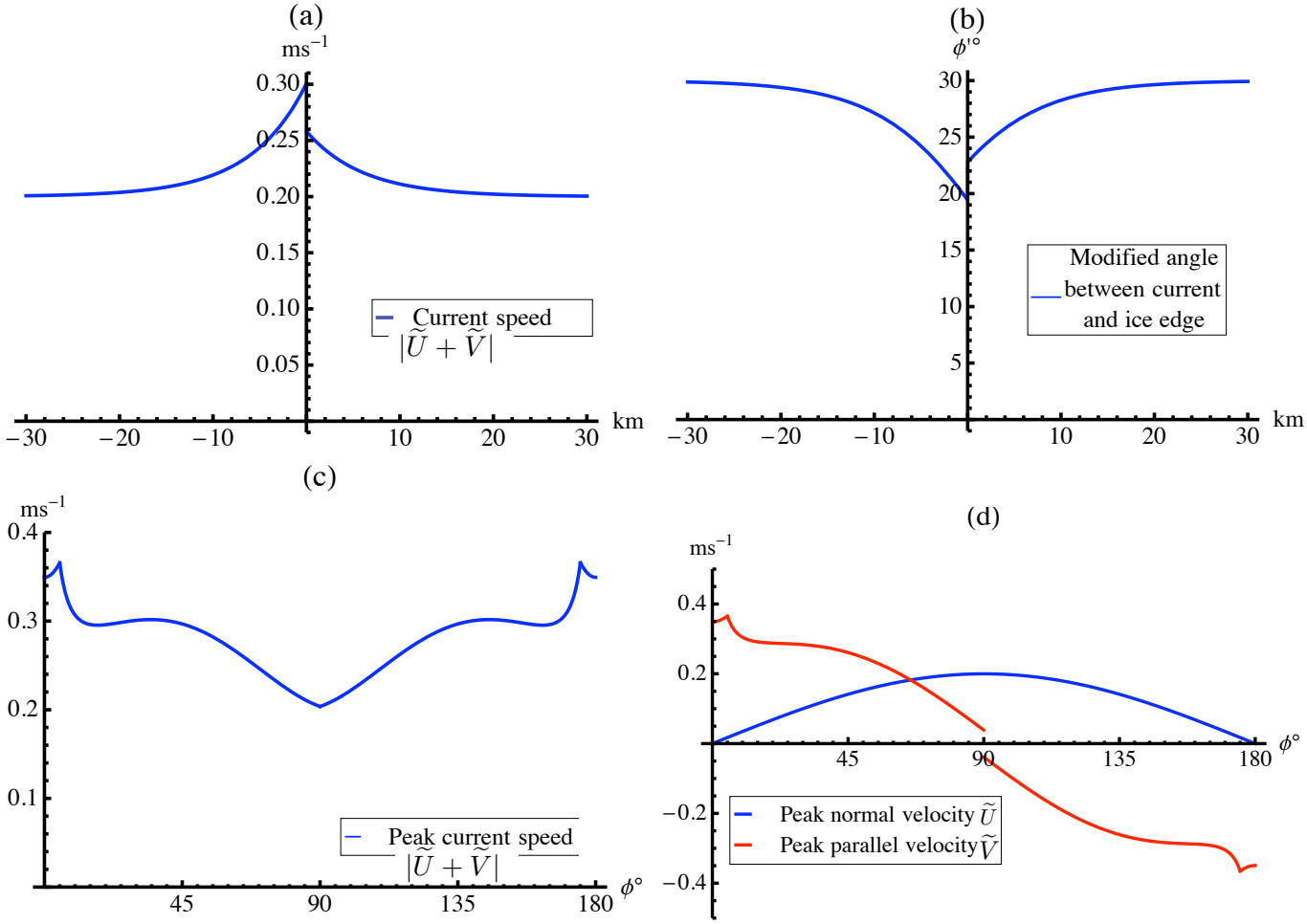


Figure 3.6: As figure 3.4 but for the ocean in the northern hemisphere. The approach ocean current speed is $U_O = 0.2$ m s$^{-1}$ for all figures and at an angle of $\phi = 30°$ to the sea ice edge in (a) and (b).

$\widehat{\mathbf{U}}_I$) and far field ocean velocity ($\widehat{U}_{O(1,2)}$ components of $\widehat{\mathbf{U}}_O$) with

$$u^2_{\text{diff}} = (\widehat{U}_{O1} - \widehat{U}_{I1})^2 + (\widehat{U}_{O2} - \widehat{U}_{I2})^2 = \sin^2\phi + \frac{\cos^2\phi}{16}.$$

This approximation is only valid for a system that only considers an ocean jet. When atmospheric forcing is present, it is possible that the ice is blown to move faster than the ocean, or slowed against the ocean current. This would modify the difference between the ocean and ice velocities, and the strength of the ocean jet.

The ocean jet perturbations can be seen in figure 3.6. This figure is for demonstration only as the jet

formation is best modelled by coupling the ocean jet formation to a dynamic sea ice model as in chapter 5. The ocean jet is similar in shape to the atmospheric jet seen in figure 3.4 though the size is different. The ocean jet perturbations extend over a distance of 40 km with the most significant perturbations within the central 20 km. The jets are also less intense due to the change in surface roughness being calculated from the difference between ocean and ice velocity. The relative increase in parallel velocity for $\phi = 30^\circ$ (figure 3.6(a)) is small compared to the wind velocity which doubles for the same value of $\phi$. Again there is an antisymmetrical correction about the change in roughness. This is of the same form discussed in section 3.1.4 due to the similarity between equations (3.1.15) and (3.2.9).

The relationship between the angle $\phi$ and the jet strength is greatly affected by the $u_{\text{diff}}^2$ term. Sea ice drift in the direction parallel to the sea ice is less restricted by the sea ice pack. This reduces $u_{\text{diff}}^2$ for currents with a bearing parallel to the ice edge which in turn reduces the jet strength. This creates the non monotonic increase in figures 3.6(c) and (d), in particular the local maximum at $\phi = 40^\circ$ and $\phi = 140^\circ$. This in contrast to the purely exponential increase experienced by the atmospheric jet in figures 3.4(c) and (d). The same angle limit as used in section 3.1.4 restricts the strength of the ocean jet. No maximum perturbation limit is used as the $u_{\text{diff}}^2$ reduction keeps the perturbations small.

# CHAPTER 4

# AN ANALYTICAL MODEL OF SEA ICE DRIFT IN A COMPACTED MARGINAL ICE ZONE

The formation of atmospheric and oceanic jets have been modelled at the sea ice edge and in the Marginal Ice Zone (MIZ). This formation is due to a sharp change in surface roughness length and the Coriolis effect and is described in detail in chapter 3. To model the sea ice drift during jet formation an analytical model of sea ice drift has been created. The size and shape of the jets is discussed in section 4.1. The momentum balance used in the model is described in section 4.2. The boundary conditions for the model are taken from free drifting ice which is matched to the model equations in section 4.3.

---

Jet formation as described in chapter 3 modifies the atmosphere and ocean velocities. A change in velocity causes a change in stress applied to the sea ice in the momentum balance described in section 2.2.3. This momentum balance can be solved in steady state to give solutions for ice velocity and concentration. The momentum balance is applied to the ice edge using scaling and simplifications described in section 4.2.1. The ice edge is defined by a low ice concentration. For a low ice concentration a momentum balance is used to model free drifting ice. This is described in section 4.3. The model can be rearranged algebraically into a nonlinear coupled system of differential equations. The solutions are dependant upon the imposed boundary

conditions. These conditions come from the atmospheric and oceanic forcing and the conditions at the extreme ice edge as described in section 4.3.3. All coordinate systems used in this chapter will be redefined (see figure 4.1) and the systems used in chapter 3 are no longer applicable. Notation for this chapter is described below and listed in table 1.

## 4.1 Jet Formation

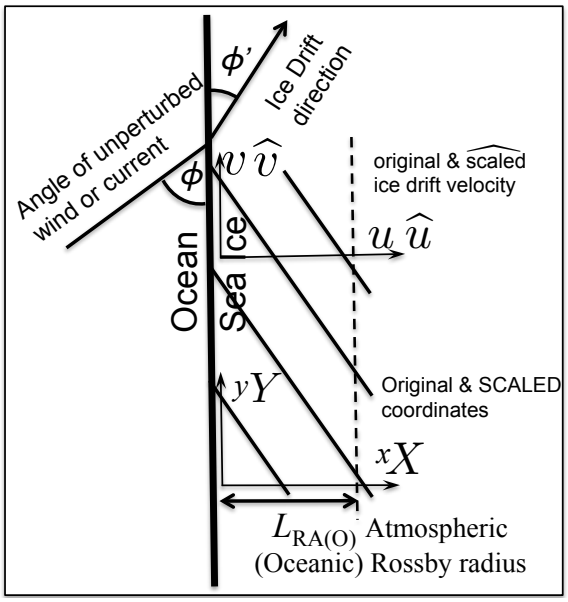


Figure 4.1: Coordinate and ice drift velocity notation for the analytical model. This notation is true for the results in chapters 5 and 6.

The formation of atmospheric and oceanic jets over the sea ice edge is modelled as in chapter 3. The size and shape of the jets depend on a number of variables. These variables are the speed of the approach current, the angle of incidence between the current and the ice edge, the drag between the sea ice and the fluid (ocean or atmosphere), and the sign and magnitude of the Coriolis effect (depending on latitude and the north/south hemisphere). These variables are varied, with each case tested against identical currents with no jet. The gravity wave speed and layer thickness associated with the atmospheric boundary layer above, and ocean mixed layer below, the sea ice are also important because they affect the Rossby radius and Froude number associated with each flow. The gravity wave speeds and layer thickness are held constant throughout the experiments and their derivation can be found in chapter 3.

### 4.1.1 Atmosphere

The formation of the atmospheric jet is described by equation (3.1.16b). The jet is centred about the change in surface roughness length that causes it to form. For the ice edge this corresponds to the extreme edge of the ice pack. In this model the sea ice edge is assumed to be compact with a sharp increase in ice concentration expected. This sharp increase clearly defines point of sharp change in surface roughness length.

The stress applied to the ice from the atmosphere is calculated from the wind stress with

$$\tilde{\boldsymbol{\tau}}^a = \rho_a C_a |\mathbf{U}^a| \mathbf{U}^a, \tag{4.1.1}$$

where $\rho_a$ is the air density, $C_a$ is a drag coefficient and $\mathbf{U}^a$ the wind velocity vector. For these calculations $C_a = \Delta C_F$ (as used in equation (3.1.16b) to define the atmospheric jet) which is higher than typically used for the sea ice pack. This represents the increased roughness of the broken floes at the sea ice edge. The values of $C_a$ and $\mathbf{U}^a$ correspond to $\mathbf{U}^a$ being calculated at a constant height of 10 m. This height is used in many observations such as those in section 3.1.4.

### 4.1.2 Ocean

The ocean jet formation is described similarly to the atmospheric jet in section 4.1.1 by equation (3.2.11b). The $u_{\text{diff}}^2$ term scales the drag term to depend on the difference between the ocean and ice velocities. This dependance upon the ice velocity requires the jet size to be solved along with the ice velocity. The theory behind the jet formation views the sea ice as a slab moving at a constant velocity. As the sea ice does not move as a slab, and has a varying velocity profile, a typical velocity is needed to calculate $u_{\text{diff}}^2$. This is taken from the free drift calculations for the extreme edge of the pack, see sections 4.3 and 4.3.3.

The ocean jets are typically an order of magnitude thinner than the atmospheric jets with a oceanic Rossby radius of 6 km compared to an atmospheric Rossby radius of 75 km (see figures 3.4 and 3.6). They are less intense and are less antisymmetric. The Froude number associated with the ocean is generally less than with the atmosphere, with $\mathcal{F}_{RO} < 1$ for all but the most extreme currents. Again the jet is centred about the extreme edge of the sea ice pack.

The stress applied to ice from the moving ocean is dependent upon the difference in velocity between

the ice and ocean beneath it. A turning angle between the velocities and the stress direction is used to simulate Ekman turning in the ocean boundary layer beneath the ice in accordance with observations (e.g. Csanady 2001). The ocean stress is calculated by equation (3.2.6). The turning angle is set to zero for these calculations, to simplify the experiment and because the ocean jet formation considers the processes that the turning angle replicates. As with the atmospheric drag, $C_o = \Delta C_F$ with $\Delta C_F$ taken as applied to the ocean jet in equation (3.2.11b) to account for the broken ice floes at the sea ice edge.

## 4.2 Ice Pack Dynamics

To model the compacted sea ice pack we use the momentum balance of equation (2.2.4) described in section 2.2.3. The components of this momentum balance given by equation (2.2.4) are used to calculate the sea ice drift from the applied atmospheric and oceanic stresses. The internal ice stresses are calculated using the Viscous-Plastic rheology described in appendix A.

### 4.2.1 Application to the Sea Ice Edge

The atmospheric and oceanic jets form during on-ice winds and currents. These winds and currents cause the ice pack to compress forming a stable ice edge. This stability allows several assumptions about the ice to be made. Primarily it can reach a steady state removing all time derivatives from the model, i.e $\partial/\partial t = 0$. The coordinate system can be aligned with the ice edge, with $x$ normal and $y$ parallel to the edge. Considering an infinite laterally invariant ice edge gives $\partial/\partial y = 0$. These simplifications are similar to those used by Lepparanta & Hibler (1985) in their study of MIZ dynamics. As the edge is compacted assumptions can be made about the normal ice velocity $u$. The thickness of the sea ice is take as a constant with $h = 1$ m. The sea surface tilt is also ignored with $\mathbf{S} = 0$. For an ice concentration of $A < 1$ the thickness distribution of the sea ice does not need to be balanced using equations such as (2.2.1) or (2.2.2).

**Zero Normal Ice Velocity**

The most simple assumption to make about the normal ice velocity is to set it to zero, i.e. $u = 0$. This gives the steady state components of equation (2.2.4) as

$$\begin{aligned} 0 &= \rho_I h f_c v + A(\tau_1^a + \tau_1^o) + \sigma_{11x} \text{ and} \\ 0 &= A(\tau_2^a + \tau_2^o) + \sigma_{12x}, \end{aligned} \tag{4.2.1}$$

where the mass $m = \rho_I h$ has been equated to the density multiplied by the thickness of the sea ice. Subscript 1 and 2 refer to the $x$ and $y$ direction respectively and subscript $x$ refers to the partial $x$ derivative.

The values of $\sigma_{11}$ and $\sigma_{12}$ can be calculated from equation (A.2.2). The only non-zero components of the strain rate tensor are $\dot{\varepsilon}_{12} = \dot{\varepsilon}_{21} = v_x/2$, simplifying equations (A.2.3). The desired components of the stress tensor can be calculated with

$$\sigma_{11} = -\frac{p}{2}, \text{ and} \tag{4.2.2a}$$

$$\begin{aligned} \sigma_{12} = &\quad \frac{p}{2} \frac{e^{-2} v_x}{(2e^{-2} {v_x}^2)^{\frac{1}{2}}} \\ = &\quad \frac{p}{2\sqrt{2}e} \text{sgn}(v_x), \end{aligned} \tag{4.2.2b}$$

where $\text{sgn}(v_x) = -1$ for $v_x > 0$ and $\text{sgn}(v_x) = 1$ for $v_x < 0$ is the sign function. The point of $v_x = 0$ is undefined in this model. The ice pressure $p$ is given as a function of ice concentration as in equation (A.2.4) in appendix A.

The length scale of the model depends on the Rossby radius of the jet formation $\mathcal{L}_R$, given the appropriate value for the jet being investigated $\mathcal{L}_{RA}$ for the atmosphere, $\mathcal{L}_{RO}$ for the ocean. The model is non-dimensionalised over these distances. For experiments with both jets, the atmospheric Rossby radius will be used as it is an order greater than the oceanic Rossby radius. The ice velocity is also non-dimensionalised. Typical ice speeds vary depending on the ocean current. For a still ocean the ice speed will be small, for a moving ocean the ice speed will be greater, of the same order as the ocean speed. The applied stresses are also scaled.

Equation (4.2.1) can be non-dimensionalised in velocity $\mathbf{u} \to U_I \widehat{\mathbf{u}}$, position $(x, y) \to \mathcal{L}_R(X, Y)$, deriva-

tives $\partial/\partial x \to (1/\mathcal{L}_R)(\partial/\partial X)$ and applied stress $\tilde{\boldsymbol{\tau}}^{\boldsymbol{a}} \to \mathcal{T}_a\widehat{\boldsymbol{\tau}}^{\boldsymbol{a}}, \tilde{\boldsymbol{\tau}}^{\boldsymbol{o}} \to \mathcal{T}_o\widehat{\boldsymbol{\tau}}^{\boldsymbol{o}}$ where the $\mathcal{T}$ terms are typical stress values defined later. The scaled components of equation (2.2.4) can be calculated from equation (4.2.1) and (4.2.2) with

$$0 = f_c\mathcal{L}_R U_I\widehat{v} + \frac{\mathcal{L}_R}{\rho_I h}(\mathcal{T}_a\widehat{\tau}_1^a + \mathcal{T}_o\widehat{\tau}_1^o)A - \frac{p^*}{2\rho_I}\frac{\partial g}{\partial A}\frac{\partial A}{\partial X}, \text{and} \tag{4.2.3a}$$

$$0 = \frac{\mathcal{L}_R}{\rho_I h}(\mathcal{T}_a\widehat{\tau}_2^a + \mathcal{T}_o\widehat{\tau}_2^o)A + \frac{p^*}{2\sqrt{2}e\rho_I}\text{sgn}(\widehat{v}_X)\frac{\partial g}{\partial A}\frac{\partial A}{\partial X}. \tag{4.2.3b}$$

These two equations can be combined in order to separate the $A$ and $\widehat{v}$ variables giving

$$g_A A_X = -\text{sgn}(\widehat{v}_X)\frac{2\sqrt{2}e\mathcal{L}_R}{p^* h}(\mathcal{T}_a\widehat{\tau}_2^a + \mathcal{T}_o\widehat{\tau}_2^o)A \text{ and} \tag{4.2.4a}$$

$$\widehat{v} = -\frac{1}{f_c U_I \rho_I h}\left[(\mathcal{T}_a\widehat{\tau}_1^a + \mathcal{T}_o\widehat{\tau}_1^o) + \text{sgn}(\widehat{v}_X)\sqrt{2}e(\mathcal{T}_a\widehat{\tau}_2^a + \mathcal{T}_o\widehat{\tau}_2^o)\right]A, \tag{4.2.4b}$$

where the partial derivatives are given in subscript notation. Equation (4.2.4a) is an ordinary differential equation (ODE) that can be solved to give a solution for $A$ the ice concentration. This solution can be substituted into equation (4.2.4b) to give a solution for $\widehat{v}$ the component of the sea ice drift velocity parallel to the sea ice edge. Approximating $g(A)$ by $g(A) = A^c$, equation (4.2.4a) can be integrated to give

$$A = \left[\text{sgn}(\widehat{v}_X)\frac{1-c}{c}\frac{2\sqrt{2}e\mathcal{L}_R}{p^* h}\int(\mathcal{T}_a\widehat{\tau}_2^a + \mathcal{T}_o\widehat{\tau}_2^o)dx\right]^{\frac{1}{c-1}}. \tag{4.2.5}$$

This produces solutions for applied forcing which is either constant or only dependant upon $X$. In these cases, $A$ behaves like a real root. For a value of $c = 20$ this is a 19th root.

However when the applied stresses have a more sophisticated relationship, such as equation (3.2.6), the integral on the RHS of equation (4.2.5) will contain continuous functions of $\widehat{v}_X$. This method does not work for such cases and a more sophisticated model is needed to obtain solutions. This is created by using a non zero value for the normal ice velocity.

**Non Zero Normal Ice Velocity**

Allowing the ice to move normal to the sea ice edge introduces complexity to equation (2.2.4). As the sea ice edge is compacted by on-ice winds and currents, $u$ is taken as small and positive for $x$ increasing into the pack. This value is taken to be constant throughout the solution with $\partial u/\partial x = 0$. The steady state components of equation (2.2.4) under these simplifications become

$$\begin{aligned} 0 = &\quad \rho_I h v + A(\tau_1^a + \tau_1^o) + \sigma_{11x}, \text{and} \\ u v_x = &-\rho_I h u + A(\tau_2^a + \tau_2^o) + \sigma_{12x} \end{aligned} \tag{4.2.6}$$

with $m = \rho_I h$ as in equation (4.2.1). Using the stress tensor components in equation (4.2.2) and scaling in section 4.2.1, equation (4.2.6) can be non-dimensionalised to give

$$0 = \quad f_c \mathcal{L}_R U_I \widehat{v} + \frac{\mathcal{L}_R}{\rho_I h}(\mathcal{T}_a \widehat{\tau}_1^a + \mathcal{T}_o \widehat{\tau}_1^o)A - \frac{p^*}{2\rho_I}\frac{\partial g}{\partial A}\frac{\partial A}{\partial X}, \text{and} \tag{4.2.7a}$$

$$U_I^2 \widehat{u}\frac{\partial \widehat{v}}{\partial X} = -f_c \mathcal{L}_R U_I \widehat{u} + \frac{\mathcal{L}_R}{\rho_I h}(\mathcal{T}_a \widehat{\tau}_2^a + \mathcal{T}_o \widehat{\tau}_2^o)A + \frac{p^*}{2\sqrt{2}e\rho_I}\text{sgn}(\widehat{v}_X)\frac{\partial g}{\partial A}\frac{\partial A}{\partial X}. \tag{4.2.7b}$$

These two equations can be combined to give a system of two ODEs to solve for $\widehat{v}$ and $A$ with

$$g_A A_X - \alpha_1[X, \widehat{v}]A - \alpha_2 \widehat{v} = 0 \text{ and} \tag{4.2.8a}$$

$$\widehat{v}_X - \beta_1 \text{sgn}(\widehat{v}_X)\widehat{v} - \beta_2[X, \widehat{v}, \text{sgn}(\widehat{v}_X)]A + \beta_3 = 0, \tag{4.2.8b}$$

where

$$\begin{aligned} \alpha_1[X, \widehat{v}] &= 2\frac{\mathcal{L}_R}{p^* h}\mathbf{T}_1[X, \widehat{u}, \widehat{v}], \\ \alpha_2 &= 2\frac{\rho_I f_c \mathcal{L}_R U_I}{p^*}, \\ \beta_1 &= \frac{f_c \mathcal{L}_R}{U_I \widehat{u}\sqrt{2}e}, \\ \beta_2[X, \widehat{v}, \text{sgn}(\widehat{v}_X)] &= 2\frac{\mathcal{L}_R}{\rho_I h U_I^2 \widehat{u}}\left(\mathbf{T}_1[X, \widehat{u}, \widehat{v}] + \frac{\text{sgn}(\widehat{v}_X)}{\sqrt{2}e}\mathbf{T}_2[X, \widehat{u}, \widehat{v}]\right) \text{ and} \\ \beta_3 &= \frac{f_c \mathcal{L}_R}{U_I}. \end{aligned} \tag{4.2.9}$$

The functions $\mathbf{T}_1[X,\widehat{u},\widehat{v}] = \mathcal{T}_a\widehat{\tau}_1^a[X] + \mathcal{T}_o\widehat{\tau}_1^o[X,\widehat{u},\widehat{v}]$ and $\mathbf{T}_2[X,\widehat{u},\widehat{v}] = \mathcal{T}_a\widehat{\tau}_2^a[X] + \mathcal{T}_o\widehat{\tau}_2^o[X,\widehat{u},\widehat{v}]$ are derived from the appied stresses with the scaling terms $\mathcal{T}_a = U_A^2\rho_a C_a$, $\mathcal{T}_o = U_O^2\rho_o C_o$. The components of the applied stress terms calculated from equations (4.1.1) and (3.2.6) with

$$\begin{aligned}
&\widehat{\tau}_1^a = \widehat{u_{\widehat{n}}^a}\sqrt{\widehat{u_{\widehat{n}}^a}^2 + \widehat{v_{\widehat{n}}^a}^2}, \quad \widehat{\tau}_2^a = \widehat{v_{\widehat{n}}^a}\sqrt{\widehat{u_{\widehat{n}}^a}^2 + \widehat{v_{\widehat{n}}^a}^2}, \\
&\widehat{\tau}_1^o = \left(\widehat{u_{\widehat{n}}^o} - \frac{U_I}{U_O}\widehat{u}\right)\sqrt{\left(\widehat{u_{\widehat{n}}^o} - \frac{U_I}{U_O}\widehat{u}\right)^2 + \left(\widehat{v_{\widehat{n}}^o} - \frac{U_I}{U_O}\widehat{v}\right)^2} \text{ and} \\
&\widehat{\tau}_2^o = \left(\widehat{v_{\widehat{n}}^o} - \frac{U_I}{U_O}\widehat{v})\right)\sqrt{\left(\widehat{u_{\widehat{n}}^o} - \frac{U_I}{U_O}\widehat{u}\right)^2 + \left(\widehat{v_{\widehat{n}}^o} - \frac{U_I}{U_O}\widehat{v}\right)^2},
\end{aligned} \tag{4.2.10}$$

with the scaled atmosphere and ocean velocites $U_A(\widehat{u_{\widehat{n}}^a}, \widehat{v_{\widehat{n}}^a}) = (u_{\widehat{n}}^a, u_{\widehat{n}}^a)$ and $U_O(\widehat{u_{\widehat{n}}^o}, \widehat{v_{\widehat{n}}^o}) = (u_{\widehat{n}}^o, u_{\widehat{n}}^o)$. The ocean stresses have had the turning angle set to zero. Due to the dependency of the ocean jet upon the $u_{\text{diff}}^2$ term (see section 4.1.2), the ocean velocity term parallel to the ice edge is a function of typical ocean and ice speeds, i.e. $\widehat{v_{\widehat{n}}^o} = \widehat{v_{\widehat{n}}^o}[\tilde{\mathbf{u}}_O, \tilde{\mathbf{u}}_I]$.

## 4.3 Free Drift at the Extreme Ice Edge

At the extreme edge of the sea ice pack, the ice concentration approaches zero. This makes the ice ocean mixture model described in section 2.2.3 no longer applicable. The ice movement can be modelled as a free drift, where the ice floes no longer have any meaningful interactions and are assumed to make no modification to the momentum over a large length scale. These interactions are considered by the ice stress tensor in equation (2.2.4). The magnitude of the internal stresses calculated by the viscous-plastic rheology are shown to be insignificant compared to the applies stresses in section 4.3.1 removing the need for an ice stress tensor. The movement of the individual ice floes is now considered rather than the sea ice - ocean mixture layer removing the dependance upon the ice concentration. The resulting free drift momentum balance is that described in equation (2.2.3). The two sea ice momentum balances in equations (2.2.4) and (2.2.3) need to be matched in order to fully model the sea ice edge. This is done using the mathemtical techniques of length contraction and variable expansion.

### 4.3.1 Matching the Free Drift and Ice Pack

To match the two momentum balances the controlling components are analysed. The ice concentration $A$ is expanded polynomially in $\epsilon$. Using small $\epsilon$ one can view which terms take precedent through the order of $\epsilon$ and the constants associated with them. This technique is used in fluid dynamics in laminar and boundary layer flows. A full documentation can be found in Dyke (1975). Convention labels the region in which the full order of the governing equations are preserved as the outer solution. The region in which the equations are scaled and the highest order term ignored is labelled as the inner solution. This labeling is confusing for this situation as it conflicts with the outer part of the MIZ which it represents. The inner and outer terminology shall not be used.

We take

$$A = A_0 + A_1\epsilon + A_2\epsilon^2 + \ldots, \qquad \frac{\partial A}{\partial X} = A_{0X} + A_{1X}\epsilon + A_{2X}\epsilon^2 + \ldots, \tag{4.3.1}$$

where $A_n$ are functions of $X$ and $\epsilon << 1$ is a constant. The series differentiate linearly. The length variable $X$ is replaced with the length contracted variable $\mathcal{X}$ where $X = \epsilon^\alpha \mathcal{X}$ with $\alpha > 0$. This is carried through to the derivatives where

$$\frac{\partial}{\partial X} = \frac{\partial}{\partial \mathcal{X}}\frac{\partial \mathcal{X}}{\partial X} = \epsilon^{-\alpha}\frac{\partial}{\partial \mathcal{X}}. \tag{4.3.2}$$

The expansion in powers of $\epsilon$ along with the change of variables has the effect of focusing on the point $X = 0$, where $A = A_0, \widehat{u} = u_0, \widehat{v} = v_0$. For the case of the sea ice edge, the ice concentration is zero with $A_0 = 0$. The first order (in $\epsilon$) change to these terms will happen beyond a specific length scale defined by $\epsilon$ and $\alpha$.

The non-dimensional steady state momentum balance in equation (4.2.7) is used with modification. $\widehat{u}$ is no longer kept constant as the assumption $\widehat{u}_X \equiv 0$ does not hold for free drifting ice near the the open ocean. The terms $\sigma_{11X}$ and $\sigma_{12X}$ from equation (4.2.2) need expanding. The function $g(A)$ in the ice pressure term (see equation (4.2.2)) is approximated by $g(A) = A^c$ so to fit with the polynomial form of equation (4.3.1).

From equations (A.2.2) and (A.2.3) the tensor components become

$$\begin{aligned}\sigma_{11} &= \frac{1}{2}p^* h A^c \left[\frac{(1+e^{-2})\widehat{u}_{\mathcal{X}}\epsilon^{-\alpha}}{\{(1+e^{-2})\widehat{u}_{\mathcal{X}}^2\epsilon^{-2\alpha} + 2e^{-2}\widehat{v}_{\mathcal{X}}^2\epsilon^{-2\alpha}\}^{\frac{1}{2}}} - 1\right] \text{ and} \\ \sigma_{12} &= \frac{1}{2}p^* h A^c \frac{e^{-2}\widehat{v}_{\mathcal{X}}\epsilon^{-\alpha}}{\{(1+e^{-2})\widehat{u}_{\mathcal{X}}^2\epsilon^{-2\alpha} + 2e^{-2}\widehat{v}_{\mathcal{X}}^2\epsilon^{-2\alpha}\}^{\frac{1}{2}}}.\end{aligned} \tag{4.3.3}$$

In these two terms the $\epsilon^{-\alpha}$ values cancel out. The terms $\mathcal{D}_{11}$ and $\mathcal{D}_{12}$ shall be used to simplify the equations with

$$\begin{aligned}\mathcal{D}_{11} &= \left[\frac{(1+e^{-2})\widehat{u}_{\mathcal{X}}}{\{(1+e^{-2})\widehat{u}_{\mathcal{X}}^2 + 2e^{-2}\widehat{v}_{\mathcal{X}}^2\}^{\frac{1}{2}}} - 1\right] \text{ and} \\ \mathcal{D}_{12} &= \frac{e^{-2}\widehat{v}_{\mathcal{X}}}{\{(1+e^{-2})\widehat{u}_{\mathcal{X}}^2 + 2e^{-2}\widehat{v}_{\mathcal{X}}^2\}^{\frac{1}{2}}}.\end{aligned} \tag{4.3.4}$$

Substituting equations (4.3.4) into equations (4.3.3), the $\mathcal{X}$ derivatives (notated by $\sigma_{11,X}$ for example) of the stress tensor terms become

$$\begin{aligned}\sigma_{11,X} &= \epsilon^{-\alpha}\sigma_{11,\mathcal{X}} \qquad (4.3.5a)\\ &= \epsilon^{-\alpha}\frac{1}{2}p^* h\left[cA^{c-1}A_{\mathcal{X}}\mathcal{D}_{11} + A^c\mathcal{D}_{11,\mathcal{X}}\right], \text{ and} \\ \sigma_{12,X} &= \epsilon^{-\alpha}\sigma_{12,\mathcal{X}} \qquad (4.3.5b)\\ &= \epsilon^{-\alpha}\frac{1}{2}p^* h\left[cA^{c-1}A_{\mathcal{X}}\mathcal{D}_{12} + A^c\mathcal{D}_{12,\mathcal{X}}\right].\end{aligned}$$

The $A^n$ terms have yet to be expanded. Upon expansion

$$\begin{aligned}A^n &= (A_0 + A_1\epsilon + A_2\epsilon^2 + \ldots)^n \qquad (4.3.6)\\ &= {A_0}^n + \epsilon\binom{n}{1}{A_0}^{n-1}A_1 + \epsilon^2\left[\binom{n}{2}{A_0}^{n-2}{A_1}^2 + \binom{n}{1}{A_0}^{n-1}A_2\right] + \ldots \quad .\end{aligned}$$

| Parameter | Value |
|---|---|
| $c$ | 20 |
| $e$ | 2 |
| $\mathcal{L}_{RA}$ | 75 000 m |
| $\mathcal{L}_{RO}$ | 6 000 m |
| $U_I$ | 0.01 m s$^{-1}$ |
| $U_O$ | 0.1 m s$^{-1}$ |
| $f_c$ | $10^{-4}$ s$^{-1}$ |
| $\rho_I$ | 900 kg m$^{-3}$ |
| $p^*$ | 27 500 N m$^{-1}$ |
| $h$ | 1 m |
| $\mathcal{T}_a, \mathcal{T}_o$ | 0.5 N m$^{-2}$ |

Table 4.1: Typical values of constants for the sea ice edge.

For the case when $A_0 = 0$ equations (4.3.5a) and (4.3.6) give

$$\begin{aligned}\sigma_{11,\mathcal{X}} = \epsilon^{-\alpha}\frac{1}{2}p^*h\Bigg\{ & \quad \epsilon^c[{A_1}^c\mathcal{D}_{11,\mathcal{X}} + cA_{1,\mathcal{X}}{A_1}^{c-1}\mathcal{D}_{11}] \\ & +\epsilon^{c+1}\Bigg[A_1^{c-1}A_2\binom{c}{1}\mathcal{D}_{11,\mathcal{X}} + c{A_1}^{c-2}\Big(A_2A_{1,\mathcal{X}}\binom{c-1}{1}\mathcal{D}_{11} \\ & \qquad +cA_1A_{2,\mathcal{X}}\mathcal{D}_{11}\Big)\Bigg] + \dots\Bigg\}, \qquad (4.3.7) \\ = \epsilon^{c-\alpha}\frac{1}{2}p^*h\widehat{\sigma}_{11,\mathcal{X}}\end{aligned}$$

with a similar result for equation (4.3.5b). Equation 4.3.7 gives $\sigma_{11,\mathcal{X}}$ and $\sigma_{12,\mathcal{X}}$ as $\mathrm{o}(p^*h\epsilon^{c-\alpha})$ to leading order as long as $\mathcal{D}_{11}$ and $\mathcal{D}_{12}$ and their derivatives and resultantly $\widehat{\sigma}_{11,\mathcal{X}}$ are no greater than $\mathrm{o}(1)$. This assumption is reasonable for any steady solution as otherwise there would have to be a large discrepancy between ${u_\mathcal{X}}^2$ and ${v_\mathcal{X}}^2$. This is true for the solutions obtained in chapter 5.

The order of each component of equation (2.2.4) can now be expressed. The length contracted form of the $x$ component is

$$U_I^2\widehat{u}\widehat{u}_\mathcal{X} = f_c\mathcal{L}_RU_I\widehat{v} + \frac{\mathcal{L}_R}{\rho_Ih}(\mathcal{T}_a\widehat{\tau}_1^a + \mathcal{T}_o\widehat{\tau}_1^o)A + \frac{p^*}{2\rho_I}\epsilon^{c-\alpha}\widehat{\sigma}_{11,\mathcal{X}}, \qquad (4.3.8)$$

with a similar result for the $y$ component. A value for $\alpha$ is selected to make the stress tensor (far right of equation 4.3.8) small compared to the other terms. This is achieved by considering the order of each

term along with values for each constant from table 4.1. The order of the constants in front of each term in equation (4.3.8) can now be calculated over scales associated with an atmospheric jet (subscript $A$) and oceanic jet (subscript $O$), ie.

$$\begin{aligned} U_I^2 &\approx \mathrm{o}(10^{-4}), & U_O^2 &\approx \mathrm{o}(10^{-2}), \\ f_c \mathcal{L}_{RA} U_I &\approx \mathrm{o}(10^{-1}), & f_c \mathcal{L}_{RO} U_O &\approx \mathrm{o}(10^{-1}), \\ \frac{\mathcal{L}_{RA}}{\rho_I h}(\mathcal{T}_a \widehat{\tau}_1^a + \mathcal{T}_o \widehat{\tau}_1^o) &\approx \mathrm{o}(10^2), & \frac{\mathcal{L}_{RO}}{\rho_I h}(\mathcal{T}_a \widehat{\tau}_1^a + \mathcal{T}_o \widehat{\tau}_1^o) &\approx \mathrm{o}(10^0), \text{ and} \\ \frac{p^*}{2\rho_I} &\approx \mathrm{o}(10^3). \end{aligned}$$

These values can be used to balance the order of the each component along with the constants associated with it. There is a different balance for the atmospheric jet system (over $\mathcal{L}_{RA}$, equation (4.3.9a)) and ocean jet system (over $\mathcal{L}_{RO}$, equation (4.3.9b)) with

$$\mathrm{o}(10^{-4}\epsilon^{-\alpha}) = \mathrm{o}(10^{-1}) + \mathrm{o}(10^2\epsilon) + \mathrm{o}(10^3\epsilon^{c-\alpha}) \text{ and} \tag{4.3.9a}$$

$$\mathrm{o}(10^{-2}\epsilon^{-\alpha}) = \mathrm{o}(10^{-1}) + \mathrm{o}(\epsilon) + \mathrm{o}(10^3\epsilon^{c-\alpha}). \tag{4.3.9b}$$

The atmosphere can be balanced (removing the stress tensor) with $\epsilon = \mathrm{o}(10^{-2})$ and $\alpha = 2$. This makes the order of the stress tensor $< \mathrm{o}(10^{-10})$ and negligible. This selection corresponds to a length contraction of $\approx 0.01\%$. For length scales shown in table 4.1 this is the outer $\approx 75$ m of the MIZ. The ocean system can be similarly balanced with $\epsilon = \mathrm{o}(10^{-1})$ and $\alpha = 2$ having the same result with the stress tensor term. The length contraction in this case is for the outer 60 m of the MIZ.

The expansion shows how the viscous plastic dynamics of the sea ice pack are similar to free drift at the sea ice edge. This is achieved by assuming that the ice concentration reaches zero and leaves the ice velocity unchanged. The similarity is over a distance of 75m for a sea ice edge under an atmospheric jet and 60m over an ocean jet. Boundary conditions for the ice pack can be calculated using the free drift momentum balance.

### 4.3.2 Application to the Sea Ice Edge

The same simplifications used for the ice pack (section 4.2.1) are applied to the free drift momentum balance. This models the ice movement at the extreme ice edge, allowing the normal velocity $\widehat{u}$ to be unconstrained. As this region is thin compared to the scales of atmospheric and oceanic drag variation (Rossby radius $\mathcal{L}_{R(A,O)}$), the velocity solution can be taken as constant throughout, removing all spatial derivatives. The peak values of atmosphere and ocean velocity (at $X = X_{\text{peak}}$) are used for the applied stresses. The ice velocities $(\widehat{u}, \widehat{v})$ can be calculated from the components of equation (2.2.3) with all spatial and time derivatives set to zero. These are a set of simultaneous equations with

$$\begin{aligned} 0 = \quad & f_c \widehat{v} + \frac{1}{\rho_I h U_I} \mathbf{T}_1[X_{\text{peak}}, \widehat{u}, \widehat{v}] \text{ and} \\ 0 = & -f_c \widehat{u} + \frac{1}{\rho_I h U_I} \mathbf{T}_2[X_{\text{peak}}, \widehat{u}, \widehat{v}]. \end{aligned} \tag{4.3.10}$$

In order to calculate the stress terms $(\mathbf{T}_1, \mathbf{T}_2)$, typical ice and ocean velocities are needed to calculate $u^2_{\text{diff}}$. The typical ocean velocity $\tilde{\mathbf{u}}_O = (\sin\phi, \cos\phi)$ is taken as the non-dimensional far field ocean velocity, the typical ice velocity $\tilde{\mathbf{u}}_I = (\widehat{u}, \widehat{v})$ is equated to the ice velocity to be solved for. The solution gives boundary conditions for the sea ice pack (see section 4.3.3). The boundary conditions give typical ice and ocean velocities and thus a value of $u^2_{\text{diff}}$ for the sea ice pack solution.

### 4.3.3 Boundary Conditions

Boundary conditions are needed to find a solution for the ice pack. These conditions are derived from the free drift system in section 4.3.2 along with an imposed low, nonzero ice concentration $A$ chosen to represent the sea ice edge. A value of $A = 0$, which would represent the open ocean results in the solution $A = 0$ for the whole domain and we choose $A = 0.1$. The free drift system, however gives values for $\widehat{u}, \widehat{v}$ which are inconsistent with the assumptions in section 4.2.1. The parallel component of the velocity $(\widehat{v})$ is consistent though the normal component $(\widehat{u})$ is too high to match to the low normal velocity set in section 4.2.1. A discontinuity in the normal velocity is required. A lower value for $\widehat{u}$ can be calculated from equation (4.2.8b) to maintain continuity in the $x$ direction. Prescribed values of $A = 0.1$ (as before) and $\widehat{v}$ (from the free drift solution) are used. Values for forcing functions $\mathbf{T}_1, \mathbf{T}_2$ are used as in the free drift solution. The derivative

$\widehat{v}_X$ is set to zero, to maintain continuity, and the derivative $A_X$ is set to be high, anticipating a sharp increase in ice concentration. $\widehat{u}$ is then calculated from

$$0 = -f_c \mathcal{L}_R U_I \widehat{u} + \frac{\mathcal{L}_R}{\rho_I h} A \mathbf{T}_2[X_{\text{peak}}, \widehat{u}, \widehat{v}] A + \frac{p^*}{2\sqrt{2} e \rho_I} \text{sgn}(\widehat{v}_X) g_A A_X, \tag{4.3.11}$$

with $\mathbf{T}_1$ calculated as for the free drift in section 4.3.2, i.e. $u^2_{\text{diff}}$ is a function of $\widehat{u}$. For the results in chapter 5, $\widehat{u}$ for the analytical model is approximately 10% of the value for the free drift solution.

For the pack solution $\widehat{v}$ is expected to be at its highest at the extreme edge of the ice pack. This gives $\widehat{v}_X < 0$ with $\text{sgn}(\widehat{v}_X) = -1$ (in equation (4.2.8b)) for all $X$.

# CHAPTER 5

# RESULTS FROM THE ANALYTICAL MODEL

A model of sea ice drift at the sea ice edge has been described in chapter 4. This chapter contains results from that model. The techniques used in performing experiments with the analytical model are described in section 5.1. Results from experiments with an atmospheric jet are in section 5.2.1 with detailed plots from a demonstration experiment (figure 5.1) and an analysis of changing parameters (figure 5.2). Results from experiments with an ocean jet are presented similarly with a demonstration experiment (figure 5.3) and changing parameters (figures 5.4, 5.5 and 5.6). Sea ice drift during both atmospheric and oceanic jet formation has been considered and four examples are presented in section 5.2.3. The nature of the sea ice during jet formation is investigated in section 5.2.4.

## 5.1 Solving Methods

The system of equations (4.2.8) in chapter 4 can be used to model the dynamics of the sea ice edge. The boundary conditions are set by matching the free drift solution (equation (4.3.10)) with the ice pack momentum balance (equation (4.3.11)).

The equations are solved over a simplified domain. The domain has the ice edge at $X = 0$ defined by

a low ice concentration of $A = 0.1$. The system is solved for $X > 0$ over the distance of $> 2\mathcal{L}_{R(A,O)}$ to include all of the sea ice under the influence of the atmospheric or oceanic jets. The jets are centred about $X = 0$ with $\widehat{n}$ aligned with the $X$ axis. When both jets are applied, the oceanic jet is a function of $(\mathcal{L}_{RA}/\mathcal{L}_{RO})\widehat{n}$ to allow for the different scales of the two jets. Using simplifications the system can be solved over this domain.

### 5.1.1 Approximation and Linearisation

The coefficient of the highest order derivative in equation (4.2.8a) $(A_X)$ is a nonlinear function of $A$. This non linearity comes from the $g(A)$ function and makes the system of equations difficult to solve using simple numerical methods. This has been addressed by linearising this function over many domains. Approximating $g(A)$ by a piecewise continuous set of lines causes the derivative $\partial g/\partial A$ in equation (4.2.8a) to be constant in each domain. The system can now be solved in each domain, matching the boundary conditions of each domain to its neighbours to create a complete solution.

Define the open set $\mathcal{Q}_A = [0, 1]$ which is subdivided into $n$ open sets $\mathcal{Q}_i = [A_{i-1}, A_i]$ by the monotonically increasing series $\{A_0, A_1, \ldots A_n\}$, where $A_0 = 0$, $A_n = 1$ and $\bigcup_{i=1}^{n} \mathcal{Q}_i = \mathcal{Q}_A$. This allows us to define the set of functions

$$g_i(A) = \left\{ m_i A + c_i \text{ s.t. } \begin{array}{ll} g_i(A_{i-1}) & = g(A_{i-1}) \\ g_i(A_i) & = g(A_i) \\ |g(A) - g_i(A)| < \varepsilon_i & \forall A \in \mathcal{Q}_i \end{array} \right\} \tag{5.1.1}$$

where $\varepsilon_i << 1$ is the maximum error for each function. As both the functions $g_i(A)$ and $g(A)$ are monotonic increasing, the error can be contained by having the size of domain $\mathcal{Q}_i$ (given as $A_i - A_{i-1}$]) sufficiently small. Approaching the limit $A_{i-1} \to A_i$ results in $g_i(A_{i-1}) = g(A_{i-1}) \to g_i(A_i) = g(A_i)$. This gives $|g(A) - g_i(A)| \to 0$.

A non uniform subset distribution has been chosen. Set width decreases as $A$ approaches 1. This allows the maximum error $\varepsilon_i$ to be small and approximately equal for all $i$, maintaining the accuracy of the complete solution over all subsets.

The solution is started at $X = 0$. Boundary conditions are taken for $A$ and $\widehat{v}$ (derived in section 4.3.3) and equations (4.2.8) are solved over $\mathcal{Q}_1$ until $A = A_1$. Values for $A$, $\widehat{v}$ and $X$ at this point are used as boundary conditions to solve over $\mathcal{Q}_2$. This process is repeated to give a complete solution for the ice edge.

## 5.2 Results

Solving equations (4.2.8) over the domain in equation (5.1.1) gives values for the lateral ice velocity $v$ and ice concentration $A$. These values are defined for the whole solution. The movement of the ice balances the rate of change in momentum induced by the external stresses. This rate of change is purely spatial in the $x$ direction with all other derivatives zero (i.e. $\partial/\partial t = 0, \partial/\partial y = 0$).

For each experiment, three conditions are considered and solved for. The first is for no jet and the second and third are a jet in the northern and southern hemisphere. This is analogous to having runs with $\phi^\circ$ and $180 - \phi^\circ$ allowing all values of $0^\circ \leq \phi^\circ \leq 180^\circ$ to be considered. The orientation of the axes in this model only allows movement in the positive $y$ direction as defined in figure 4.1, constraining the far field forcing to have an approach angle of $0^\circ \leq \phi^\circ \leq 90^\circ$.

### 5.2.1 Atmospheric Jet Formation

Demonstration calculations are done for an approach wind of 5 $\text{ms}^{-1}$ at 45° to the ice edge. The calculations are repeated for both the northern and southern hemispheres, giving the negative and positive sides of the jet perturbations respectively (see section 3.1 for the jet shape). This gives similar results to repeating the experiment with winds at 45° and 135° to the ice edge. For the angle selected, the ice edge in the southern hemisphere experiences the stronger jet (figure 5.1(b)). The stress balance for the southern hemisphere has been plotted. The applied stresses are the dominant forces within the balance (figure 5.1 (c) and (d)), with the atmospheric stress balanced by the ocean stress (acting opposite to the ice motion due to the still ocean) with a mall contribution from the internal stresses. The internal stress components in figures 5.1 (c) and (d) have a saw tooth appearance due to the approximation methods used to solve the system (section 5.1.1). This profile can be smoothed by approximating the internal stresses using the same method as used for $g(A)$ in section 5.1.1. This is the solid blue line in the stress plots which lies at the centre of the varying dashed

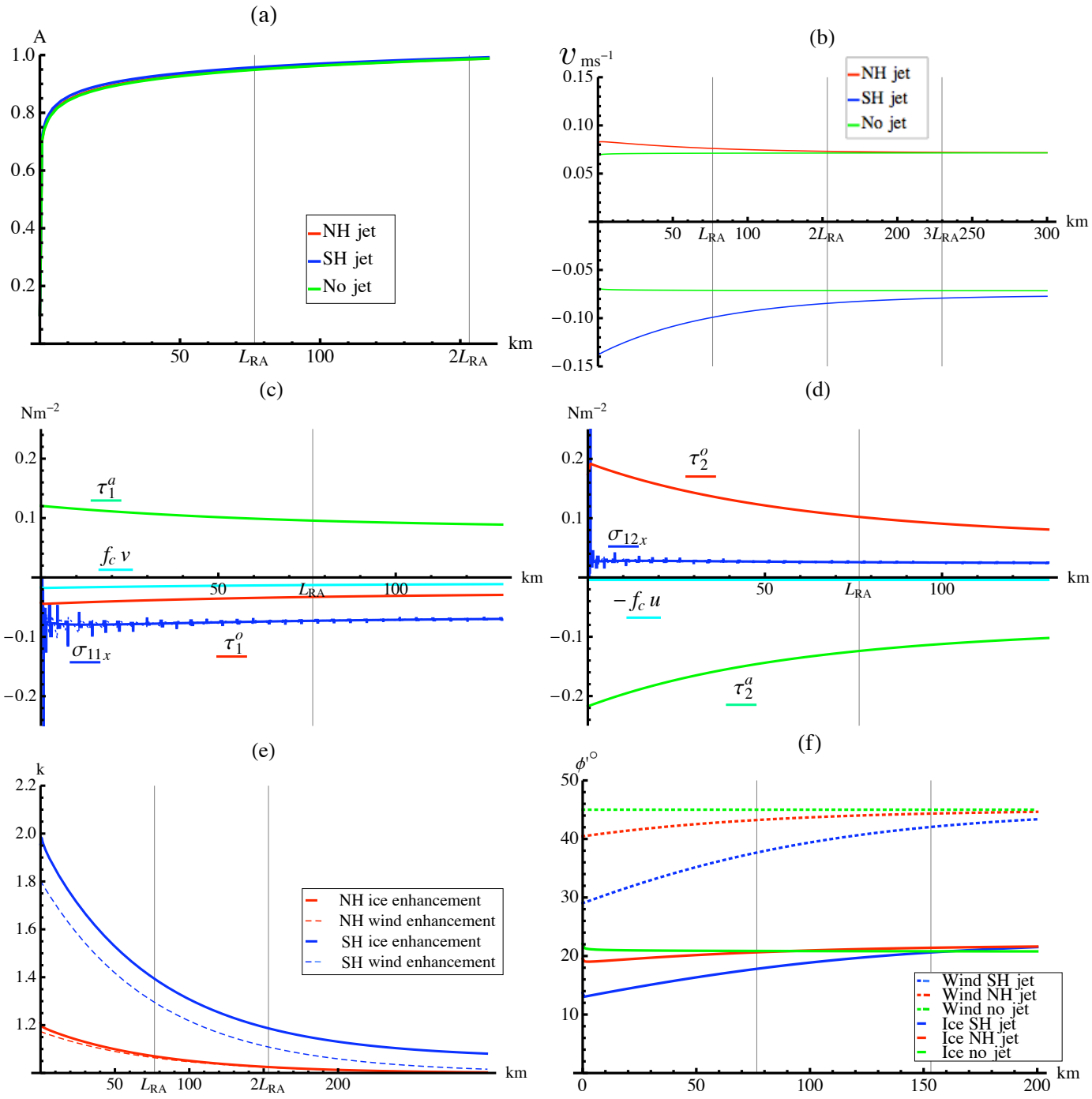


Figure 5.1: Atmospheric jet formation with $\phi = 45°$ and $U_A = 5$ m s$^{-1}$. Plot (a) is the ice concentration $A$, plot (b) is the dimensional lateral ice velocities $v$ for four cases (see legend, both no jet cases are green) with the southern hemisphere case is plotted negative to the $y$ axis to ease comparison to chapter 6. Plots (c) ($x$ direction) and (d) ($y$ direction see figure 4.1) are the dimensional stress components for the southern hemisphere solution. Plot (e) is the enhancement factor $k$ for the parallel component of the wind and ice velocities. Plot (f) is the angle $\phi\prime$ between the wind (dashed) and ice (solid) motion and the ice edge.

blue line. The Coriolis acceleration acts normal to the ice edge against the perturbed winds which compress it, though is small compared to the other stresses.

The atmospheric stress is at its peak at the ice edge, decaying away to the far field value into the ice pack. This decay is experienced by the ice velocity. The lateral component of the sea ice velocity is at its highest at the ice edge, and decays away over the same distance as the atmospheric stress ($\approx 2\mathcal{L}_{RA}$ see figure 5.1(b)). The ice motion when no jet is present gives a constant value for the lateral velocity across the solution (green lines in figure 5.1(b)). When the atmospheric jet is present, the ice speed decays to this value. Comparing the jet, and no jet solutions gives an enhancement factor $k = v_{\text{jet}}/v_{\text{no jet}}$, where $k = 1$ is for no enhancement and $k > 1$ is for positive enhancement or an increase in velocity. An atmospheric velocity enhancement factor can be calculated in the same way. The atmosphere and ice velocity enhancement have a similar same size and shape. The wind (dashed lines) and ice drift (solid lines) in figure 5.1(e) for the northern hemisphere are identical with a small difference (<20% of the sea ice enhancement) for the southern hemisphere. As the enhancement to the wind and also the sea ice velocity is purely parallel to the sea ice edge, the direction of motion is modified. Figure 5.1 (f) shows the modified angle of incidence ($\phi\prime$ see figure 4.1) between the wind and sea ice drift and the sea ice edge. For all the cases shown, the ice drift direction is closer to parallel to the ice edge than the wind above it. This is due to the compaction of the sea ice edge restricting ice motion normal to the ice edge.

The ice concentration increases to around 70% over a short distance from the sea ice edge ($< 1$ km) before the increase slows (see figure 5.1 (a)). This shape is similar to the 19th root in equation (4.2.5) discussed in section 4.2.1 and is true for all the calculations presented.

The increased ice drift caused by the formation of the atmospheric jet increases the ice transport parallel to the ice edge. This can be measured by integrating the dimensional ice velocity parallel to the ice edge over the region of the jet, i.e. for 0 km $\leq x \leq 3\mathcal{L}_{RA}$ km. The velocity is multiplied by the ice concentration to give the sea ice fraction of the mixture layer. As the thickness of the ice is constant in this model, the transport is given as the horizontal area of sea ice per unit time $\mathcal{A}_{\text{transport}}$ with

$$\mathcal{A}_{\text{transport}} = \int_0^{3\mathcal{L}_{RA}} Avdx \tag{5.2.1}$$

Where $A$ is the ice concentration and $v$ is the component of the dimensional ice drift velocity parallel to the sea ice edge. The case of no jet has a parallel drift of $\approx 50$ km$^2$ hr$^{-1}$ for the outer $3\mathcal{L}_{RA}$ of the sea ice edge. The atmospheric jet formation increases this drift by $\approx 20$ km$^2$ hr$^{-1}$ for a jet in the southern hemisphere and $\approx 3$ km$^2$ hr$^{-1}$ for the northern hemisphere.

As the angle of approach wind changes so does the jet intensity (section 3.1.3). This relationship to the angle of approach is transferred to the ice jet through the atmospheric stress. This gives the lateral ice velocity enhancement a similar profile to the lateral wind velocity enhancement, see figure 5.2(a) which is at 5 km from the edge of the ice pack, near the centre of the jet. For an approach angle which gives a significant lateral velocity component the profiles share a similar curve. As the lateral component of the ice drift velocity become close to zero ($60^\circ < \phi < 120^\circ$ in both jet and no-jet cases), internal stresses and the Coriolis accelerations take a greater role in the momentum balance. This can cause the non-jet case to have a near zero value for the lateral velocity (the cause of the lump at $\phi = 110^\circ$). Also as the wind approaches an angle normal to the ice edge, the jet perturbation can be negative, slowing the lateral motion compared to the non jet case (at $\phi = 70^\circ$). There is a discontinuity in the plot at $\phi = 90^\circ$ due to the change in sign of the second order perturbation in the wind jet calculation (see chapter 3). The second order perturbation gives a greater enhancement for $\phi > 90^\circ$ with the ice and ocean reaching the maximum perturbation limit derived from the analysis of parallel flow (equation (3.1.17)) at $\approx 15^\circ$ to the ice edge rather than $\approx 5^\circ$ for the negative perturbation ($\phi < 90^\circ$). This gives the wider plateau at $\phi = 180^\circ$. This is reversed for the southern hemisphere. The size of the plateau is also dependant upon $U_A$, with a greater size for faster wind speeds.

Changing the far field wind speed alters the jet in two ways. The symmetrical component is linearly dependant upon the approach wind speed and gives the same enhancement factor for all wind speeds. The anti-symmetrical component depends on both the wind speed and the Froude number. This gives a greater asymmetry for higher wind speeds seen in the diverging trends in figure 5.2(b). As the wind speed approaches the critical limit ($\mathcal{F}_A \to 1, U_A \to 10$ m s$^{-1}$) the asymmetric and symmetric components are of similar magnitude. This gives a one sided jet with little or even a negative perturbation (seen for $U_A > 8$ m s$^{-1}$) on the negative side and a large discontinuity about the ice edge. The spatial variability of such a jet is not

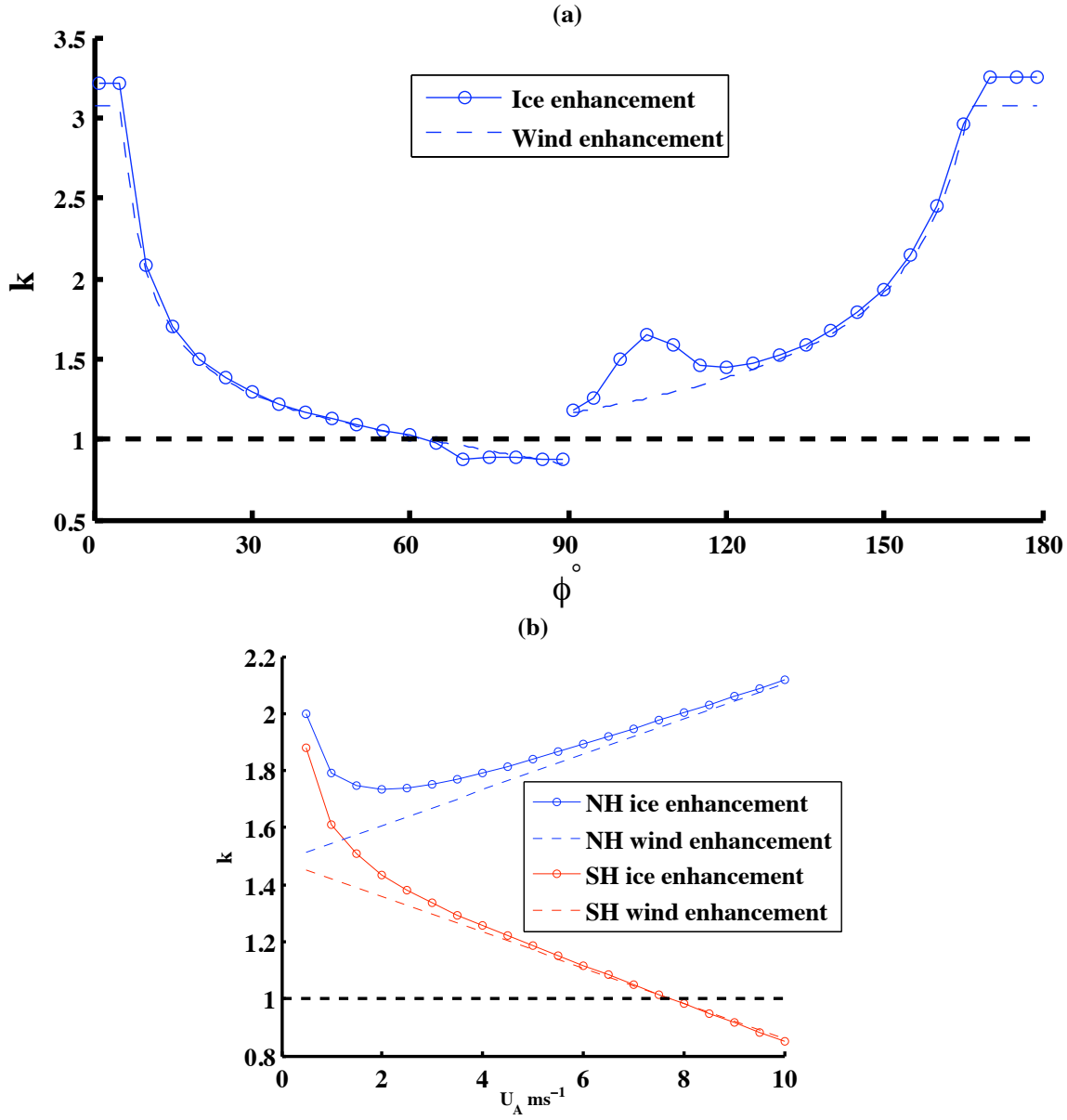


Figure 5.2: Peak enhancement factor $k$ for the lateral component of wind and ice velocities taken at 5 km from the ice edge. Plot (a) is for varying values of $\phi$ for a northern hemisphere jet, with $\phi = 0°$ and $\phi = 180°$ for purely parallel wind velocity. The far field wind speed is held constant at $U_A = 5$ m s$^{-1}$. Plot (b) is for varying values of $U_A$ with the approach angle held constant at $\phi = 45°$ (SH analogous to $180° - \phi$ with reversed Coriolis acceleration).

plotted, though the strength of a jet throughout it's extent is proportional to the strength at it's maximum. Plotting the peak enhancement at the ice edge against the approach speed gives two results seen in figure 5.2. When the positive side of the jet is over the sea ice, the ice enhancement increases linearly with wind speed. When the negative side is over the sea ice, there is a linear decrease. This linearity is not present for low wind speeds when Coriolis and internal stress components become similar to the applied stress (for $U_A < 2$ m s$^{-1}$).

### 5.2.2 Oceanic Jet Formation

The relationship between ocean jet formation and the sea ice response is more sophisticated than with the atmospheric jet as described in section 5.2.1. The applied stress from the ocean cannot be applied as with the atmospheric forcing. This is due to the ocean stress (equation (3.2.6)) and the ocean jet strength ($u^2_{\text{diff}}$ term in equation (3.2.11)) being proportional to the difference in velocity between the ice and the ocean rather than just the ocean velocity.

Demonstration calculations are done for an approach current of 0.2 m s$^{-1}$ at 30° to the ice edge. This angle has been chosen over 45° (as used for the demonstration calculations in section 5.2.1) as it produces an ocean jet of greater magnitude. The calculations are repeated for both the northern and southern hemispheres. As with the atmospheric jet, the southern hemisphere experiences the stronger jet (figure 5.3(e)). The two main components in the momentum balance are the ocean stress and the internal stress gradient (see figure 5.3 (c) and (d)). Again the internal stress components in figures 5.3 (c) and (d) have a saw tooth appearance due to the approximation methods used to solve the system (section 5.1.1). The smooth approximation to these stresses is the solid line. These components are equal throughout the solution despite the jet formation. The ice is moving faster than it does in the experiments with the atmospheric jet, giving a larger Coriolis acceleration. The ocean jet forms a sea ice jet of equal spatial size and similar intensity. This keeps the difference between the lateral ocean and ice velocities equal throughout the solution (see the difference between corresponding solid and dashed lines in figure 5.3(b)).

The ocean and ice perturbation velocities are at their peak at the ice edge, decaying away to the far field values into the ice pack over a distance of $\approx 2\mathcal{L}_{RO}$ (see figure 5.3(b)). The enhancement factor $k$ is calculated as with the atmospheric jet. The spatial shape of the ice enhancement matches the ocean

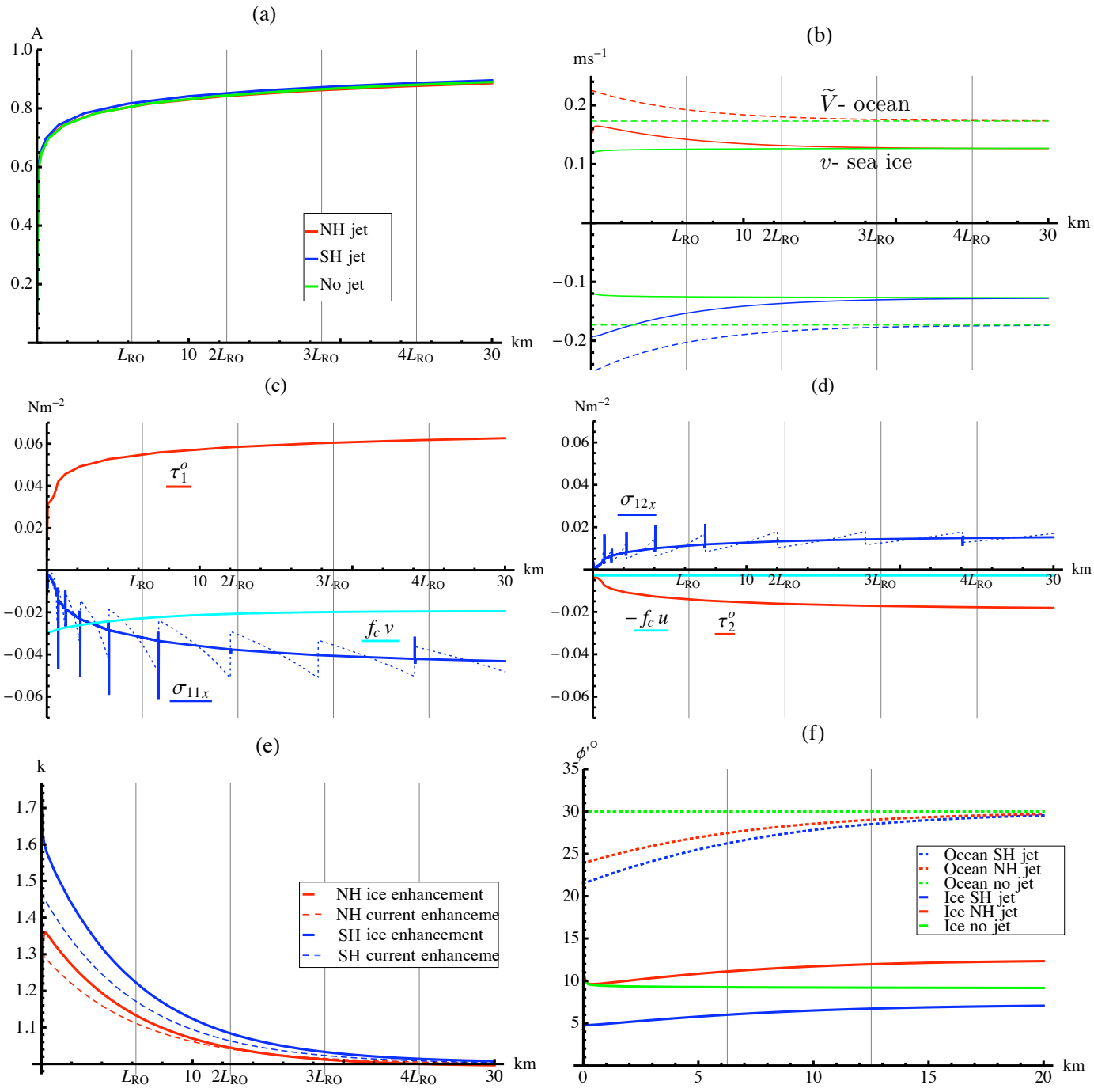


Figure 5.3: Sea ice edge response to oceanic jet formation with $\phi = 30°$ and $U_O = 0.2$ m s$^{-1}$. Plots (a) and (b) are solutions for four cases (see legend, both no jet cases green). Plot (a) is the ice concentration $A$, plot (b) is the dimensional lateral sea ice velocity $v$ (see figure 4.1) as in 5.1(b) along with the corresponding ocean velocities $\widehat{V}$ (see figure 3.2). Plot (c) ($x$ direction) and (d) ($y$ direction see figure 4.1) are the dimensional stress components for the southern hemisphere solution. Plot (e) is the enhancement factor k for the parallel component of the ocean and ice velocities. Plot (f) is the angle between motion and the ice edge as in figure 5.1(f)

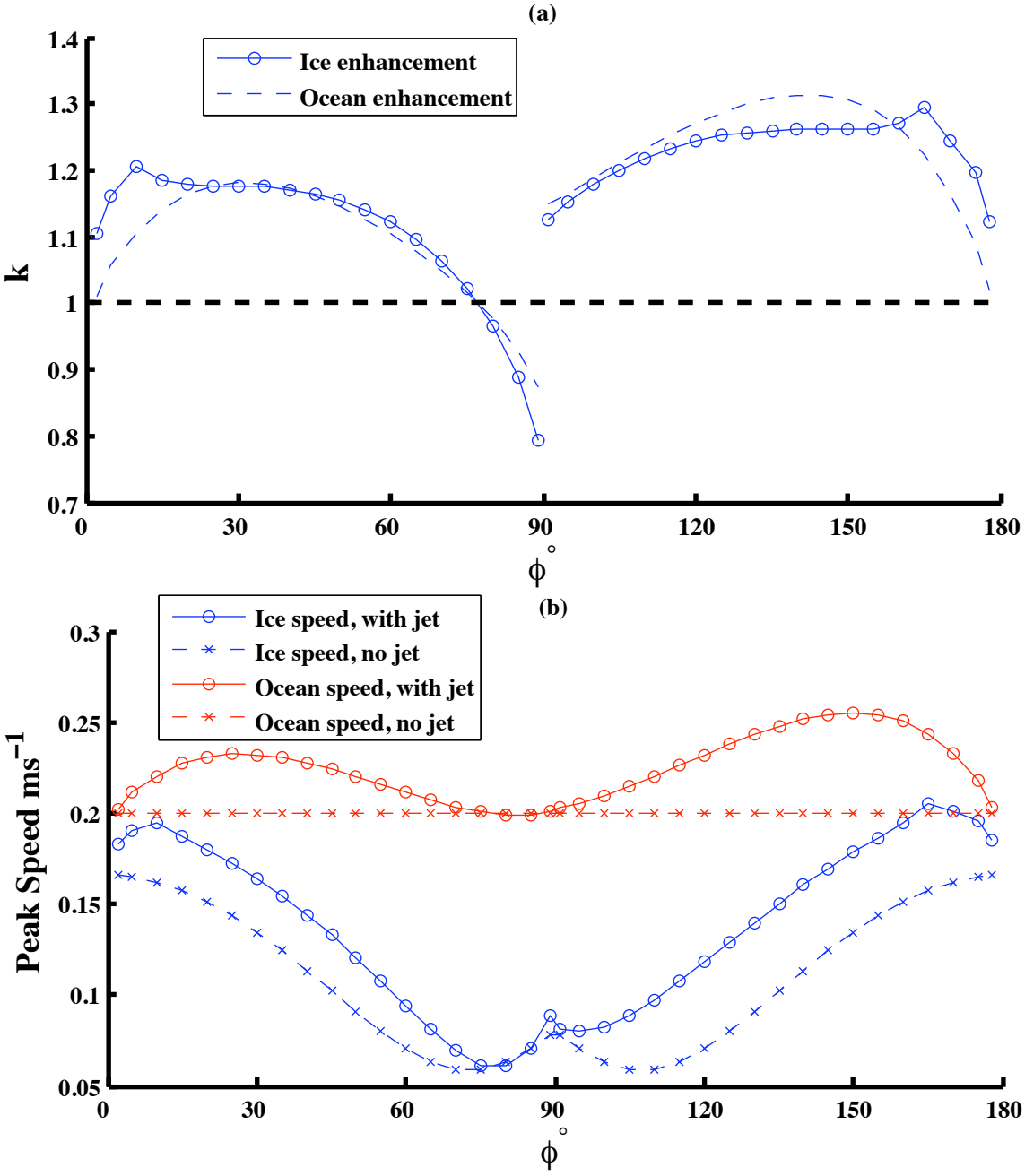


Figure 5.4: Ocean jet formation for varying $\phi$ in the northern hemisphere. The far field current speed is held constant at $U_O = 0.2$ m s$^{-1}$. Plot (a) is the enhancement of the parallel component of ocean and ice velocities, plot (b) the ice and ocean speeds, both taken at 500 m from the sea ice edge.

enhancement for both northern and southern hemisphere jets with a small difference ($<$20% of the sea ice enhancement) in magnitude (see figure 5.1(e)). The jets are smaller and less intense than the atmospheric jet. This is due to the jet strength depending on the difference between ice and ocean (or wind) speeds ($u^2_{\text{diff}}$), which is much smaller for the ocean jet. As with the atmospheric jet, the oceanic jet formation alters the direction of the ocean current and the sea ice drift (see figure 5.3(f)). Again the ice drift direction is closer to parallel than the ocean current beneath it due to the compaction of the sea ice edge. The directions of ice drift for the far field ($x > 3\mathcal{L}_{RO}$) are not equal for the three cases shown. This is due to the variation of the ice drift normal to the ice edge. The normal component of the sea ice velocity is constant throughout the solution and matched to the free drift at the edge of the sea ice pack (see section 4.3.3).

The ocean jet formation increases the ice transport parallel to the ice edge. This transport can be calculated as with the atmospheric jet case using equation (5.2.1), integrating over the distance 0 km $\leq x \leq 3\mathcal{L}_{RO}$ km. As the ocean jet covers a smaller distance into the sea ice pack, the ice transport associated with it is less. The no jet case has a transport of $\approx 7$ km$^2$ hr$^{-1}$ for the outer $3\mathcal{L}_{RO}$ of the ice pack. This increases by $\approx 1.3$ km$^2$ hr$^{-1}$ for the southern hemisphere jet and $\approx 0.6$ km$^2$ hr$^{-1}$ for the northern hemisphere jet. The ice concentration has a 19th profile as for the atmospheric jet (figure 5.3(a)) with a 70% concentration within 1 km from the sea ice edge.

The relationship between the changing angle $\phi$ and the ocean jet formation is different to that shown by the atmospheric jet in figure 5.2(a). The difference between ocean and ice velocity ($u^2_{\text{diff}}$) is smallest for ocean currents flowing in a direction parallel to the sea ice edge (see figure 5.4(b)) and greatest for normal flows where the compaction of the ice edge limits the normal component of the sea ice velocity. This damps the large jet speeds expected near to parallel angles and gives the bell curves in figure 5.4(a). As with the atmospheric jet, the lateral component of the ocean and ice velocities have a similar enhancement over all $\phi$ except for currents flowing parallel to the sea ice edge. At these angles, the normal ice drift velocity ($u$) is close to zero and the normal ice stress is balanced by the Coriolis effect. There is the same discontinuity as seen with the atmospheric jet about $\phi = 90^\circ$ due to the second order jet perturbation. This also gives rise to the increased jet for $\phi > 90^\circ$ and the negative jet for $80^\circ < \phi < 90^\circ$.

Changing the far field ocean current speed (figure 5.5(a)) alters the jet with a similar relationship to that seen with the atmospheric jet (figure 5.2(b)). The northern and southern hemisphere solutions are split by the

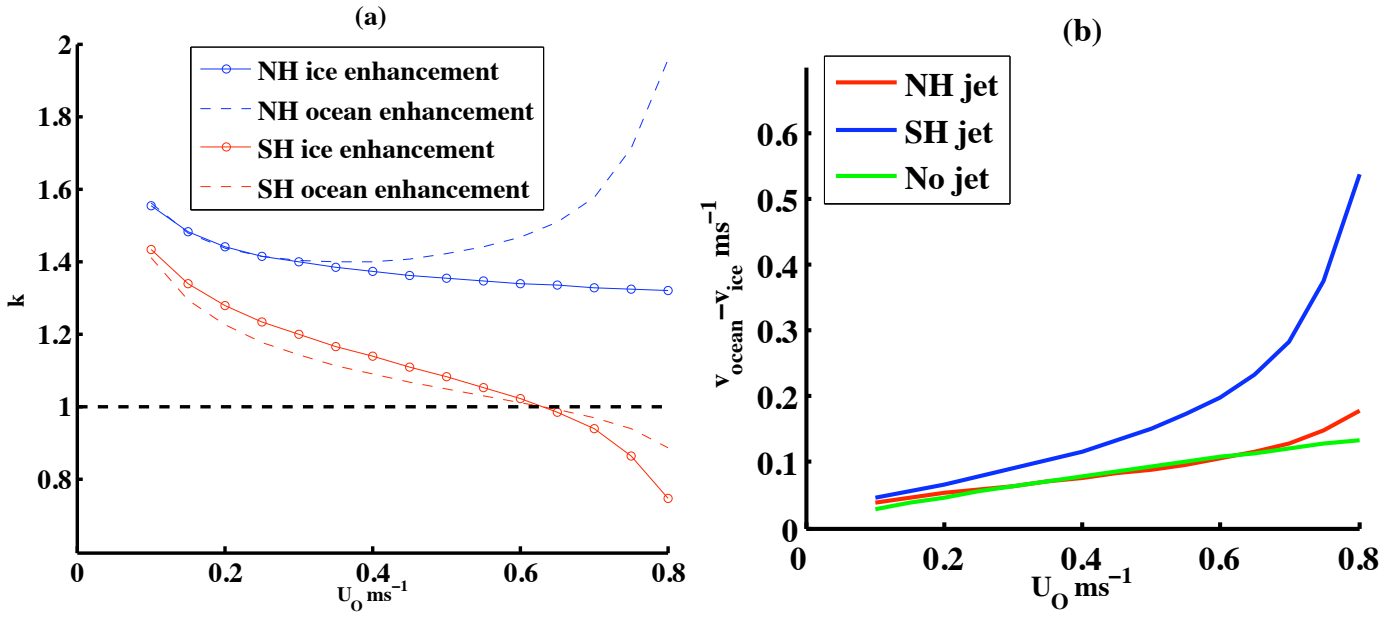


Figure 5.5: Ocean jet formation for varying $U_O$, the far field ocean current speed with the approach angle held constant at $\phi = 30°$. In plot (a) is for the enhancement factor $k$ of the parallel velocities of a jet in the northern (NH) and southern (SH) hemisphere. Plot (b) is the difference between the lateral component of the ice and ocean velocities.

asymmetrical component of the ocean jet. This asymmetry is greater for higher ocean speeds with negative jet perturbations for the northern hemisphere as the critical limit is approached ($\mathcal{F}_O \to 1, U_O \to 0.8$ m s$^{-1}$). The relationship is not as linear as that of the atmospheric jet. This is due to the increased complexity created by the $u^2_{\text{diff}}$ term. Increasing the far field current speed decreases the ice jet enhancement (solid lines), whereas the ocean jet shows an increase for the southern hemisphere jet (dashed blue line). For the case of no jet and the northern hemisphere jet, the difference between the lateral ocean and ice velocities have a similar relationship with the far field ocean current $U_O$ (figure 5.5(b)). For the southern hemisphere and the positive second order jet the difference is much greater for higher $U_O$ (solid blue line). This gives the increase in ocean jet enhancement seen in figure 5.5(a).

The ocean jet described in figures 3.6(c) and (d) in chapter 3 is not consistent with the jet calculated from this model, seen in the ocean enhancement in figure 5.4(a). This is due to the assumption used for calculating $u^2_{\text{diff}}$ in section 3.2.4. This assumption was that the lateral component of the ice velocity is held at $3/4$ the magnitude of the ocean velocity. This can be replaced with the factor $U^{\text{ocean}}_{\text{ice}}$, where previously

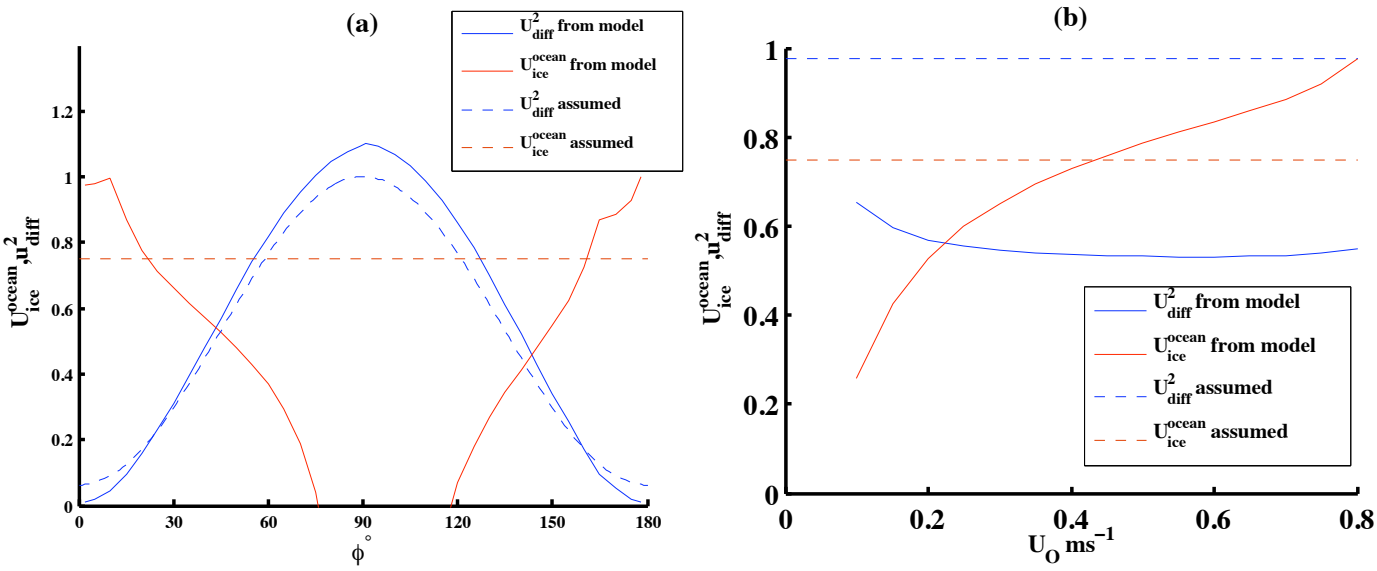


Figure 5.6: The relationship between sea ice and ocean jet formation. The blue lines are calculated values of $u^2_{\text{diff}}$, the red lines are calculated values of $U^{\text{ocean}}_{\text{ice}}$, the dashed lines are values from chapter 3. Plot (a) is for varying values of $\phi$ as in figure 5.4. Plot (b) is for varying values of $U_O$, with $\phi = 30°$, as in figure 5.5.

a value of $U^{\text{ocean}}_{\text{ice}} = 3/4$ was used. Figure 5.6 shows the relationship of $u^2_{\text{diff}}$ and $U^{\text{ocean}}_{\text{ice}}$ against changing $\phi$ (5.6(a)) and $U_O$ (5.6(b)), compared to the assumptions of chapter 3. This improved form of $U^{\text{ocean}}_{\text{ice}}$ can be used to apply the ocean jets to a large sea ice model, as in chapter 6.

### 5.2.3 Combined Jets

The atmospheric and oceanic jets are likely to form whenever there is neither a still ocean or atmosphere (as observed by King et al. 2010). For these cases the oceanic jet needs careful consideration, as depending on the direction of the applied stresses, the ocean jet can either form positive or negative relative to the ocean current. If the sea ice is moving faster than the ocean in the along ice direction, then from the frame of reference of the sea ice edge, the ocean current will appear to be approaching the sea ice edge from the opposite direction, giving a negative jet. The atmosphere (typically 1-10 m s$^{-1}$, Andreas et al. 1984) moves two orders of magnitude faster than the sea ice (typically 1-10 cm s$^{-1}$, Johannessen et al. 1983) so does not need to be considered in this way. In the following experiments three scenarios have been investigated: the winds and ocean currents aligned; the winds and ocean currents seperated by an angle of $90°$ and opposing each other; and the winds and ocean currents separated by an angle of $45°$ and approaching the ice edge

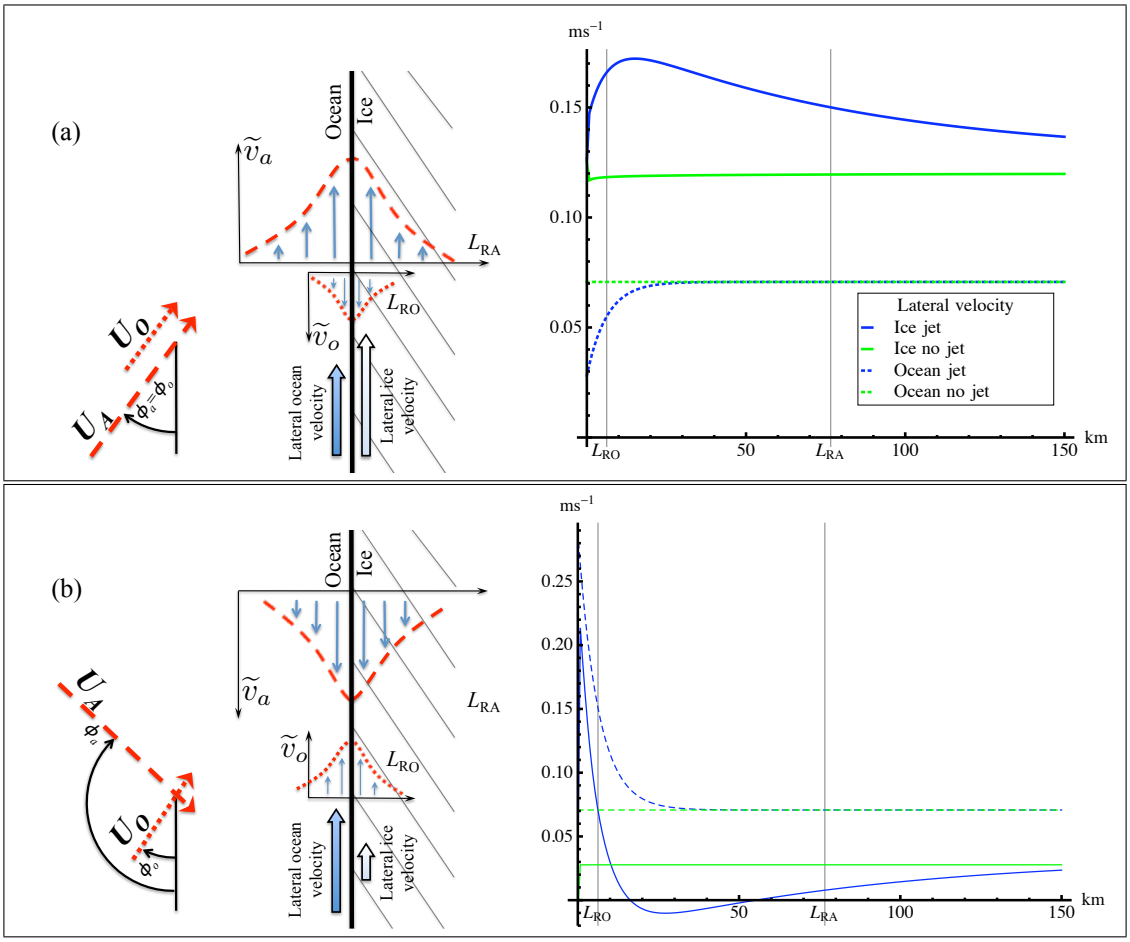


Figure 5.7: Combined jet formation for aligned (a) and opposing wind and ocean current (b). The diagrams show the direction of the approach winds and currents, along with the jet perturbations and relative velocities of the ice and ocean. The plots show the lateral component of the ice and ocean velocities for calculations with and without a jet.

from the same side.

To solve these various arrangements of atmospheric and oceanic stress, the experiments were first done for ocean and atmosphere with no jet. The direction of the ice movement in these experiments shows the relative direction between the ocean and the ice. This indicates the direction of a ocean jet. Far field wind and ocean current speeds of $U_A = 5$ m s$^{-1}$ and $U_O = 0.1$ m s$^{-1}$ have been used for all the experiments. These values give atmospheric and oceanic stress of comparable magnitude. Only the angle of incidence of

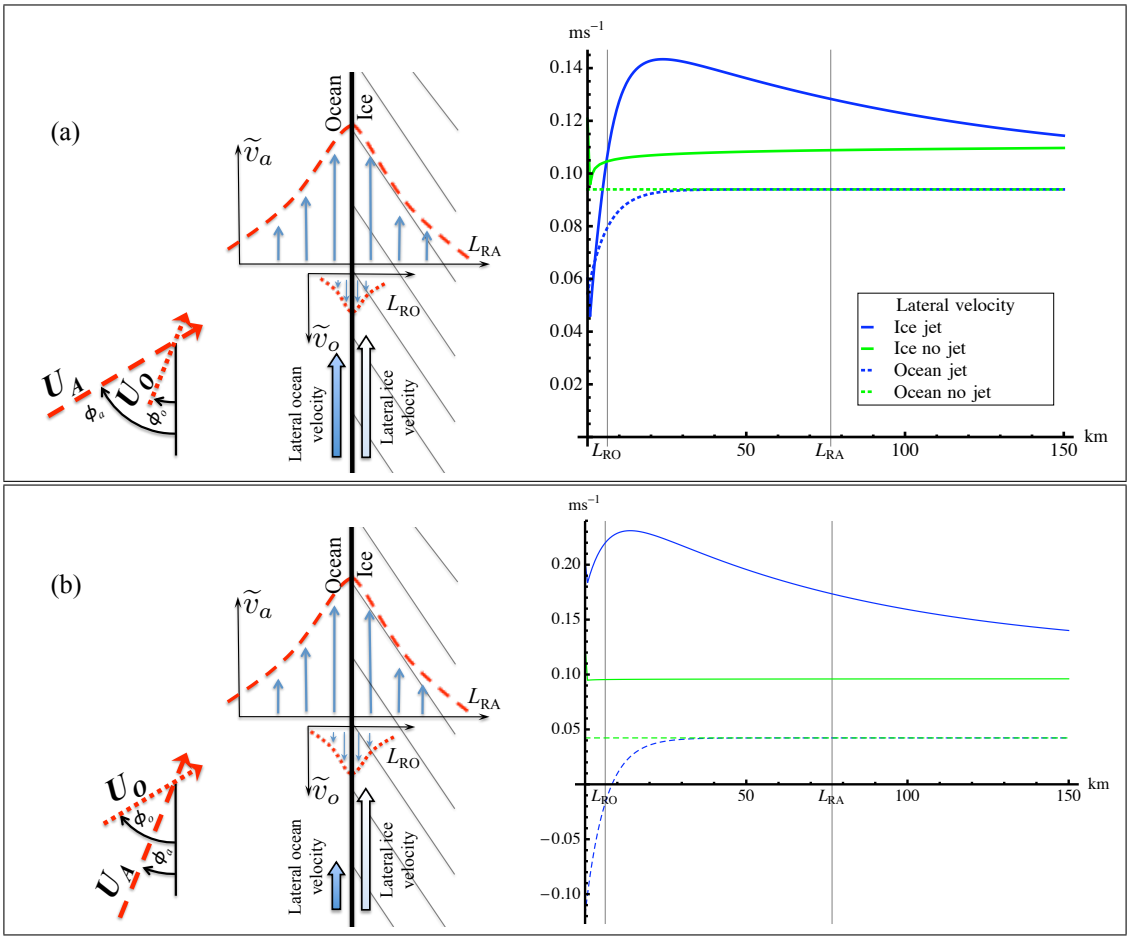


Figure 5.8: Combined jet formation for near aligned wind and ocean current. The diagrams show the direction of the approach winds and currents, along with the jet perturbations and relative velocities of the ice and ocean. The plots show the lateral component of the ice and ocean velocities for calculations with and without a jet.

the atmosphere ($\phi_a$) and ocean ($\phi_o$) with the ice edge have been varied.

### Aligned Winds and Ocean Currents

When the wind and ocean current are aligned, the ice is shown to be moving faster than the ocean (figure 5.7(a)). The ocean stress will counter the applied stress from the atmosphere (see figure 5.7(a)). This will cause a small oceanic jet negative to the direction of the ocean current. In this experiment $\phi_a = \phi_o = 45°$.

**Opposing Winds and Ocean Currents**

This situation produces the the largest ocean jet (see figure 5.7(b)). As the ocean and atmosphere oppose each other, the ice pack is held near stationary for the no jet solution. The stationary ice pack gives a large value for $u^2_{\text{diff}}$ and a strong ocean jet is formed positive to the far field ocean current. As the atmospheric jet is acting in the opposite direction to those in section 5.2.1, the sign$(v_x)$ term in equation (4.2.8b) is changed to represent the increasing rather than decreasing lateral ice velocity. In this experiment $\phi_o = 45^\circ$ and $\phi_a = 135^\circ$ separating the flows by $90^\circ$.

**Near - Aligned Winds and Ocean Currents**

These two experiments have the approach wind and ocean current separated by a $45^\circ$ angle, one at $\phi = 20^\circ$ and one at $\phi = 65^\circ$. Both these experiments (shown in figure 5.8) have the same jet structure as the aligned experiment: a positive atmospheric and a negative oceanic. The ocean jet is small for both solutions. The near parallel flow of the atmospheric jet for experiment shown in figure 5.8(b) gives a large value for $u^2_{\text{diff}}$ but the value of $\phi_o$ gives a small ocean jet. The opposite is true for the experiment shown in figure 5.8(a). The atmospheric stress leads to a small value for $u^2_{\text{diff}}$, damping the large jet given by the near parallel ocean current.

For all these cases the oceanic and atmospheric jets oppose each other. This is true for all times when the lateral component of the applied stresses are of comparable magnitude. If either of the applied stresses is lesser than the other, and is of comparable magnitude to the internal ice stresses, then the solutions in sections 5.2.1 or 5.2.2 will be valid.

A failing of these combined jet calculations is with the internal stress gradient. Equation (4.2.2b) contains a sign$(v_x)$ term. This is constant for the solutions with a single jet in sections 5.2.1 and 5.2.2 but not for the combined jets. As the ocean and atmospheric jet oppose each other (in a steady state), a change in sign$(v_x)$ is expected. This happens for all solutions in figures 5.7 and 5.8 at around 25 km from the ice edge. This model does not contain any method for changing sign$(v_x)$ so these solutions are somewhat inaccurate. The effect changing the sign$(v_x)$ has upon the solution is within the internal stress gradient. The component of

this in equation (4.2.3b) will work positively or negatively depending on the sign of $v_x$. For the outer region of the ice pack (where the ocean jet dominates) the internal ice stresses will act in the opposite direction to those in the inner. To balance this change in direction of stress, the ocean stress will have to increase. This increase comes from having a greater difference between the ice and ocean velocity. The ocean velocity is fixed so the lateral component of the ice velocity will be increased in the direction of the atmospheric stress. There will be step change in the solution. The impact of a change in the internal stresses are not expected to make a large impact upon the solution. For the experiments with an atmospheric jet the internal stresses are less than the applied stress see figures 5.1(c) and (d). The internal stresses for the experiments illustrated in figures 5.7 and 5.8 were of a similar magnitude.

The simplifications used in section 4.2.1 remove the ability of the ice pack to respond to discontinuities in the $x$, or on-ice, direction. This leads to the step changes due to the sign($v_x$) term. A more sophisticated model is needed to view the changing ice stresses. As the ice stress regime described in appendix A becomes complex without the simplifications in section 4.2.1, a complete dynamical sea ice model shall be used. This sea ice model is the Los Alamos Sea Ice Model (CICE) and the results are shown in chapter 6.

### 5.2.4 Ice Concentration Comparisons

The ice concentration profiles in all the model runs have a similar profile. This is the shape of 19th root of the distance from the ice edge, $x$ in this case, with some scaling (see the ice concentration solution in equation (4.2.5)). The rates of increase in ice concentration from all the model runs, with jets and without, are compared by plotting the distance from the ice edge (at $x = 0$) to the point where 90% ice concentration is achieved in figure 5.9. The plots for 80% and 95% concentrations have a similar form on a different distance scale. This is due to the concentration development following the same 19th root profile.

The rate of increase in ice concentration varies over all the experiments. There are trends within all sets of experiments where a single parameter is varied, though there is no single parameter that directly influences the ice concentration. To compare all the experiments, the ice motion at the edge has been compared to the ice concentration in figure 5.9.

The relationship in figure 5.9(a) shows that the faster the ice, the quicker the ice concentration increases, resulting in a shorter distance to the point of 90% ice concentration. This is as expected for the steady states

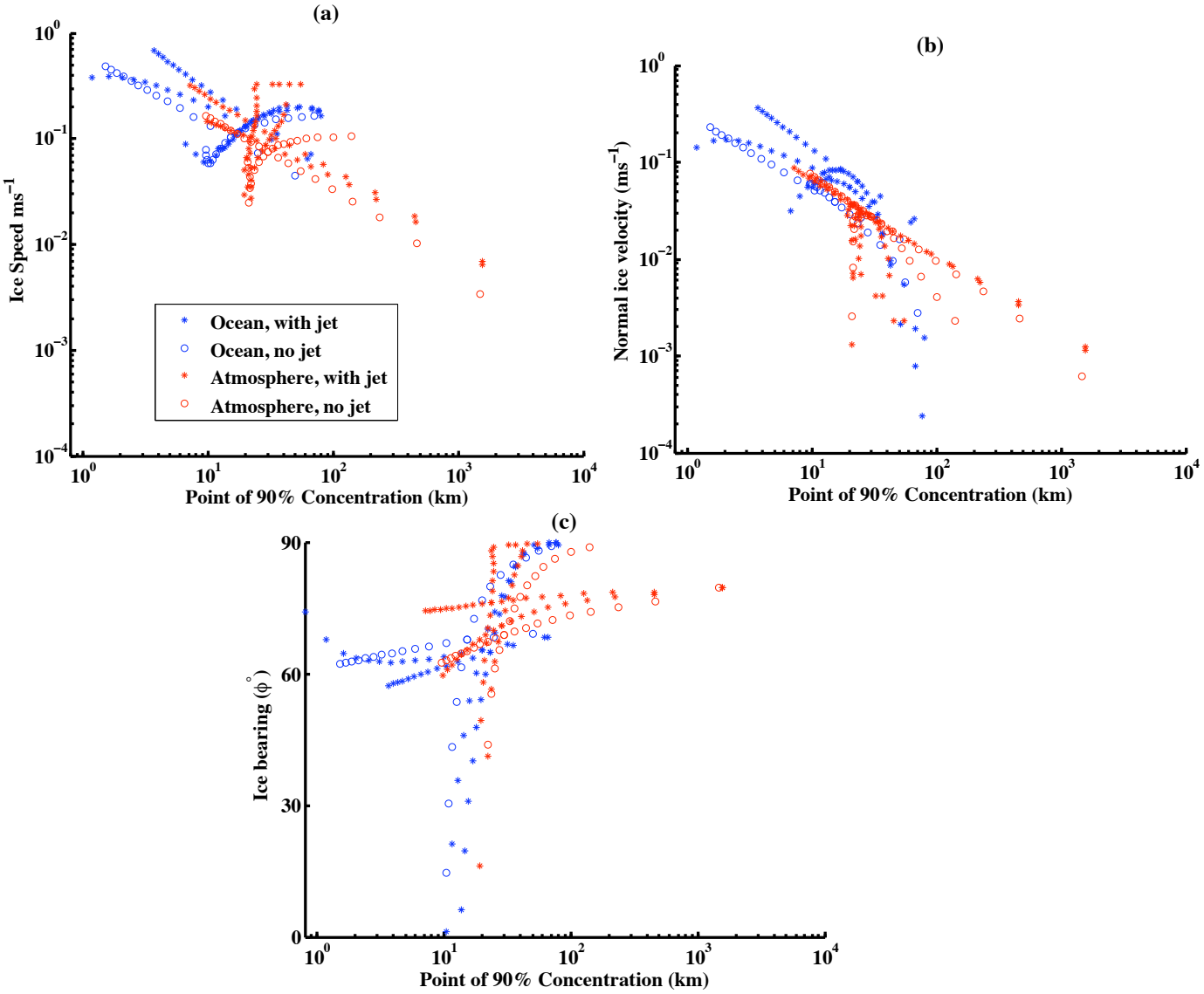


Figure 5.9: Relationship between ice concentration and ice edge velocity. The distance from the ice edge (on a log scale) at which 90% concentration is reached is plotted against; the ice speed (plot (a) - log scale), the normal component of the ice velocity (plot (b) - log scale) and the angle of incidence between the ice motion and the ice edge (plot c). This angle is analogous to $\phi\prime$ in figures 5.1(f) and 5.3(f). The red points are from experiments with a dominant atmosphere, blue for a dominant ocean. The circles represent experiments without a jet, stars with a jet.

considered in this model. For a higher ice velocity at the ice edge, the internal ice stresses will need to be higher to balance the applied stresses and Coriolis acceleration and to keep the ice edge steady. For this

model the ice stress depends upon the rate of change in ice concentration $\partial g(A)/\partial x$, with a higher value giving greater internal stresses and the sorter distance to 90% concentration. There is a similar trend when just considering the normal component of the ice edge velocity in figure 5.9(b). This component is more directly linked to the bunching of the sea ice, particularly in this model where it is held constant throughout the solution. High ice speeds and high normal components are not necessarily concurrent giving little trend between the direction of ice motion at the extreme ice edge and the increase in ice concentration. This can be seen in plot (c) where there is no clear trend.

There is no clear division in figure 5.9 between the ocean and wind jet experiments. The lowest ice speeds, and therefore slowest increase in ice concentration, occur for a still ocean which is only apparent in the atmospheric jet experiments. The variation in ice concentration shows that the dynamics of the ice edge is not just confined to the region within an order of Rossby radius of the extreme edge. The concentration can be less than 90% beyond the region under influence of the jets (300 km from the sea ice edge). Also the concentration can be greater the 95% very quickly, well inside the jets (under 10 km).

# CHAPTER 6

# RESULTS FROM THE CICE MODEL

This chapter documents the use of the Los Alamos Sea Ice model to investigate jet formation. The set up of the the model is documented in section 6.1. This includes the various grids used, the method of applying the jets to the sea ice edge and how the initial conditions are created. Of particular interest is section 6.1.3 which compares the model's response to jet formation at various resolutions. The results of the model are in section 6.2 with experiments with an atmospheric jet (section 6.2.1), oceanic jet (section 6.2.2) and both jets (section 6.2.3). Included in these sections are comparisons to the results from the Analytical model in chapter 5.

---

In the analytical model described in chapter 4 only the component of the ice velocity parallel to the ice edge was able to vary. The normal component was held constant (see section 4.2.1), restricting the direction in which the ice could deform. The edge was assumed to be laterally invariant, removing all variations along the ice edge. Only a steady state was considered. To model an unconstrained sea ice edge the Los Alamos Sea Ice Model (CICE) is used. This model is described in section 2.1.2 and uses a viscous plastic stress regime as described in appendix A. This is the same rheology used in the analytical model described in chapter 4. The ice edge in the CICE model is able to develop with time and in all directions. Also other processes such as ice ridging are considered.

## 6.1 Model Set Up

The CICE model is designed to model sea ice on a global scale. To focus on processes at the sea ice edge an idealised domain is used. The size of the domain is varied according to the grid spacing in order minimise computer run time. Several grids have been constructed to represent such a domain (see figure 6.1). These grids are land free and every grid point in each row (column) is at the same latitude (longitude). The east-west edges are cyclic, in that the ice exiting the domian on the western boundary enters upon the eastern boundary, and vice versa. The model had to be slightly modified in order to do this. This is the only modification made to the model in these experiments. The size of the domains have been selected to be greater than the length scale of the jets. The width of the domains are greater than $2\mathcal{L}_{R(A,O)}$ and the length is such that the rear end of the domain is far away from the area under the influence of a jet ($> 4\mathcal{L}_{R(A,O)}$ for the jets shown in chapter 3 at 70°N). For exact grid sizes see table 6.1. The jets are applied purely through the forcing data. As in chapter 5, the experiments are done in pairs, with and without a jet.

### 6.1.1 Jet Application

In order to develop the forcing data to include atmospheric and oceanic jets, individual data points have to be perturbed. The atmosphere and ocean velocity fields are stored in two arrays, the $x$ and $y$ components. To add jets to these fields, two values need to be known for each point in the array; the distance from the point to the ice edge, and the angle of the ice edge, which represent $\phi$ and $\widehat{n}$ in equations (3.1.16b) and (3.2.11b). These values can be calculated by analysing the ice concentration, and taking values from the grid dimensions.

To find the ice edge, two fields are created. These are areas of ice cover $A > 60\%$, and areas of open ocean $A < 15\%$. Points of ice edge are defined as points of ice cover that are within a certain distance of points of open ocean. This distance varies depending upon the grid resolution and how diffuse you want the edge to be. A longer distance will include points on a slowly increasing ice concentration. The search distances for the various domains are shown in Table 6.1. These distances were selected after performing an edge search on various time steps from the spin up runs.

From the ice edge points the ice edge angle can be calculated. A box of width $2\mathcal{L}_{R(A,O)}$ (for an atmo-

| Domain | Resolution | Width | Length | Edge Search Distance | Grid Points |
|---|---|---|---|---|---|
| Atmosphere | 50 km | 1000 km | 1500 km | 75 km | $20 \times 30$ |
| | 10 km | 400 km | 800 km | 20 km | $40 \times 80$ |
| | 5 km | 200 km | 800 km | 20 km | $40 \times 160$ |
| | 2 km | 200 km | 800 km | 5 km | $100 \times 400$ |
| | 1 km | 200 km | 800 km | 3 km | $200 \times 800$ |
| Ocean | 1 km | 200 km | 400 km | 3 km | $200 \times 400$ |
| | 500 m | 100 km | 200 km | 2 km | $200 \times 400$ |
| | 250 m | 50 km | 150 km | 1 km | $200 \times 600$ |

Table 6.1: Dimensions and key lengths of the domains shown in figure 6.1.

spheric or oceanic Rossby radius, respectively) is drawn around each point. Starting at the edge of each box, a search is performed for other edge points. When another point is found, the geodesic angle between this point and the original point is calculated. During this calculation a check is performed to keep the ice upon the right hand side, to keep all the ice edge angles consistent. This calculation is repeated for a number of times and averaged. If no other ice edge points are found within the box, the original edge point is discounted. For the grids shown in figure 6.1 the angle calculations were repeated five times. This number of calculations gave a consistent angle across the ice edge.

This process calculates the direction of the ice edge over a Rossby radius. Wobbles and deviations of a length scale shorter than this are ignored. Also ice edge points which are not part of a continuous edge are discounted.

A band of grid cells (one or two cells thick depending upon the straightness of the edge and the grid resolution) are now defined as the ice edge. As the jets cover a distance $\approx 3\mathcal{L}_{R(A,O)}$ away from the ice edge, a thicker band of cells is needed to define the region affected by the jets. Setting the distance $l$ from the ice edge in the thin band of edge cells as $l = 0$, the band of cells can be thickened by considering each ice edge cell and adding all unselected neighbouring cells. The distance from the ice edge is increased by considering the grid cell size at this point. The ice edge angle is also passed on to the new points. This process is iterated until a band of width $\approx 6\mathcal{L}_{R(A,O)}$ is created. This distance contains all significant perturbations to the wind or ocean current in both directions from the ice edge.

The jets can now be added to the wind velocity components of the forcing data. The values needed in equations (3.1.16b) and (3.2.11b) are $U_{(A,O)}$ taken from the original velocity arrays, $\widehat{n}$ calculated by scaling

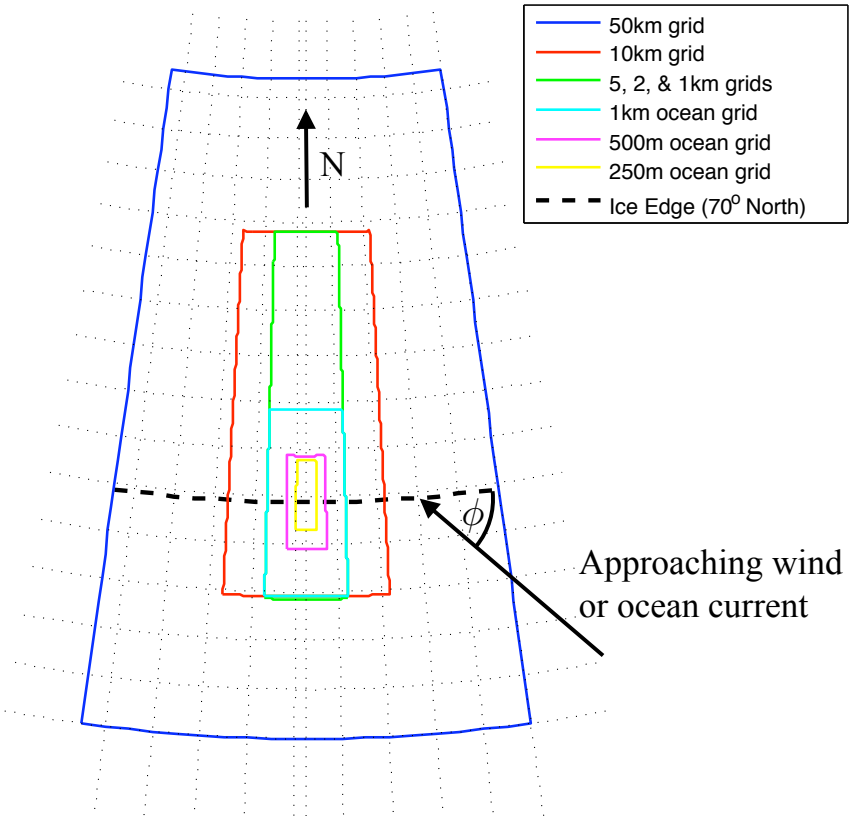


Figure 6.1: Domains used in the CICE experiments. The dashed grid lines are spaced by 100 km, with an extra line at 0°W. The grids are all centred upon (70°N,0°W), with an ice edge at $\approx$ 70°N. The angle between the wind or ocean current and the sea ice edge, $\phi$, is illustrated.

$d$ over a Rossby radius and $\phi$ the difference between the ice edge angle and geodesic angle of the wind or ocean current (see figure 3.2). This geodesic angle can be calculated from the components of the forcing data and the geodesic angle of the grid. The atmospheric jets can now be added. For the oceanic jets, the $u^2_{\text{diff}}$ term needs to be considered. The coupled method of calculating this term used in chapter 4 cannot be used. The addition of the jets is external to the dynamics of the CICE model, and there is no free drift layer at the edge of the ice. The relationship between $u^2_{\text{diff}}$ and $\phi$ or $U_O$ shown in figure 5.6 is considered. The $\phi$ dependency can be easily parameterised with $u^2_{\text{diff}}[\phi] = \mathcal{K} \sin^2 \phi$, where $\mathcal{K} = 1.1$ is a constant. The $U_O$ dependency is not conclusive from the analytical model so is not considered in calculating $u^2_{\text{diff}}$ for the CICE experiments.

### 6.1.2 Initial Conditions

To get a smooth, but yet realistic initial ice edge at 70° N a spin up period is needed. The initial ice state gives a constant ice thickness distribution (with an average ice thickness of $\approx 1.5$ m) and concentration (calculated from the thickness distribution and approximately 99%) over the ice covered portion of the domain. Running the model with a still ocean and atmosphere and an idealised forcing set gives a more realistic development from the open ocean to continuous ice cover. However a small change in the forcing can cause large areas of new ice to form. This gives the outer 10 km of the ice edge as thin ($<$ 20 cm) ice which is not consistent with a stable and well compacted ice edge. Spin up runs giving such edge conditions have to be repeated after adjusting the idealised forcing set, specifically the ocean surface and air temperatures. The length of the spin up period depends on the domain used as a higher resolution model has more grid points. Also due to way in which the CICE model remaps its fields, the higher resolution models require a shorter time step. Computational constraints on the high resolution (grid size of less than 5 km) models meant that the spin up phase of the model run can be for 10 to 20 model days. The low resolution models could be allowed to run for a longer period. This longer spin up gives more starting points to choose from, allowing for a more compacted ice edge during the jet experiments. The high resolution models have a less smooth ice edge. This is due to the shorter spin up period, and also the small scale variations that can exist at the higher resolutions but not at the low resolutions.

After performing all the spin up runs all the resolutions have similar ice states. The ice concentration increases rapidly, and the ice thickness increases to between 1 m and 1.5 m, within 10 km of the ice edge or within one grid cell for coarser 50 km resolution. The ice states for the various resolutions are not identical. Changing the resolution of the model changes the response of the model to the forcing. Altering the forcing to ensure the same ice response for all resolutions is the beyond the scope of this thesis and such consistency is not needed as all the jet experiments which are to be compared will be at the same resolution and with the same initial conditions.

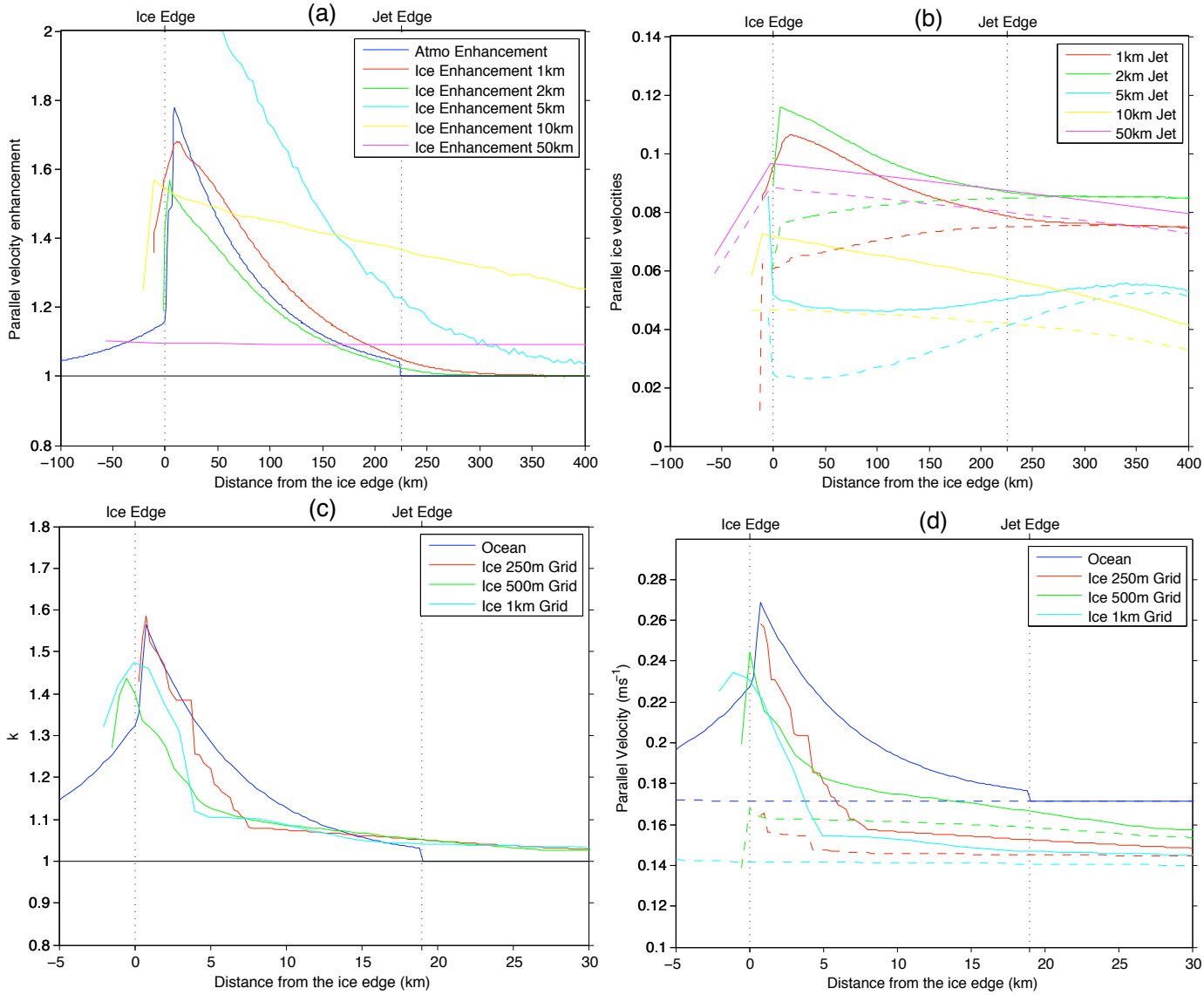


Figure 6.2: Resolution comparisons. Plots (a) and (b) are for the atmospheric jet experiments, plots (c) and (d) are for the ocean jet experiments. The zonally averaged enhancement of the parallel velocities are shown in plots (a) and (c). The jet (solid line) and no-jet (dashed line) zonally averaged parallel velocities are shown in plots (b) and (d). Plot (d) includes the ocean velocity (blue).

### 6.1.3 Resolution Comparisons

The response of the sea ice to the jets is not the same for all resolutions. The same jet experiment was repeated on each domain in order to find at which resolution the response of the sea ice converges to the same solution. Convergence is needed to ensure that the experiments in section 6.2 correctly analyse the

sea ice response to the jet formation, not to processes that can only occur at a particular resolution. For the atmosphere a wind of 5 $ms^{-1}$ at an angle of $\phi = 135°$ to the ice edge was used. The process in section 6.1.1 was used to add the jet to the forcing. The lowest resolution used was 50 km to represent the resolution commonly used by the sea ice component in global climate models. It is also the resolution of a working Arctic wide CICE set up at our disposal. Higher resolution domains at 10 km, 5 km, 2 km and 1 km were also used. These domains can be seen in figure 6.1 along with the domains used for the ocean jet experiments. The ocean jet was tested at 1 km, 500 m and 250 m resolution.

Figure 6.2 shows the results for the atmospheric jet approaching convergence for the 2 km and 1 km resolutions. The way in which these results are interpreted and presented is explained in section 6.2. The enhancement for the parallel ice velocity in both of these experiments is similar to the enhancement of the wind speed in lateral extent (plot (a)) The magnitude of the enhancement differs by less than 20% of the atmospheric enhancement, a similar result to the analytical model in figure 5.1. This result is in agreement with the results in chapter 5. The parallel component of the sea ice velocity from the jet and no-jet runs using the 1 km and 2 km resolutions (plot (b)), although not identical in magnitude due to the differing ice state between model set ups (as discussed in section 6.1.2), have a similar profile which is not matched by the lower resolution runs. From this, it is concluded that to accurately test the effects of the atmospheric jet upon the sea ice edge, a grid size of at most 2 km must be used. In section 6.2.1 the 1 km resolution is used.

The sea ice shows little response to the jets at 50 km resolution, and simulation of the jets on a global model of this size would be inconclusive. The response of the model at 10 km and 5 km resolution is not consistent. For the test runs illustrated in figures 6.2(a and b) there is a very large jet enhancement for the 5 km resolution (blue lines) due to large variations in the ice velocity. This response was not matched by any of the other resolutions and was also not seen for different wind patterns at the same 5 km resolution. Analysis of atmospheric jet formation over the sea ice at 5 km resolution would not be conclusive.

There is no clear convergence for the ocean jet in figure 6.2 (c) and (d). There is an ice jet in all three of the runs which has a similar size and shape. The magnitude of the ice drift speed in both the jet and no-jet runs are similar (plot(d)). As the resolution increases the ice jet approaches the shape of the ocean jet, though it does not have the the same correlation as seen with the atmospheric jet on the 1 km grid. When at the high resolutions used for the ocean jet, the ice thickness can alter greatly over the width of the jet,

whereas it is near constant over the width of the atmospheric jet. This gives the unsmooth velocity profile and disagreement between the runs within 5 km from the sea ice edge for the ocean experiments at 500 m and 250 m resolution. A grid resolution of 500 m has been selected for the experiments in section 6.2.2, to give a well defined jet whilst keeping a run time short enough to allow the various runs shown in section 6.2.2.

## 6.2 Results

Taking the initial conditions described in section 6.1.2, experiments were performed. For the atmospheric jets a domain with a 1 km resolution is used, for the oceanic jets a 500 m resolution. Various jets are applied using the method described in section 6.1.1. The idealised forcing sets are applied to the ice for 6 hours to allow a semi-steady state in which short time scale accelerations to the sea ice have finished. The CICE model outputs results at every hour giving values for every grid point. As the grids are square in latitude and longitude and the ice edge is at constant latitude, the output data can be averaged across the grid width (in the direction parallel to the ice edge) to give a mean value in the zonal direction normal to the ice edge. This mean value is the one used in figures 6.2 through to 6.8. Standard deviations to the mean values are typically $< 2\%$ of the mean values and are too small to plot. Representing the data in this way allows direct comparisons to the results in chapter 5 to be made.

Demonstration calculations with the same forcing conditions as used for the analytical model are shown. The angular and far field velocity dependencies have been tested using many individual model runs. Due to the time constraints in performing many high resolution model runs, the dependencies are tested over fewer individual points than used for the analytical model. As the ice motion in the CICE model is unconstrained the far field forcing can have a value of $0^\circ \leq \phi \leq 180^\circ$.

For experiments with the atmospheric jet the ocean is kept still, and vice versa (section 6.2.1 and 6.2.2). Experiments with both atmospheric and oceanic jets are shown in section 6.2.3.

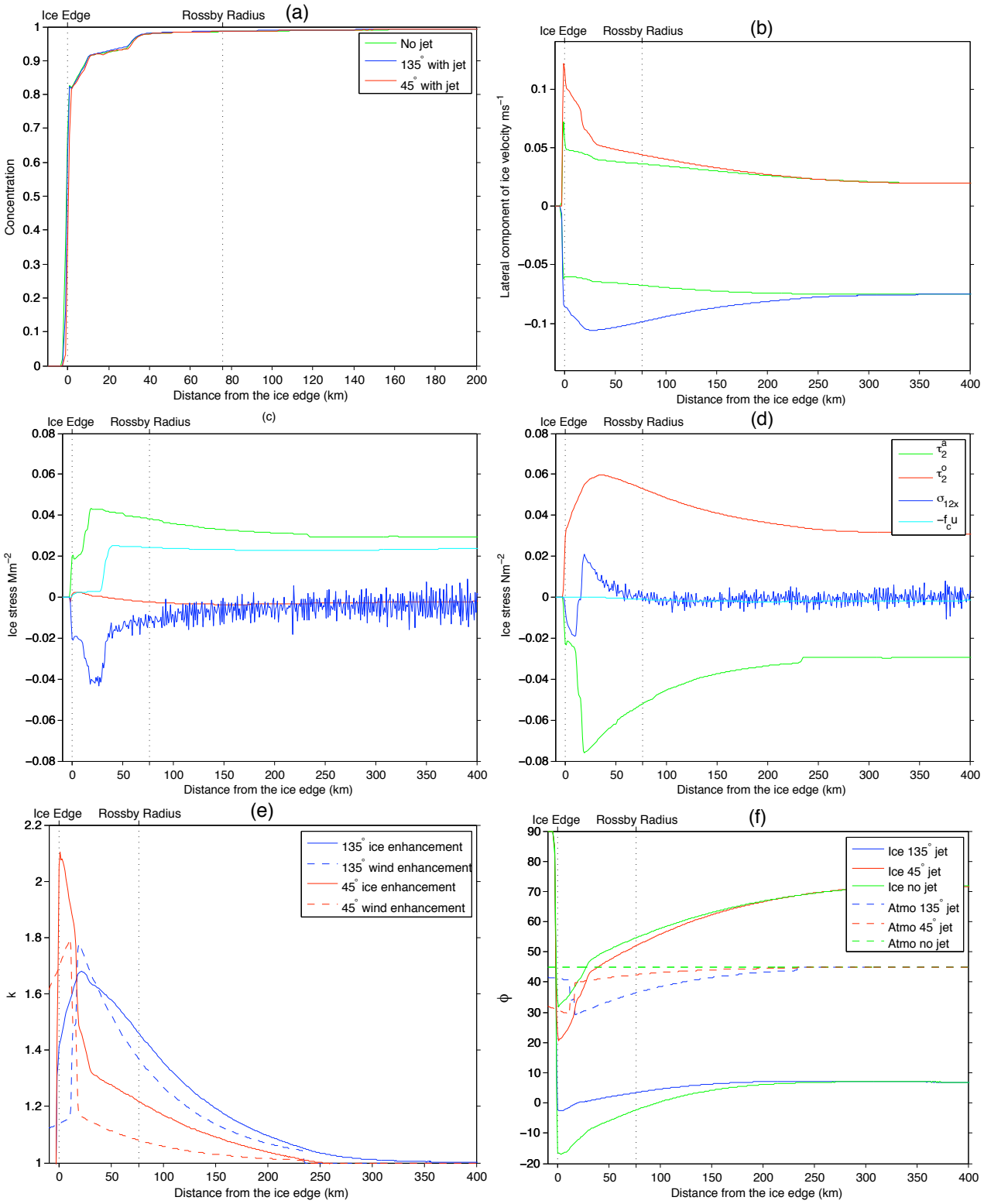


Figure 6.3: Atmospheric jet experiment analogous to figure 5.1. Plot (a) is the ice concentration $A$ as with figure 5.1(a) and plot (b) is the dimensional lateral ice velocity $v$; see legend for the cases plotted. Plots (c) and (d) are the dimensional stress components for the $\phi = 135°$ experiment, plot (c) normal, plot (d) parallel to the ice edge. Plot (e) is the enhancement factor $k$ of the velocity components parallel to the ice edge. Plot (f) is the angle $\phi\prime$ between the wind (dashed) and ice (solid) motion and the ice edge. The $135°$ cases are plotted as $180° - \phi\prime$ to ease comparison.

### 6.2.1 Atmospheric Jet

An ice jet forms in the model in under an hour and is present in the first time step of the model and remains constant over the run. Parallel to the ice edge (figure 6.3(d)) the external stresses dominate with the atmospheric stresses balanced by ocean drag which oppose the ice motion due to the ocean being still. Normal to the ice edge (figure 6.3(c)) the atmospheric stress is balanced by the internal ice stresses and the Coriolis effect. The demonstration stress profiles are for $\phi = 135^\circ$ where the Coriolis component opposes the on-ice atmospheric stress. The Coriolis component has a large step at $\approx 40$ km from the ice edge due to an increase in ice thickness at this point. The sharp change in the Coriolis component is balanced by the internal stress of the sea ice, resulting in no change in the sea ice velocity at this point. The Coriolis component has a large effect on the normal component of the sea ice drift, with differing values for the demonstration calculations. For the wind at $\phi = 135^\circ$ to the ice edge, the Coriolis component restricts the normal component resulting in the angle between the ice drift and the ice edge being small (blue solid line and neighbouring green solid line in figure 6.3(f)). For the extreme edge the ice is dispersing. For the wind at $\phi = 45^\circ$ to the ice edge the Coriolis component compacts the ice edge giving a higher normal ice drift. The angle between the wind and the ice drift is $\approx 30 - 40^\circ$ in the direction of the Coriolis acceleration for all cases.

The difference between the positive and negative second order solution to the jet is clearly seen between the jets at $\phi = 135^\circ$ and $\phi = 45^\circ$ (blue and red lines respectively in figures 6.3(b) and (e)). These two solutions are congruous to a jet at $\phi = 45^\circ$ in the southern and northern hemispheres respectively. The change in sign of the second order component is at the extreme ice edge and alters the ice velocity. The alteration is most evident for the wind at $\phi = 45^\circ$ to the ice edge (red lines in figures 6.3(b) and (e)) where the ice velocity rapidly increases at the ice edge forming a $\approx 20$ km wide jet. This rapid increase in ice velocity will be referred to as the thin atmospheric ice jet for the remainder of the thesis. The velocity profiles of the no-jet cases have a slight westward bend toward the ice edge (green lines in figure 6.3(b)) that can be accounted for by the increasing ice thickness and therefore Coriolis component further into the ice pack. The enhancement factor k (as described in section 5.2.1) of the parallel component of the ice velocity correlates well to that of the wind velocity (see figure 6.3(e)). The correlation is greater for the wind at $\phi = 135^\circ$ than for $\phi = 45^\circ$.

The ice transport parallel to the edge can be calculated as in chapter 5. The definite integrals can be calculated numerically using the across grid averaged velocities and concentrations along with the grid cell size at each data point. As the ice thickness in the CICE model is not constant, the volume transport is first calculated and then divided by the cross sectional area of the ice to get the ice area transport

$$\mathcal{A}_{\text{transport}} = \frac{\int_0^{3\mathcal{L}_{RA}} Avhdx}{\int_0^{3\mathcal{L}_{RA}} hdx}. \tag{6.2.1}$$

Where $A$ is the ice concentration, $v$ is the component of the dimensional ice drift velocity parallel to the sea ice edge and $h$ is the ice thickness. As with the analytical model the sea ice transport is calculated over the outer $3\mathcal{L}_{RA}$ of the sea ice pack. For the cases of no-jet the ice transport parallel to the ice edge is $\approx 55$ km$^2$ hr$^{-1}$ for the wind at $135^\circ$ to the ice edge and $\approx 28$ km$^2$ hr$^{-1}$ for the wind at $45^\circ$ to the ice edge. The transport increases when an atmospheric jet forms, by $\approx 18$ km$^2$ hr$^{-1}$ for the wind at $135^\circ$ and by $\approx 6$ km$^2$ hr$^{-1}$ for the wind at $45^\circ$.

The ice concentration increases rapidly for all runs (figure 6.3(a)), reaching 99% inside 40 km from the ice edge. As the runs all have the same initial conditions and are over too short a time scale for large scale ice drift ($> 10$ km), no discernible difference between the runs can be observed.

The angular dependence of the atmospheric jet intensity is matched by the ice jet (figure 6.4(a)). At near parallel winds where there is a large jet intensity, the sea ice jet reaches a maximum enhancement of $k \approx 2.5$. The enhancement of the thin atmospheric ice jet (as described above and seen in the red line in figure 6.3(b)) due to the second order discontinuity (solid red line) is higher than the enhancement of the atmospheric jet (dashed red line). There is a similar plateau as experienced by the ice outside the thin jet.

Changing the far field wind speed changes the enhancement of the atmospheric jet (red and blue dashed lines in figure 6.4(b)). This change in enhancement does not transfer directly to the sea ice. For faster wind speeds ($U_A > 5$ m s$^{-1}$) the sea ice velocity enhancement is similar to the atmospheric enhancement. The negative side of the second order jet (for $\phi = 45^\circ$ in this case) along with the thin edge jet follow the atmospheric enhancement above them (the atmospheric enhancement above the thin jet is the same as the positive side of the jet - the dashed blue line). The sea ice velocity enhancement for the positive second

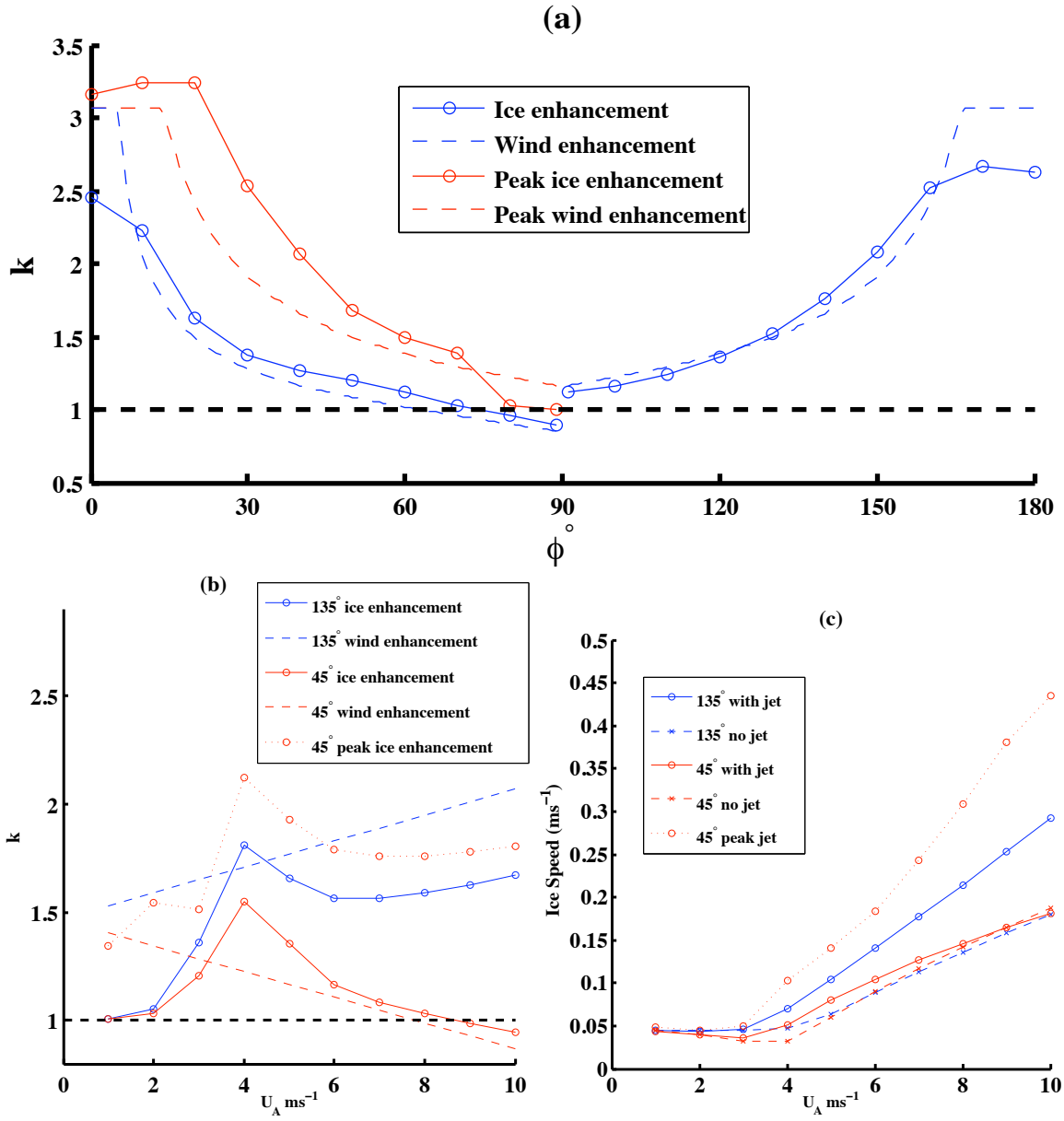


Figure 6.4: Atmospheric jet formation for varying wind direction and speed, values taken at 20 km from the ice edge to avoid the thin atmospheric jet. The red 'peak' lines correspond to the thin atmospheric jet taken at 5km from the ice edge. Plot (a) is the enhancement of velocities parallel to the ice edge for varying $\phi$. Plot (b) is the ice enhancement for varying wind speed $U_A$. Plot (c) is the dimensional ice speed for varying wind speed.

order jet ($\phi = 45°$) is less than for the atmosphere with the same trend. For $U_A < 5$ m s$^{-1}$ the correlation breaks down. The ice speed is near constant for all runs with $U_A < 3$ m s$^{-1}$ and even decreases slightly for increasing $U_A$ for the no-jet runs. This non-linear relationship between the wind and ice speed results in the non-linear change in enhancement. At low wind speeds the applied atmospheric stress is low and less important in the momentum balance.

**Analytical Model Comparisons**

The size and shape of the ice jets are similar to those calculated by the analytical model in section 5.2.1. The is a strong similarity between figures 5.1 and 6.3 except for the thin atmospheric jet for winds at $\phi = 45°$ to the ice edge in the CICE model and different magnitudes of stresses in the stress balance. The different stress magnitudes are due to different drag coefficients in the two models. The atmospheric ($C_a = 3.5 \times 10^{-3}$) and oceanic ($C_O = 0.011$) drags used in the analytical model were derived from observations of the marginal ice zone (see sections 3.1.4 and 3.2.4). These values are approximately twice those used in the CICE model which represent the smooth central pack ice. When repeating the analytical model calculations using the drag coefficients used in the CICE model, the values in the stress balance are of similar magnitude to those in figure 6.3(c) and (d). The ice drift speeds for the different models vary by less than 10% despite the different drag coefficients.

The angular dependence of the jet enhancement is the same for both models (blue lines in figures 5.2(a) and 6.4(a)). The atmospheric jet in both models are calculated using the same equation. The ice drift enhancement has strong correlation to the atmospheric enhancement in both models, with a slightly reduced enhancement for parallel winds in the CICE model. For low wind speeds there is less of a correlation between the wind and ice enhancement in the CICE model than seen at high wind speeds (see figure 6.4(b and c)). There is a strong correlation for all wind speeds in the analytical model.

### 6.2.2 Oceanic Jet

The formation of an ocean jet under the sea ice forms a sea ice jet above it. The ice jet takes 4-6 hours to form during which the sea ice is accelerating to the velocity of the ocean beneath it. As the stress applied to ice from the ocean is proportional to the square of the difference in velocity between them, the ice acceleration

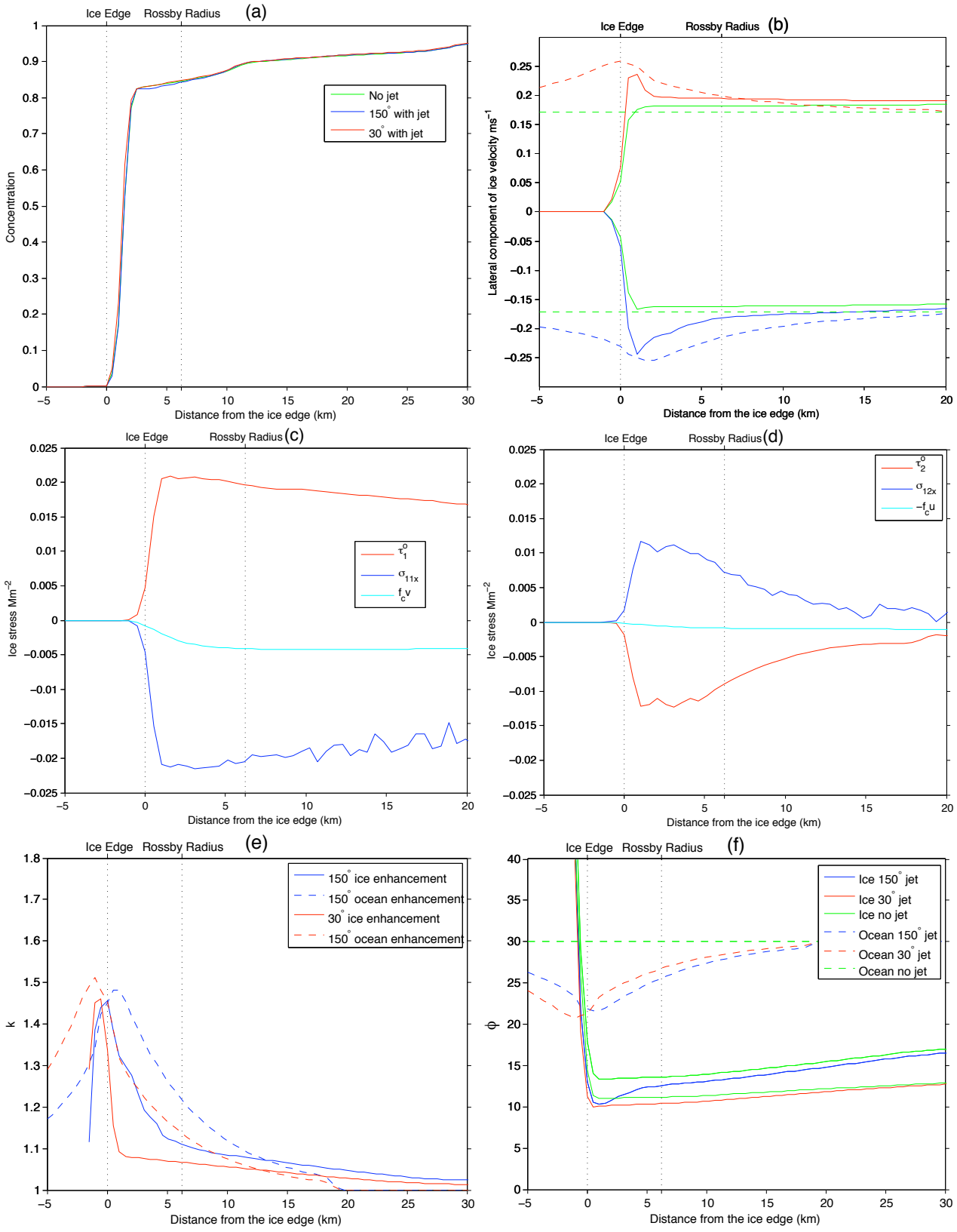


Figure 6.5: Ocean jet experiment analogous to figure 5.3. Plot (a) is the ice concentration $A$ and plot (b) is the dimensional lateral ice and ocean velocities $v$; see legend for the cases plotted. Plots (c) and (d) are the dimensional stress components for the $\phi = 150°$ experiment, plot (c) normal, plot (d) parallel to the ice edge. Plot (e) is the enhancement factor $k$ of the velocity components parallel to the ice edge. Plot (f) is the angle $\phi\prime$ between the wind (dashed) and ice (solid) motion and the ice edge. The $150°$ cases are plotted as $180° - \phi\prime$ to ease comparison.

is greatest at the first time step. The results shown in figures 6.5, 6.6 and 6.7 are from the semi-steady state reached by the end of the demonstration model runs.

Both normal (figure 6.5(c)) and parallel (figure 6.5(d)) to the sea ice edge the ocean stress is balanced by the internal ice stress. The Coriolis component is small and is normal to the ice edge in the off-ice direction. The parallel component of the sea ice velocity is close to that of the ocean. For both the $\phi = 30^\circ$ and $\phi = 150^\circ$ no-jet experiments the parallel component of the sea ice velocities (solid green lines) are westward of that of the ocean velocity, resulting in the parallel component of sea ice velocity being greater than that of the ocean for $\phi = 30^\circ$. The ice speed, however, is still less than that of the ocean. The westward difference between the sea ice and ocean is due to the difference between the direction of ocean current and ice drift (figure 6.5(f)) which is greater for the currents at $\phi = 30^\circ$. For $\phi = 30^\circ$ the ocean drag normal to the ice edge opposes the the Coriolis acceleration whereas for $\phi = 150^\circ$ they are aligned.

The enhancement of the ocean and ice velocity have a similar magnitude (see figure 6.5(e)). The shape of the enhancement is not as correlated as the atmospheric jet in figure 6.3(e). There is a similar thin jet at the extreme ice edge as seen with the atmospheric jet in section 6.2.1. This forms for the negative second order jet solution during angles of incidence $0^\circ < \phi < 90^\circ$.

There is an increased ice drift parallel to the ice edge. For a current at $\phi = 150^\circ$ to the ice edge there is a drift of $\approx 11$ km$^2$ hr$^{-1}$ for the outer $3\mathcal{L}_{RO}$ of the ice pack which increases by $\approx 1.8$ km$^2$ hr$^{-1}$ when the ocean jet is present. For a current at $\phi = 30^\circ$ to the ice edge there is a drift of $\approx 10$ km$^2$ hr$^{-1}$, increasing by $\approx 1.2$ km$^2$ hr$^{-1}$ with the ocean jet.

The ice speed is very similar to the ocean speed over all angles of incidence (see figure 6.6(b)). The velocity enhancement of the sea ice parallel to the ice edge is similar to that of the ocean for near normal angles of incidence ($50^\circ < \phi < 130^\circ$), but is less for near parallel angles. There is a similar peak enhancement for the thin oceanic jet for $0^\circ < \phi < 90^\circ$. The enhancement for this peak jet is greater and has a slight correlation to the ocean enhancement at this point (red lines in figure 6.6(a)). For varying far field ocean current speed, the ocean and sea ice velocity enhancement are well correlated (figure 6.7(a)) for the positive and negative sides of the second order jet ($\phi = 150^\circ$ and $\phi = 30^\circ$ respectively) and also the thin oceanic jet for $\phi = 30^\circ$ (red dotted line). This correlation is due to the difference between the parallel component of the ocean and sea ice velocity being small (figure 6.7(b)). This difference decreases for higher ocean speeds.

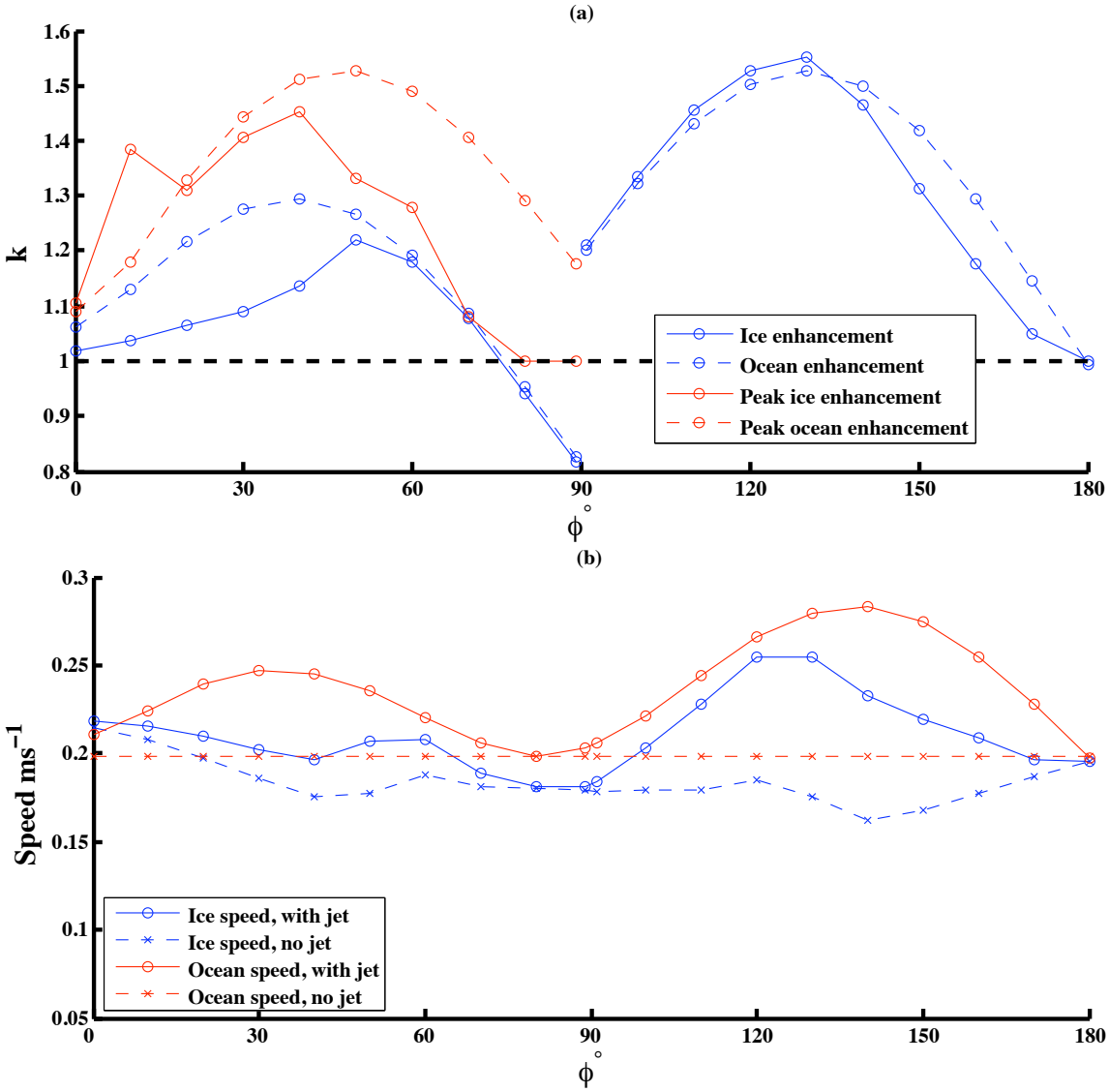


Figure 6.6: Ocean jet formation for varying $\phi$, velocities taken 1 km from the ice edge. Plot (a) is the enhancement of the ice and ocean velocities parallel to the ice edge. As with figure 6.4(a) the peak jet is plotted for $0° < \phi < 90°$ and corresponds to the thin oceanic jet 500 m from the ice edge. Plot (b) is the absolute speed of the ice and ocean at 1 km from the ice edge.

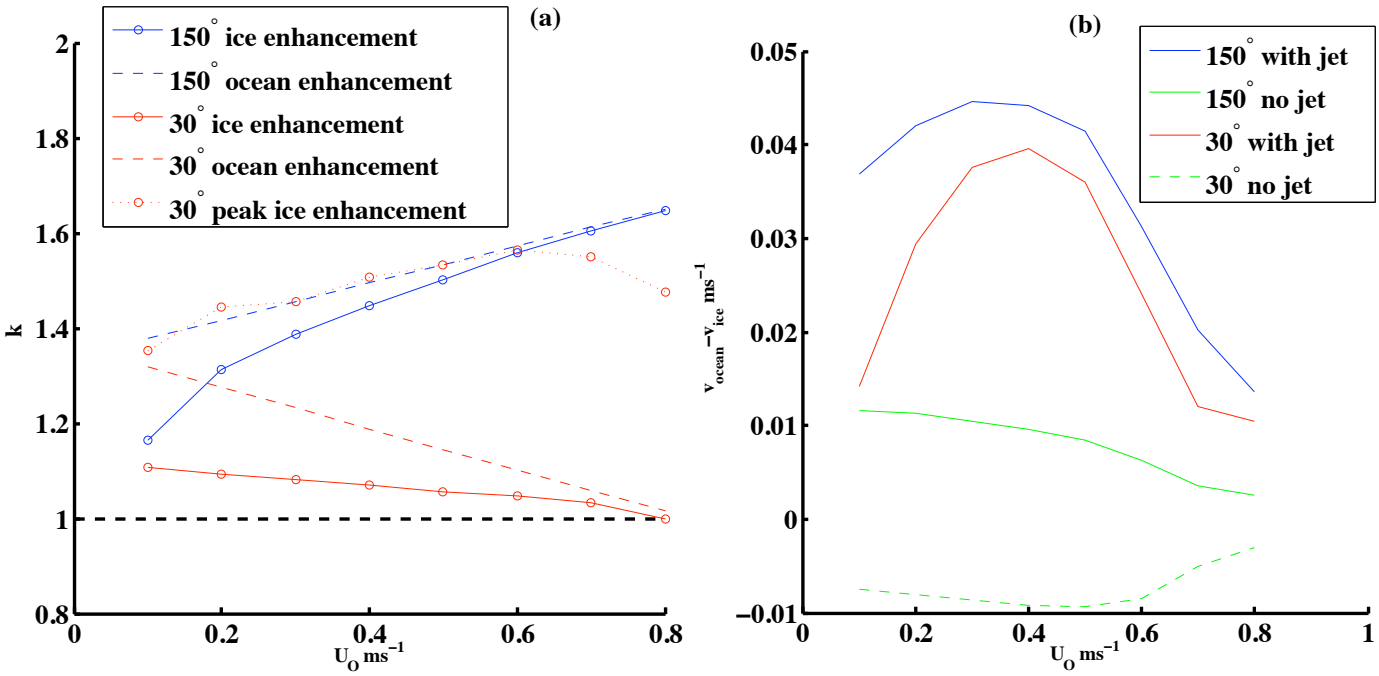


Figure 6.7: Ocean jet formation for varying ocean speed $U_O$. Plot (a) is the enhancement factor k of the velocity components parallel to the ice edge at 1 km, the 'peak' velocity at 500 m is plotted for the 30° case as with figures 6.4(b) and 6.6(a). Plot (b) shows the difference between the parallel component of the ice and ocean at 1 km as in figure 5.5.

Figure 6.7(b) shows the westward difference between the sea and ocean for $\phi = 30°$ in the green dashed line. The difference is negative for all far field ocean current speeds due to the parallel component of the sea ice velocity being greater than that of the ocean.

### Analytical Model Comparisons

The size and shape of the sea ice jets are similar for both models. The component of the sea ice velocity parallel to the sea ice edge is of similar magnitude for the demonstration calculations although the spatial profile in the CICE model is not as well correlated (figures 5.3(b and e) and 6.5(b and e)) .

The stress balance calculated by the CICE model (figures 6.5(c and d)) is of a different magnitude to that calculated by the analytical model (figures 5.3(c and d)). The difference in stress is due to the drag coefficient between the ocean and ice. For the analytical model a value of $C_O = \Delta C_F \approx 0.011$ is used to represent the broken ice floes and therefore rougher underside of the sea ice pack expected in the Marginal

Ice Zone (see section 3.2.4). This value is different in the CICE model. A value of $C_O = 0.00536$ is used by the model representing the continuous sea ice pack. Using this lower value in the analytical model results in a stress balance of with a similar magnitude to that seen in figures 6.5(c and d). Despite the difference in stress the speed of the ice drift is similar for both the models.

The angular dependence of $u^2_{\text{diff}}$ has been considered in the creation of the jets with the CICE model. The far field ocean current speed dependence has not. The ocean enhancement in figure 6.7(a) and the ocean speed in 6.7(a) are similar to the ones in figures 5.4(a) and 5.5(a), with the jets applied to the CICE model being more intense. The dependence upon the far field current speed (figure 6.7(a)) is different. The $u^2_{\text{diff}}$ term used to calculated the ocean jet strength applied to the CICE model does not consider the far field ocean current speed (see end of section 6.1.1). This gives the relation between the ocean velocity enhancement and the far field ocean current speed a similar form to the atmospheric jet seen in figure 6.4(a).

The angular dependency of the sea ice response to the ocean jet in the CICE model is different to that predicted in section 5.2.2. The assumption in the analytical model that the compaction of the sea ice edge will resist ice drift normal to the ice edge (see section 4.2.1) is not true for the experiments with the CICE model. The CICE model ocean and ice drift speeds are similar over all angles of incidence (figure 6.6(b)) and all current speeds (figure 6.7(b)) with a difference in drift direction of $\approx 15^\circ$ (figure 6.5(f)). This is in contradiction to the assumptions used in calculating the jet strength.

The ocean jet strength is dependent upon the difference in velocity between the ocean and ice edge, the $u^2_{\text{diff}}$ term in equation (3.2.11b). This term was parameterised using the results from the analytical model in figure 5.6(a). The ocean jets used in these CICE experiments are therefore not consistent with the ice drift calculated by the model. The jet theory presented in chapter 3 predicts that only ocean jets with a low enhancement of $k < 1.1$ will be able to form for the ice drift calculated by the CICE model. Such a low enhancement makes little difference to the state of the sea ice edge.

### 6.2.3 Combined Jets

The 1 km grid has been used to apply both the atmospheric and oceanic jets to the sea ice edge. The calculations from section 5.2.3 with aligned (figure 5.7(a)) and opposing (5.7(b)) jets have been repeated using the CICE model. The sea ice is unconstrained and free to deform in all directions. The model was run

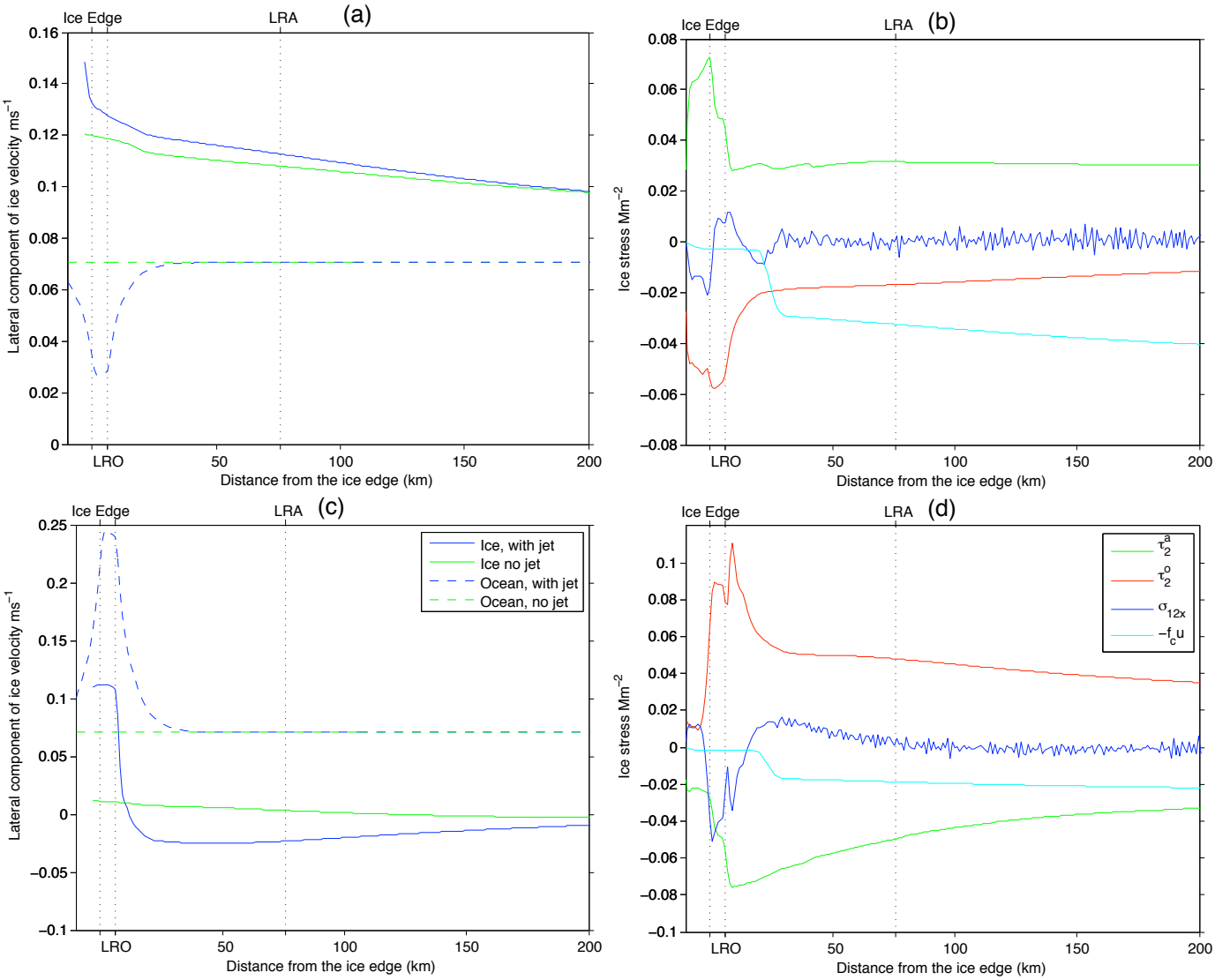


Figure 6.8: Sea ice response to the formation of atmospheric and oceanic jets. Plots (a) and (b) are jets at $\phi_a = \phi_o = 45°$ as in figure 5.7(a). Plots (c) and (d) are for jets at $\phi_a = 135°$ and $\phi_o = 45°$ as in figure 5.7(b). Plots (a) and (c) are the ice and ocean velocities coloured as in figure 5.7. Plots (b) and (d) are the parallel components of the ice stresses coloured as in figure 6.3(d).

for 12 hours to allow the sea ice dynamics to develop in time. The far field wind and ocean current speeds are the same as the analytical calculations with $U_A = 5$ m s$^{-1}$ and $U_O = 0.1$ m s$^{-1}$. The strength of the ocean jets was taken from the analytical calculations in section 5.2.3 by imposing the associated values of $u^2_{\text{diff}}$.

### Aligned Jets

With both the atmosphere and ocean approaching the sea ice edge at angle of $\phi_a = \phi_o = 45°$ a semi-steady state was reached after 4 hours. The ice initially moves very fast, at almost twice the speed of the ocean. This results in a very high ocean drag resisting the motion of the ice, decelerating it to the state shown in figure 6.8(a). Here the atmospheric stress is balanced by the ocean drag, internal ice stresses and Coriolis acceleration. The internal ice stress has large spatial variations at the extreme ice edge, changing sign several times in the outer 30 km of sea ice. At the extreme sea ice edge, the step change between the positive and negative side of the second order atmospheric jet occurs at the same location as the oceanic jet causing little spatial change in the sea ice velocity. The component of the ice velocity normal to the ice edge is high ($\approx 0.13$ m s$^{-1}$) and has the ice moving faster than the ocean. This contradicts the assumptions behind the formation of the oceanic jet (see section 3.2). Such a physical situation is unlikely to exist as the difference in speed between the ice and ocean is not such that an ocean jet could form. The ocean jet formation would be possible for ocean currents approaching parallel to the ice edge.

### Opposing Jets

With the atmosphere and ocean opposing each other a semi-steady state was again reached after 4 hours. As with the analytical model (figure 5.7(b)) this alignment has the greatest enhancement of the oceanic jet and the greatest response of the sea ice to it. Away from the extreme edge the atmospheric stress and ocean drag oppose each other (figure 6.8(d)) to give almost no ice drift parallel to the ice edge. The ice movement is normal to the ice edge at $\approx 0.07$ m s$^{-1}$, which is less than the ocean speed. The large ocean jet forms a thin and intense sea ice jet at the extreme edge. There is a large spatial change in ice motion, from no parallel drift in the far field to a drift of over 0.1 ms$^{-1}$. This large spatial change causes a large change in internal ice stress.

### Analytical Model Comparisons

The CICE model has produced a sophisticated model of combined jet formation at the sea ice edge. The analytical model in chapter 4 is unable to consider internal ice stresses that change direction. This spatial

variation is evident in the CICE model (figure 6.8(b and d)). The lateral ice velocities in both the CICE and analytical model are similar over the extent of the atmospheric jet.

As with the ocean jet experiments in section 6.2.2, the aligned atmospheric and ocean jets present an unlikely physical situation. The ice drift normal to the ice edge is much greater than predicted by the analytical model and therefore an ocean jet would not be expected to form. The opposing jet experiment (figure 6.8(c) and (d)) does present a valid ocean jet.

# CHAPTER 7

# DISCUSSION

In this final chapter the results of the thesis are discussed. The model of atmospheric and oceanic jet formation is summarised in section 7.1. This summary includes observations that are linked with jet formation (section 7.1.1) along with analysis of where jet are likely to form (section 7.1.2). Modelling of the sea ice edge is summarised in section 7.2 assessing the success of the Analytical and CICE models. The results of the models are analysed to give a prediction of sea ice jet formation. Possible observations of ice edge jets are presented in section 7.2.1. The wider implications of this thesis toward ice modelling (section 7.3) and the global climate (section 7.4) are discussed. The chapter concludes with a discussion of the immediate and long term research needed to follow on from this thesis in section 7.5.

---

Sea ice plays an important role in global climate (see section 1.1). Understanding the nature of sea ice dynamics is needed to accurately model the global climate (chapter 2). The nature of the sea ice edge and the atmospheric and oceanic conditions that exist above and below it differ from those of the sea ice pack (section 1.3). However, the sea ice edge is not explicitly considered by the sea ice component of global climate models. We have performed analytical and numerical studies of the dynamics of the sea ice edge.

## 7.1 Atmospheric and Oceanic Jet Formation

The formation of atmospheric and oceanic jets has been modelled over the sea ice edge. The atmospheric jet formation is similar to coastal jets and is driven by the sharp change in surface roughness at the sea ice edge (see section 3.1.4). The oceanic jet formation is driven by a similar sharp change in surface roughness beneath the ice. The jet strength depends upon the difference in velocity of the fluid (air or ocean) and the sea ice. Since the ice moves much more slowly than the air, the ice can be considered stationary for the atmospheric jet calculation. The similarity of the sea ice drift and ocean current velocities (see section 3.2.2) makes the ocean jet problem more complex as both the ocean and ice velocity need to be considered.

For the problem presented in this thesis interaction between sea ice and ocean waves is not explicitly considered. This interaction is a controlling factor in the state of the MIZ and sea ice edge as it accounts for the smaller floe size (see section 1.3), and thus greater surface roughness. However the floe size is unlikely to change greatly due to jet formation. The subcritical wind speed associated with atmospheric jet formation is slower than the wind speed in stormy conditions which cause large ocean waves. In the study of Birnbaum & Lupkes (2002) where the surface drag of the MIZ was allowed to vary at a greater distance from the ice edge due to the form drag associated with floe edges, there was still a sharp change in surface roughness at the sea ice edge. The assumption of chapter 3, that the sea ice edge can be modelled as a slab of constant surface roughness unchanging throughout the jet formation, is therefore valid.

If the floe size and surface roughness does change due to continued jet formation on a greater time scale (over several days compared to the six hour experiments presented here) then the results in this thesis suggest that ice jet formation will not be greatly altered. When the surface roughness of the sea ice was changed to match the analytical and CICE models (see comparisons in sections 6.2.1 and 6.2.2), the sea ice drift speed was not greatly changed, although the stress balance was. This would also be true for a change in floe size. As floe size becomes smaller, due to greater wave interaction, both the ocean and atmospheric drag increases. The changing applied stresses (atmospheric and oceanic) balance themselves.

A decreasing floe size for unchanging ice concentration is unlikely to alter the dynamics of the sea ice edge. Feltham (2005) shows how the granular flow like dynamics of smaller ice floes have little effect upon the nature of the sea ice edge. A thin ice jet of approximately 1 km wide was discovered due to the granular

nature of the ice. This jet is small in comparison to the width of the atmospheric jet and is of a similar size to the thin atmospheric jet (see section 6.2.1 in particular figure 6.3(b)) or an oceanic jet. The atmopheric jet is shown to have the greater effect upon the sea ice pack.

### 7.1.1 Observations of Jet Formation

There have been several ship and airborne studies of atmospheric conditions over the sea ice edge. Of particular interest are observations of wind speed and direction which are the greatest indicator of jet formation. Sharp changes in wind stress have been predicted by Guest et al. (1995) as a cause of changes in the Atmospheric Boundary Layer (ABL). A sharp change in stress fits well with the second order discontinuity in the wind speed perturbations in figure 3.3. Guest et al. (1995) also give observations of wind stress at the sea ice edge with the maximum just iceward of the sea ice edge during on-ice wind conditions in the Fram Strait. This is well correlated with a jet forming during winds at $90^\circ < \phi < 180^\circ$ to the ice edge. No information about the angle between the wind and the ice edge is presented in the study. Orr et al. (2005*a*) attribute sharp changes in cloud conditions over coastlines to the sharp change in wind speed caused by jet formation. Such cloud conditions have been observed over the sea ice edge (Fairall & Markson 1987).

Atmospheric jet formation predicts changing wind speeds over an atmospheric Rossby radius. Guest et al. (1995) show changing surface wind speeds across the sea ice edges in the Antarctic and Arctic Oceans. They combine previous studies along with original data. Wind speeds are shown to vary over the order of 100 km from the sea ice edge during on-ice wind conditions. These events happened for wind speeds of $< 15$ m s$^{-1}$ so fit well with the atmospheric jets presented in this thesis (low Froude number conditions require $U_A < 11$ m s$^{-1}$ but the perturbed wind speed can be greater than this). The observations of Andreas et al. (1984) have a similar form. Guest et al. (1995) also comment that atmospheric mesocale features of length scale less than 30 km are difficult to resolve from the aircraft borne measurements that were used for the study.

There are limited available observations of ocean currents at the sea ice edge that either show or disprove jet formation. Such observations would have to be over a scale of less than 10 km (comparable to an oceanic Rossby radius $\mathcal{L}_{RO} \approx 6$ km).

The form of the atmospheric jets, in particular the second order discontinuity, is in agreement with

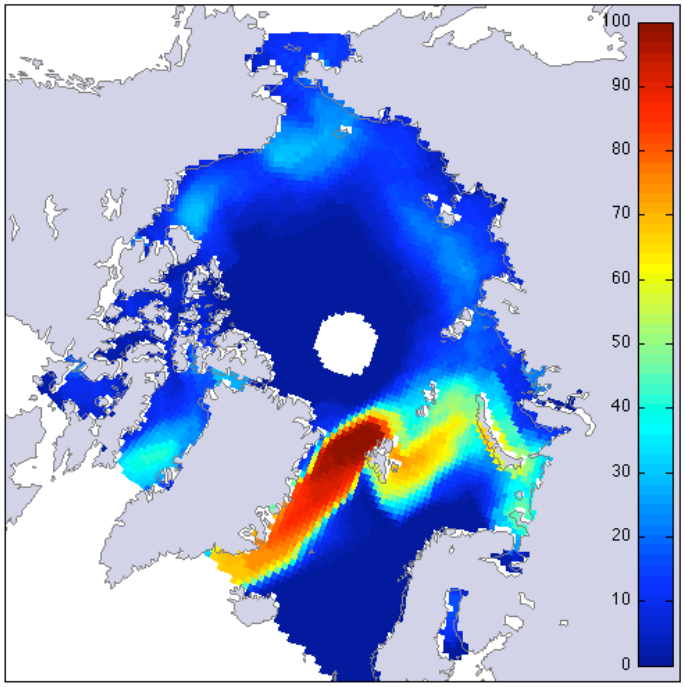


Figure 7.1: Areas of possible atmospheric jet formation in the Arctic from NSIDC SSMI ice concentration data 1990 to 2008 (monthly averages). Colour shades represent the percentage of the data that could contain an atmospheric jet formed over a sea ice edge when considering the sea ice edge location but not the wind direction.

Glendening (1994). The model of Glendening is a numerical model of the ABL which is primarily forced by a thermal change between the sea ice edge and open ocean and the occurrence of a coastal front along the sea ice edge although changes in surface roughness are also considered. An along ice jet was observed to arise from the model with a discontinuity between ice on the right (analogous to $0° < \phi < 90°$) and ice on the left ($90° < \phi < 180°$) of approach winds. This discontinuity is likewise attributed to the Corilois acceleration of the wind. It is shown that the model agrees with the observations and modelling of Guest et al. (1995).

### 7.1.2 Areas of Likely Jet Formation

For atmospheric jets to form a sharp change in surface roughness length is required. A compacted sea ice edge gives such a sharp change. For the jet to be the driving wind feature, the ice edge needs to be in the open ocean to avoid wind processes formed over land masses and ice shelves due to changes in surface elevation (Hunt et al. 2004). Locations that fit these requirements can be found by looking at ice concentrations.

Ice concentration from the National Snow and Ice Data Centre (NSIDC) (Cavalieri et al. 1996) has been used to give the location of the sea ice edge in the Arctic ocean from 1990 to 2008 inclusive. The data is satellite Special Sensor Microwave Imager (SSMI) data given as averaged monthly ice concentrations. The ice concentration has been processed using the same method as in section 6.1.1 to give the areas where the ice edge allows for an atmospheric jet to form. The criteria for a jet to form is that there is a sufficiently compacted ice edge, in this case, open ocean within 70 km of sea ice of concentration greater than 80%. The data available was of $\approx 50$ km resolution.

The ice concentration map gives one main area where an ice edge allowing for jet formation is present. This is in the Fram Strait and Greenland Sea (high percentage red area in figure 7.1). The Fram Strait is a highly studied area of the Arctic. This is due to the ice drift in this area accounting for 90% of the sea ice leaving the Arctic basin (Vinje & Finnekåsa 1986).

Ice drift in the Fram Strait can be calculated from Synthetic Aperture Radar (SAR) images from satellites (Korsnes 1994). Images taken at various time intervals are compared to show the distance moved by the sea ice. Kwok (2004) gives a summary of ice drift through the Fram Strait over the period 1978 to 2002. The average ice drift in this period is 866,000 $\text{km}^2\ \text{yr}^{-1}$, which is equivalent to $\approx 100\,\text{km}^2\ \text{hr}^{-1}$. When an atmospheric jet forms over the sea edge the results of this thesis show that the sea ice drift beneath it will increase. This increase is calculated in chapters 5 and 6 to be $\approx 5 - 20\,\text{km}^2\ \text{hr}^{-1}$, with greater values possible for winds parallel to the ice edge. This increase is over the outer 250 km of ice pack compared to the 780 km width of the Fram Strait. The possible ice drift increase due to the formation of an atmospheric jet is significant at around a quarter of the total ice drift through the Fram Strait.

To view possible locations of jet formation, information about wind direction is needed along with ice concentration. This is most easily available from a Global Climate Model. Presented in figure 7.2 is analysis

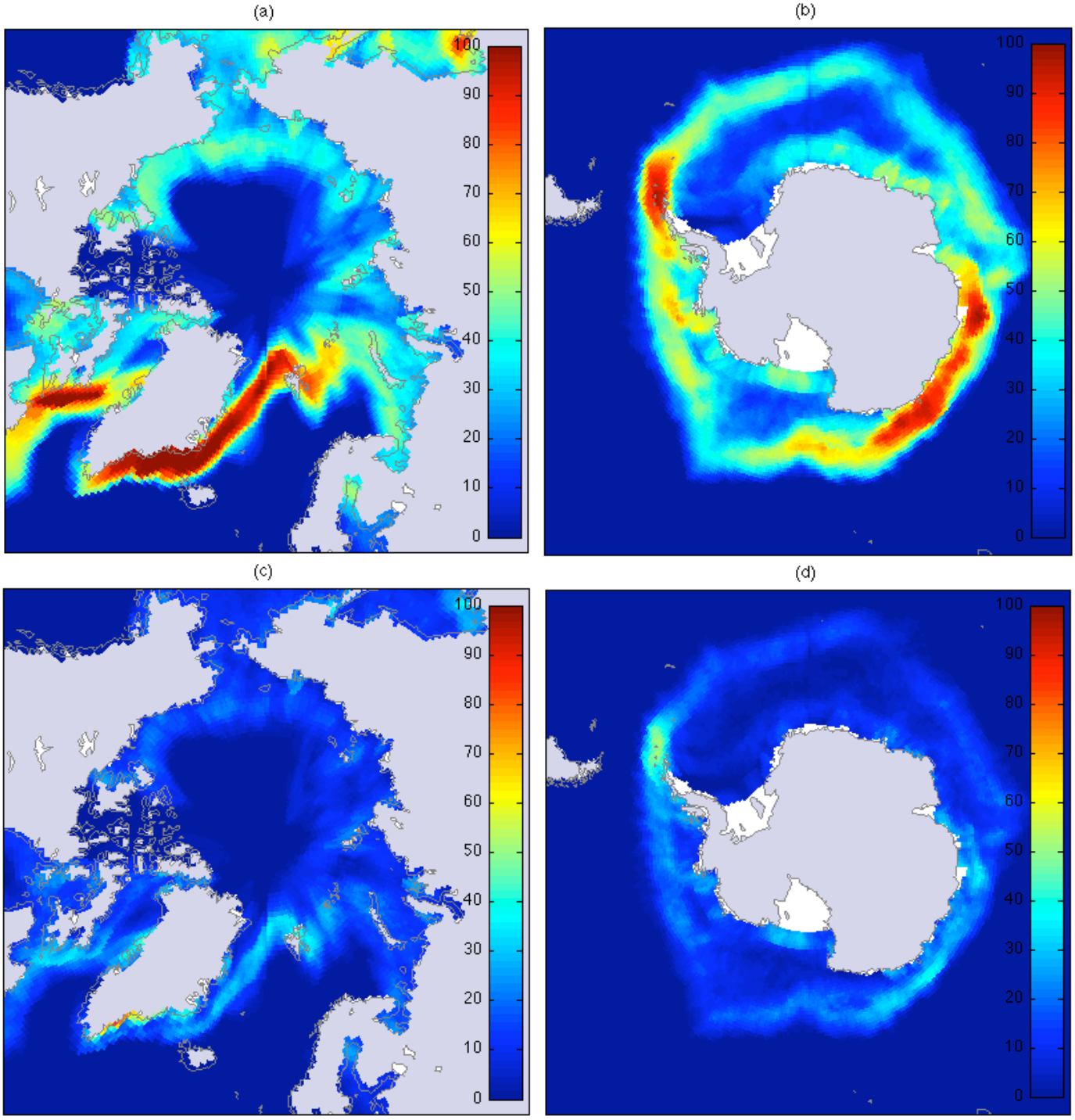


Figure 7.2: Areas of possible atmospheric jet formation in the HadGEM2 model (2 years of daily ice concentration and wind data). Plots (a and b) are percentage of the data that could contain an atmospheric jet formed over a sea ice edge (same analysis as presented in figure 7.1). Plot (c and d) show the percentage of the data in which the wind direction and strength allow for an atmospheric jet over a sea ice edge.

from two years of daily output from the Hadley Centre Global Environment Model version 2 (HadGEM2) developed by the Met Office Hadley Centre (Collins et al. 2008). The output is from a model run that has a similar mean sea ice extent to observations in the period 1990 - 2000. The daily averaged winds were the highest time resolution available. As the wind speed and direction can change hourly, averaged wind data may miss possible times of jet formation. Daily wind records for an entire polar region are not easily available from observations. The output is given at $\approx 50$ km resolution.

The ice concentration is analysed as the NSIDC data shown in figure 7.1 to give areas in which an atmospheric jet is able to form. The wind speed and direction in these areas is then checked to see if a jet would form. The criteria for this is that the wind is on-ice ($0° < \phi < 180°$ see figure 3.2 in chapter 3) and that the wind is subcritical ($U_A < 11$ m s$^{-1}$). These conditions are in accordance with jets presented in this thesis, although jet formation during off-ice winds may also be possible. The subcritical limit is used to remove wind conditions which are inconsistent with the assumptions in the jet calculations in chapter 3. The turbulent processes that form the jet have a length scale several orders less than the resolution of the model (100 m compared to a resolution of ≈50 km) and are not parameterised into it. The jets are therefore not expected to feature in the data analysed and no evidence of their formation in the model has been found (for example there is no increased wind speed above the ice edge for on-ice winds).

For the Arctic the model data gives two main areas where atmospheric jets can form. In the Fram Strait and Greenland Sea as with the NSIDC data in figure 7.1 and also in the Labrador Sea west of Greenland (see figure 7.2(a)). There is an ice edge allowing for atmospheric jet formation in these areas for 90 - 100% of the data. When considering the winds these two areas have subcritical on-ice wind allowing for jet formation for 40 - 50% of the time or approximately half of the time when there is an ice edge allowing for jet formation (see figure 7.2(c)).

There is an other area of possible jet formation that only occurs during the summer. The area of the Arctic Ocean north of the Bering Strait between the Beaufort and East Siberian Seas has a long ice edge which allows for atmospheric jet formation (shown by the blue green in figure 7.2 (a)). The interaction between the atmosphere and sea ice edge in this area, in particular the movement of storms, has been studied by Long & Perrie (2012). Atmospheric jets were not included in this modelling study.

For the Antarctic there are two main areas where atmospheric jets can form. One is east of the Antarctic

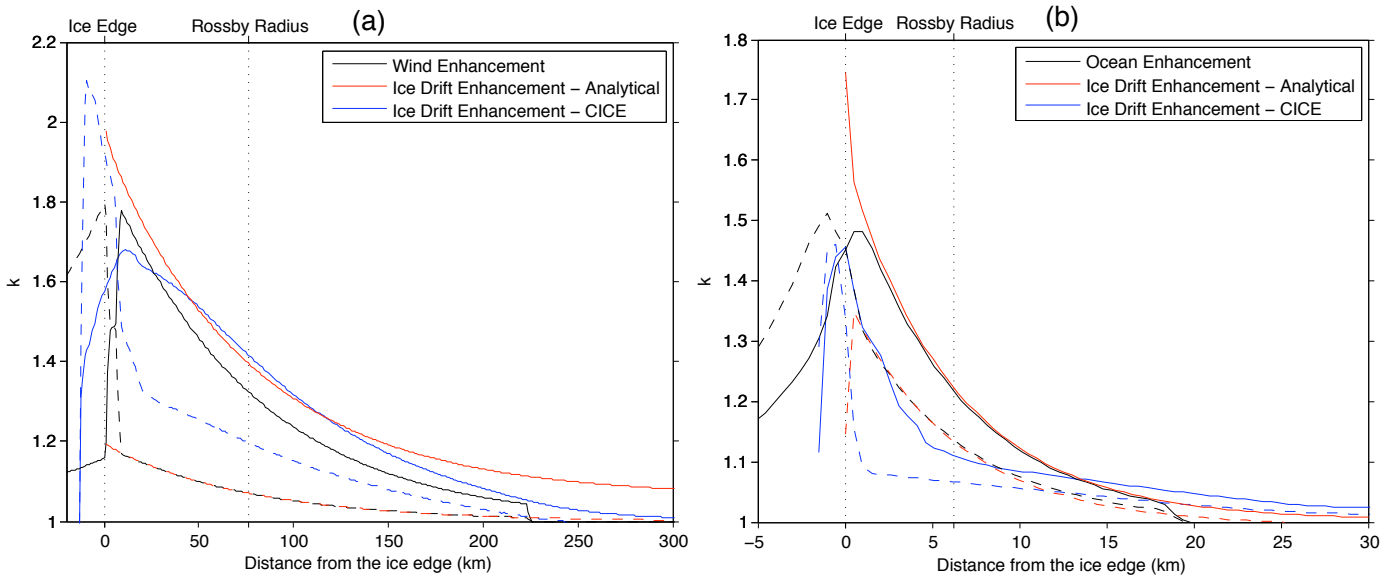


Figure 7.3: Enhancement of parallel components of velocities due to atmospheric jet (plot (a)) and oceanic jet (plot (b)) formation in both Analytical and CICE models (see legend). The solid lines for the positive, dashed lines for the negative second order part of the jet. Plot (a) is combination of figures 5.1(e) and 6.3(e), plot (b) a combination of figures 5.3(e) and 6.5(e) repeated here for convenience.

Peninsula in the Weddell Sea. The other is off of East Antarctica between Wilkes Land and the Ross Sea. Both of these areas have an ice edge allowing for jet formation at 80-100% of the time. When considering the wind strength and direction an atmospheric jet would be expected to form around 40-50% of the time.

## 7.2 Ice Jet Formation

An idealised analytical model of the sea ice edge has been produced (chapter 4). This model uses a viscous-plastic rheology to describe sea ice stress. Despite the complexity of the stress regime, the model produces stable solutions within little computational time. Free drifting ice at the extreme edge of the sea ice pack has been matched to the ice pack solution. The free drifting ice is in good agreement with the ice pack solution as the ice concentration decreases. Despite the simplifications and restrictions in the analytical model, its results are in agreement with the Los Alamos numerical sea ice climate model (CICE) which uses the same sea ice rheology. The agreement is strongest for the atmospheric jet experiments where the longer length scale ($L_{RA}$ an order greater than $L_{RO}$) allows for smoother solutions to the CICE model. For the ocean

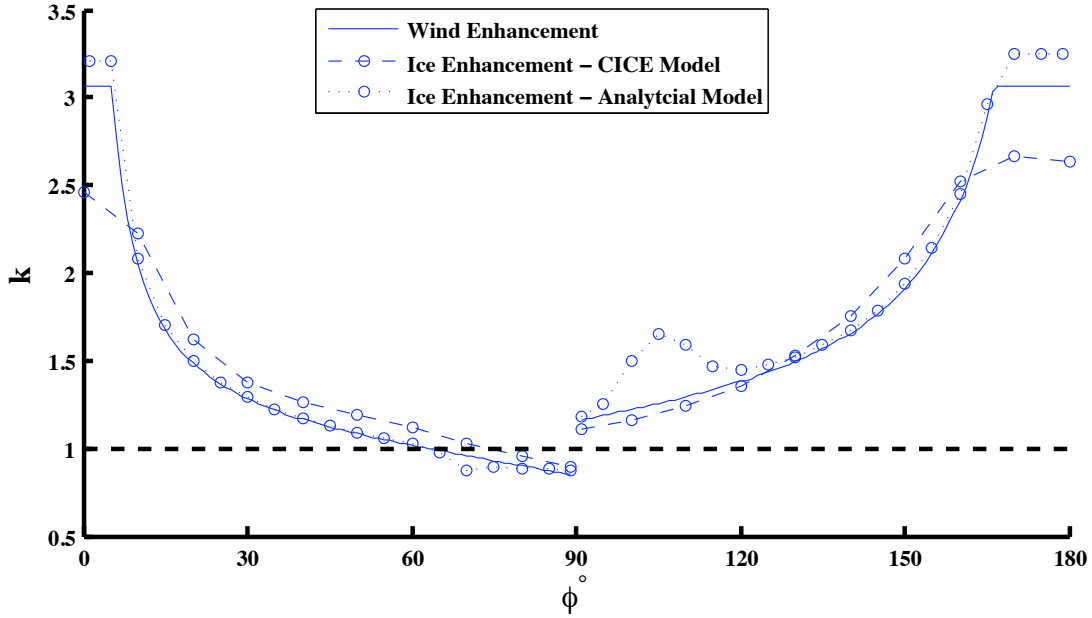


Figure 7.4: Peak parallel velocity enhancement for atmospheric and ice jets in both Analytical and CICE models (see legend) at the sea ice edge avoiding the thin atmospheric jet. This is a combination of figures 5.2(a) and 6.4(a) repeated here for convenience.

jet, the faster moving sea ice contradicts the assumptions used to create the analytical model. The analytical model was unable to accurately model the ice drift during the formation of both atmospheric and oceanic jets. This is due to simplifications within the model causing it to be unable to reproduce the internal stresses caused by a change in ice drift direction. The results in this thesis show the validity of a simplified dynamical model to observe processes at the sea ice edge.

Ice jet formation has been observed in the analytical model (chapter 5) and the CICE Model (chapter 6). Perturbations to winds and ocean currents over the sea ice edge cause perturbations to the sea ice drift. These perturbations are of the same size and relative enhancement resulting in a good match in figure 7.3 of the analytical and CICE models, particularly for the atmospheric jet in 7.3(a). The perturbations to the ice drift form an ice jet parallel to the ice edge, alter the dynamics of the sea ice and increase the ice transport along the ice edge.

The atmospheric jet size and strength varies for changing wind conditions. This variation is seen in

the ice jet in both the analytical and CICE models with a good agreement between the two in figure 7.4. The formation of this ice jet alters the sea ice edge. The amount of ice transported along the sea ice edge increases when a jet is present. This is an increase of $\approx 5 - 20$ km$^2$ hr$^{-1}$ which is an increase of around 40% over the outer 250 km of the sea ice pack (see equation (5.2.1) in section 5.2.1 and equation (6.2.1) in section 6.2.1). The drift increase is also comparable to the ice drift through the Fram Strait. The ice drift in the Fram Strait is responsible for 90% of the ice outflow from the Arctic ocean and plays a major role in the state of Arctic sea ice (see section 7.1.2). Also due to the Coriolis acceleration of the sea ice, increasing the ice drift velocity parallel to the sea ice edge alters the compaction or dispersion of the sea ice pack.

For calculations using the analytical model the ocean jet intensity was coupled to the ice drift calculations. The strength of the ocean jet is dependant upon the difference in velocity between the ice drift and ocean current, $u^2_{\text{diff}}$. For this reason the jet intensity and ice drift speed are calculated as a coupled system (see section 4.3.2). The value of $u^2_{\text{diff}}$ associated with both the jet strength and ice drift is used to give a solution for the ice edge (see section 4.3.3). The jet strength for varying ocean currents in this model gave a parameterisation for the ocean jet strength to be used in the CICE model (see figure 5.6 in section 5.2.2 and section 6.1.1). Due to simplifications and constraints in the analytical model, the ice drift calculated in the analytical and CICE models is not in good agreement resulting in little correlation in figure 7.5 particularly in the region $60 < \phi < 120$.

The ice drift velocity calculated by the CICE model is very similar to the ocean current velocity for all the ocean jet experiments. This directly contradicts the assumption in the analytical model that the ice drift normal to the ice edge is reduced due to the compaction of the sea ice. The difference between the ice drift and ocean current (given as $u^2_{\text{diff}}$ in section 3.2.2) in the results from the CICE model is small. This gives a small ice jet intensity (the magnitude of the perturbation to the ice drift) for all occasions when the ocean stress dominates the sea ice-ocean momentum balance.

If the compaction of the ice edge does not significantly reduce the component of the ice drift velocity normal to the sea ice edge, then ocean jets as described in chapter 3 are unlikely to form. The results from the CICE model suggest that the applied stress from a moving ocean is too great to be countered by a compact ice edge. Therefore ocean jets are unlikely to play an important role in ice edge dynamics.

Ocean jets are only likely to form during specific arrangements of winds and ocean currents encountering

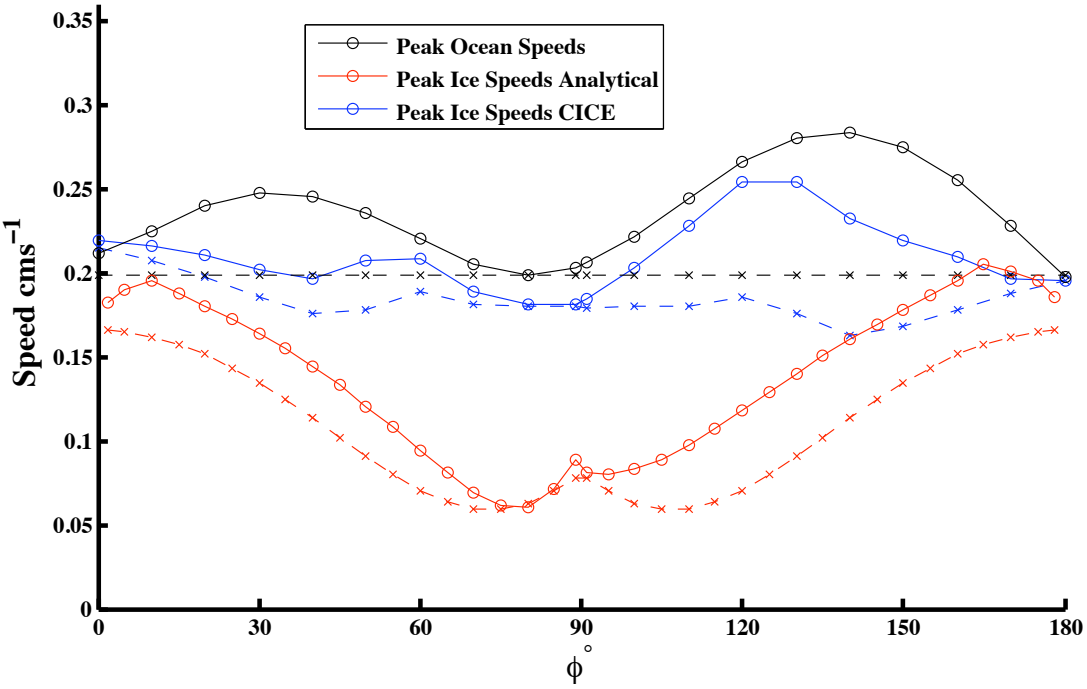


Figure 7.5: Peak ocean and ice speed for ocean and ice jets in both Analytical and CICE models (see legend) at the sea ice edge avoiding the thin oceanic jet. Solid lines are for situations with a jet, dashed for without a jet. This is a combination of figures 5.4(b) and 6.6(b) repeated here for convenience.

the sea ice edge. If the applied wind and ocean stress are such that there is a significant difference between the ice drift and ocean current then an ocean jet will be able to form. One such arrangement is shown in figures 5.7(b) and 6.8(c and d) and has the direction of the wind and ocean current separated by $90°$. Winds and ocean currents are often separated by such an angle due to the Ekman spiral (Csanady 2001), though the possibility of such an arrangement over the sea ice edge is unknown.

### 7.2.1 Observations of Ice Jet Formation

Ice jets, that we presume to be caused by an atmospheric jet above them (ocean jet also possible though more unlikely), have been observed. Johannessen et al. (1983) show ice jets that extend over 50 km into the sea ice pack during on-ice winds. The ice speed is approximately 0.3 ms$^{-1}$ at the ice edge decaying to 0.2 ms$^{-1}$ at 250 km into the sea ice pack (see figure 1.4 in particular (a) from 19 September and (b) from 27

September). The winds are parallel to the ice edge at a speed of approximately 10 $ms^{-1}$. No information about the varying wind speed into the pack is available. The ice edge is recorded as being straight and well compacted.

These observations fit well with the occurrence of an atmospheric jet over the sea ice edge. The wind speed and direction agree with the presence of an atmospheric jet and the ice jet is of similar size to the ice jets calculated in chapters 5 and 6. Johannessen et al. comment "that the ice edge jet is a ubiquitous, wind-driven feature" and the decay of wind stress into the ice pack is in correlation to the decay in ice drift speed. The location of this ice jet is in the Arctic Ocean north of Svalbard and the Fram Strait. This correlates with the Fram Strait being a key area for possible atmospheric and ice jet formation (see section 7.1.2).

Greenan & Prinsenberg (1998) present observations of ice drift and wind speed in the MIZ. These observations are of buoys mounted on-ice floes in the Labrador sea. Although it is not possible to analyse these observations to show atmospheric or ice jet formation, the relationship between the ice drift and wind speeds is applicable. For the buoy located within the ice pack the ice drift speed was observed to be approximately 0.9% of the wind speed with a value of $\approx 2.6\%$ for the bouy in the MIZ. The results from both the analytical (chapter 5) and CICE (chapter 6) give values of 0.9-1.6% for within the sea ice pack (at 100-150km from the ice edge) and 1.2-1.9% for the ice edge. This comparison suggests that this thesis may be underestimating the ice drift speed at the ice edge. The results from Greenan & Prinsenberg have a lower ice concentration and thinner ice in the marginal ice zone than the values used in this thesis. Also small ocean currents are observed to be aligned to the ice drift. This accounts for the faster ice drift.

## 7.3 Implications for Sea Ice Modelling

It has been shown that a sea ice jet can form in the CICE model (chapter 6) due to the presence of an atmospheric jet. The best model response is for a maximum grid cell size of 2 km. The results in this thesis can not give an accurate resolution at which ice jets can form due to the atmospheric jet above. The results in figure 6.2 show a good response at 1 km and 2 km resolution with inconsistent results at 5 km resolution. The sea ice component of current climate models are approaching high resolutions of 2 km (McClean et al. 2010, Maslowski et al. 2012). The method documented in section 6.1.1 could be

parameterised into the CICE or other sea ice model, to alter the wind speeds before they are applied to the sea ice. The jets would be able to follow a moving ice edge and the model would show how the presence of jets will affect the sea ice on a global scale.

For sea ice models running at a resolution with grid cells wider than 2 km the ice jets could be difficult to include. From the results in chapter 6 it would be possible to create a parameterisation that would add in an ice jet to a sea ice model by perturbing the sea ice drift. These perturbations would mimic the ice jet formed by the arrangement of winds and ocean currents and the sea ice edge. However, adding such perturbation to the sea ice drift would form an imbalance in the ice drift momentum. Such an imbalance does not make for a well functioning model.

If atmospheric jets are present in climate models the results in this thesis indicate that ice edge jets will form. If the atmospheric jets are not present, then they could be added to the wind above the sea ice edge using the method described in section 6.1.1. Adding the jets in this manner does however introduce a similar imbalance as perturbing the ice jets into a sea ice model.

Jet formation due to a sharp change in surface roughness is caused by the interaction of the atmosphere or ocean with the sea ice edge. In order to model this process it needs to be considered in the coupling of the sea ice and atmosphere or ocean component of a climate model. The coupling process of the HadGEM3 model described in chapter 2 simply passes forcing data between the components. This process is typical of climate models and would not allow for the jet formation described in this thesis. The turbulence that is responsible for the jet formation is of the order 10 m in scale (Hunt et al. 2004), far too small to be resolved by a climate model. To include these jets within a climate model and investigate their role in the global climate (discussed in the next section 7.4), a coupling process that considers and parameterises sub-grid scale phenomena is required.

## 7.4 Implications for Global Climate

Atmospheric jet formation increases the sea ice drift at the sea ice edge during on-ice winds. This increase in ice drift could play a major role in rapid ice retreats. These events have been observed by King et al. (2010) in the Bellingshausen Sea and are discussed in section 1.3. Such events are ideal for jet formation

with continued strong on-ice winds forming a compact sea ice edge. A compact sea ice edge gives a sharp change in surface roughness which drives the jet formation.

The formation of atmospheric jets over the sea ice edge could cause an increase in the formation of deep ocean water. Pickart et al. (2003) show that the Greenland tip jet makes a significant contribution to open ocean convection and the formation of ocean deep water. This jet is formed by the cold air mass over the high orography of the Greenland ice pack flowing out into the Atlantic ocean. The Greenland tip jet has been modelled by Orr et al. (2005*b*) and is of similar size and strength to the atmospheric jets calculated in chapter 3. The formation of deep ocean water is part of the global ocean circulation as discussed in section 1.1.

Atmospheric jet formation could play a major role in Arctic sea ice drift. The Fram Strait ice drift has been shown to be forced by a wind feature known as the Greenland Sea Jet (van Angelen et al. 2011). This jet is driven by temperature and surface gradient differences between the Greenland ice sheet and the Greenland Sea. As the atmospheric jets presented in this thesis are driven by changes in surface roughness (a process not considered by van Angelen et al.) they could play an additional role in the ice export through the Fram Strait. Also ice jets have been observed in this area (Johannessen et al. 1983) giving further evidence for their importance in the Fram Strait ice drift. The south Greenland Sea also experiences Barrier winds (van den Broeke & Gallee 1996) which are southerly winds flowing towards the Greenland Peninsula. These winds interact with the sea ice edge during winter allowing for jet formation.

Maslowski et al. (2012) show how current global climate models perform badly in predicting the Fram Strait ice transport, for example the CCSM3 model was shown to give an ice transport on average twice the observed value. The inclusion of atmospheric jets into sea ice models could make a significant improvement in this area due to the ice drift associated with their formation. The Fram Strait ice transport plays a major role in the state of Arctic sea ice (see section 7.2) and can influence ocean circulation in the north Atlantic due to freshwater export (Frankcombe & Dijkstra 2011).

The modelling of ice transport could also be improved by new sea ice rheologies. There have been recent developements in creating an anisotropic sea ice rheology (Wilchinsky & Feltham 2006*a*, Tsamados et al. 2012). Modelling sea ice as an anisotropic medium gives sea ice a directional memory allowing it to deform differently in different directions. This is in accordance with observations and simulations of ice

interaction on floe size scales (Wilchinsky & Feltham 2006*b*). Anisotropy could be particularly important in the Fram Strait and at the sea ice edge where the strongly directional sea ice drift present anisotropic characteristics.

As the sea ice extent reduces in the Arctic summer, more opportunities for exploration are opened up. These opportunities are for shipping routes in the north western and eastern passages, engineering and exploration for natural resources (Brigham & Ellis 2009). The safety and feasibility of these opportunities relies on accurate predictions of sea ice drift, particularly in the Fram Strait. The changing sea ice conditions in the Arctic and the new opportunities associated with them has international importance (Proelss 2009).

## 7.5 Future Work

Further investigation should be focussed upon atmospheric jet formation. This thesis has shown that ocean jets are unlikely to form. Also the high resolution needed to investigate ocean jets is currently not available in large scale sea ice models.

#### Short Term Goals

To immediately continue the research presented in this thesis the atmospheric jets should be applied to a wider area. Regional sea ice modelling could be used to investigate the role of jet formation during particular sea ice drift events. Atmospheric jet formation is likely to occur in the Greenland Sea and Fram Strait and could play a major role in the ice export from the Arctic ocean. The rapid sea ice retreats observed west of the Antarctic peninsula (Massom et al. 2006, Massom et al. 2008, King et al. 2010) give conditions for continued atmospheric jet formation over several days significantly altering the ice drift and compaction of the ice edge.

To set up such a sea ice model a high resolution is needed with grid size at most 2 km (see figure 6.2). This would require a new grid and associated land mask. The model would require some spin up and tuning along with detailed consideration of the grid boundaries. Output from a global sea ice model could be used to force the expected ice drift into the new model domain. Jets could be added to atmospheric data sets through a new parameterisation within the model which uses the method described in section 6.1.1. The

study could be extended to use an anisotropic rheology for the deformation of sea ice.

Further study into the alignment of winds and ocean currents is also needed. The majority of investigation into atmospheric jet formation in this thesis assumes a still ocean. Ice drift observations in the MIZ show that on-ice winds are often accompanied by ocean currents (Greenan & Prinsenberg 1998, King et al. 2010). The results shown in sections 5.2.3 and 6.2.3 show that a moving ocean influences the sea ice drift velocity and can lead to ocean jet formation. The analysis of winds and ice edge location behind figure 7.2 could be expanded to include ocean currents. The jet theory of chaper 3 could be then used to present a case study of the alignment of flows and the jet formation associated with them as with the combined jets experiments shown in figures 5.7 and 5.8. The analytical model from chapter 4 would calculate the ice jet formation, and could be compared to observations of sea ice drift. The analysis in section 7.1.2 could easily be expanded to other data sets. Of particular interest is the GlobICE data set (`http://www.globice.info`) which includes Arctic wide sea ice concentration and drift speed.

**Long Term Goals**

More ambitious long term research is needed to continue the ideas of this thesis. Observational data is essential to the understanding of jets within the atmosphere, ocean and sea ice.

There are currently very few studies of the sea ice edge that can be used to verify or refute the formation of atmospheric jets due to a sharp change in surface roughness. Such a study would ideally observe low level wind speeds and surface drag over several Rossby radii either side of a compact sea ice edge during on-ice winds. Observations would need to be over a time scale less than 12 hours.

The effect that atmospheric jet formation at the sea ice edge has upon the wider sea ice pack needs to be investigated. In order to do this a sea ice model for an entire polar region at high resolution is needed. The resolution requires grid cells of at most 2 km in width. Using such a model atmospheric jets could be added to the forcing data by the model itself over time scales of one or two years in model time. Long time scale effects of jet formation in areas such as the Fram Strait and the East Antarctic (see figures 7.1 and 7.2) could make significant changes to the expected sea ice cover. The CICE model as described in chapter 2 could be used though it would need to be tuned to run at such a high resolution and a spin up period would be required.

Atmospheric jets form centred over the sea ice edge. This means that half of the jet is over the open ocean. The response of the ocean to the jet formation needs to be investigated. This requires a coupled model of sea ice and ocean dynamics such as that of Roed & O'Brien (1983) or Smith & Bird (1991). This would give insight into the alignment of winds and ocean currents. Also it could give rise to the alternate ocean jets as described by Fennel & Johannessen (1998).

# CHAPTER 8

# CONCLUSIONS

In this concluding chapter the achievements of this thesis are outlined. The original techniques devised to investigate Jet Formation at the Sea Ice Edge are outlined in section 8.1 and the main results are presented in section 8.2.

## 8.1 Original Research

For this thesis original research has been undertaken to investigate jet formation at the sea ice edge. Previous research on this topic with focus upon the sea ice edge and MIZ is limited (section 1.3) with no comprehensive review published to date. This research has been reviewed for this thesis. The subject of jet formation over coastlines and low level jet formation over oceans is well researched and applicable to this thesis and is described in section 1.2.

The theory of Hunt et al. (2004) models the formation of atmospheric jets due to a sharp change in surface roughness. This theory has been applied to the sea ice edge in this thesis for the first time in chapter 3. A review of observations and modelling of sea ice roughness in the marginal ice zone has been performed to estimate the increase in surface roughness. This has allowed for the prediction of atmospheric jet size and strength in section 3.1.4.

The interaction of the ocean with the rough underside of the sea ice pack has been considered for the first time in section 3.2. Jet formation in the ocean has required the consideration of jet formation due to a fluid's interaction with a moving band of increased surface roughness. This is a new extension to the theory of Hunt et al. (2004). To apply the ocean jet theory a review of measurements of roughness lengths and drag coefficients at the sea ice ocean interface has been performed in section 3.2.4. This review has been used to investigate the ice to ocean drag in the MIZ, an area where observations are currently unavailable.

An analytical model of sea ice drift at the sea ice edge has been created (chapter 4). This model uses several simplifications in order to calculate sea ice drift without the use of a full numerical model. These simplifications are the use of a laterally invariant steady sea ice edge and assuming that the compaction of the sea ice pack will resist the movement of ice drift normal to the sea ice edge (see section 4.2). The model is constructed using the momentum balance of Gray & Morland (1994) and rheology of Hibler (1979), which are widely used in existing sea ice models (see section 2.2). Most existing studies of sea ice with the rheology of Hibler (1979) use numerical models whereas this model uses novel methods (section 5.1) to achieve analytical solutions. Despite the simplifications and restrictions we have imposed, the analytical model is able to produce realistic solutions for the ice drift during the formation of an atmospheric jet. These results are similar to those produced by the CICE model (see section 7.2), which uses the same rheology in a fully numerical model with no restrictions. The use of the analytical model is shown to be a valid method of investigating sea ice drift at the sea ice edge using a viscous plastic rheology.

The use of the CICE model to investigate the sea ice edge is a novel method not documented in previous research. The model has been set up at various resolutions to investigate the model's sensitivity to grid resolution (see section 6.1). This sensitivity is not documented in the existing literature. The method of finding an ice edge in a map of ice concentration data has been created for this thesis (section 6.1.1). This has allowed for the addition of atmospheric and oceanic jets into forcing data for the CICE model experiments and the analysis of ice concentration data to find possible locations of atmospheric jet formation (section 7.1.2). The use of the edge finding and jet applying methods allow for the consideration of jet formation in a global sea ice model. The analysis of ice concentration data to find areas of likely atmospheric jet formation over the sea ice edge has been done for the first time (section 7.1.2).

## 8.2 Original Results

Atmospheric jet formation at the sea ice edge has been modelled (chapter 3). These jets are due to the action of the Coriolis acceleration on a flow over a sharp change in surface roughness length. The Coriolis acceleration and change in roughness have been shown to exist at the sea ice edge (section 1.2) along with the other requirements for the formation of atmospheric jets (section 3.1). The arrangement of on-ice winds has been addressed in this thesis as it is more likely to present the sharp change in surface roughness length and the resulting sea ice drift will be more stable and easier to model. The shape of the jets features a peak wind speed over the sea ice edge that decays away over several atmospheric Rossby radii (75 km, see section 3.1.4). There is a first order correction to the jet shape which results in a discontinuity in wind speed at the sea ice edge. The jet perturbation to the wind speed is in the direction parallel to the sea ice and its magnitude depends on the angle between the unperturbed wind and the sea ice edge and the Froude number of the flow (section 3.1.4). The strongest jets are for winds that are near parallel to the sea ice edge where the wind speed is increased by a factor of three.

Oceanic jet formation has also been modelled (section 3.2). The physical processes behind the oceanic jets are the same as the atmospheric jets using the characteristics of the ocean mixed layer. The requirements of the flow to allow for jet formation, such as the stability of the ocean and propagation of the surface shear layer have been assumed to exist. This is due to limited available observations of the ocean mixed layer at the sea ice edge. The ocean jet shape is the same as the atmospheric jet shape though over the lateral extent of an oceanic Rossby radius (6 km see section 3.2.4). The strength of the ocean jet depends upon the difference in speed between the ocean and sea ice edge (section 3.2.2). To accurately calculate the ocean jet strength the jet calculation needs to be coupled to the analytical ice drift model as described in section 4.3.2 giving an ocean jet that increases the ocean current speed by a maximum of 50% (section 5.2.2). The results from the analytical model allow the jets to be added to the CICE model as described in section 6.1.1. The results from the CICE model, however, disagree with the analytical model and show that the compaction of the sea ice edge is not sufficient to stop the ice drift normal to the ice edge (figure 7.5). This results in the relative difference between the sea ice and ocean velocities being small and no ocean jet likely to form (section 7.2). This result from the CICE model shows that ocean jets are less likely to form than atmospheric jets.

The formation of atmospheric and oceanic jets over the sea ice edge has been shown to result in the formation of a sea ice jet (chapters 5 and 6). The sea ice jet formation is particularly likely for on-ice winds over all angles of incidence between the unperturbed wind and sea ice edge (see figures 3.2 and 7.4). The sea ice jet that forms under an atmospheric jet has a similar enhancement to the atmospheric jet (sections 5.2.1 and 6.2.1), for example a wind speed increase of 100% results in an ice drift speed increase of 100%. The sea ice jet that results from an atmospheric jet matches an observed sea ice jet north of Svalbard (Johannessen et al. 1983) and is shown to significantly increase the transport of sea ice along the sea ice edge by 40% over the outer 250 km of the sea ice pack. This increase in sea ice transport could be a significant factor in the Fram Strait ice export (section 7.1.2), an area where atmospheric jet formation is likely to occur over the sea ice edge (figure 7.2). Current global climate models typically misrepresent the Fram Strait ice export (section 7.4) a process that can have large implications for the Arctic sea ice extent (section 2.1).

# APPENDIX A

# THE VISCOUS PLASTIC SEA ICE RHEOLOGY

When modelling sea ice as a continuum, a method of relating the deformation rates and internal stresses, or its rheology, is needed. With early sea ice models such as Reed & Campbell (1960) this was done simply by considering the sea ice cover as a highly viscous fluid. This method was improved by adding an internal ice pressure (e.g. Rothrock 1970), and then by considering it as a plastic medium such as the AIDJEX (Arctic Ice Dynamics Joint Experiment) model (Coon et al. 1974). At low stress rates sea ice is observed to behave in a non deforming motion. A hybrid rheology is used giving a non plastic deformation at low stress rates. Hibler (1979) introduced a Viscous - Plastic (VP) rheology which is described in this appendix. See Feltham (2008) for a full description of sea ice rheology and methods used to model it.

## A.1 Viscous and Plastic Deformation

For a continuum sea ice model at a length scale greater than individual sea ice floes the dynamics of the sea ice have been assumed to be isotropic, that it obeys the same rules of deformation in all directions. Anisotropy in a continuum sea ice model has recently been investigated (Tsamados et al. 2012) and, while shown to be important to the central pack, would be expected to have little impact over the shorter length scales investigated in this thesis. For normal stress levels in the VP rheology the ice deforms as a plastic. In

plastic deformation energy is lost in deforming the ice. This lost energy creates kinematic features in the sea ice pack such as ridges for compressive stresses, or leads (cracks extending for many kilometres) for tensile stresses. For low stresses the sea ice is taken as a viscous fluid.

The transition from viscous to plastic deformation happens at the yield stress. This yield stress is expressed mathematically as a curve in the principle stress space (figure A.1) which is chosen to match known characteristics of sea ice deformation. The sea ice is assumed to be strong in shear, strongest in compression and weak in tension, often with no stress in pure divergence. Sea ice is plastically, or permanently, deformed for all stress states on the yield curve.

## A.2 Numerical Implementation

To mimic the deformation of sea ice in a continuum model an ice stress tensor is used. This tensor relates the deformation rate of the sea ice,

$$\dot{\varepsilon}_{ij} = \frac{1}{2}\left(\frac{\partial u_i}{\partial x_j} + \frac{\partial u_j}{\partial x_i}\right), \tag{A.2.1}$$

to the internal stresses within it $\sigma_{ij}$ where $(i, j) = (x, y)$ are directional indices. Realigning in the direction of greatest stress and summing the positive and negative parts gives the principle stress component $\sigma_1$ with $\sigma_2$ at right angles to it. These components are positive for tension and negative for compression. The stress invariants of negative pressure $\sigma_I$ and maximum shear rate $\sigma_{II}$ are related to the principle stresses with

$$\sigma_I = \frac{1}{2}(\sigma_1 + \sigma_2) \text{ and } \sigma_{II} = \frac{1}{2}(-\sigma_1 + \sigma_2).$$

The stresses experienced by a packet of sea ice within the continuum defines a point in $(\sigma_1, \sigma_2)$ space. As the sea ice is assumed to be isotopic the yield curve in principle stress space is symmetric about the negative pressure axis. Hibler (1979) gives an elliptic yield curve for the VP rheology which only allows for stresses that exist within it, or upon its boundary. The regime allows non permanent viscous deformation to the sea ice for stress states that exist within the yield curve. This is mainly for low compressive stresses in both principle directions (negative to both $\sigma_1, \sigma_2$). The ice can deform viscously in shear (small tensile stress in one direction, compressive in the other), though not in pure tension (positive values on both axis).

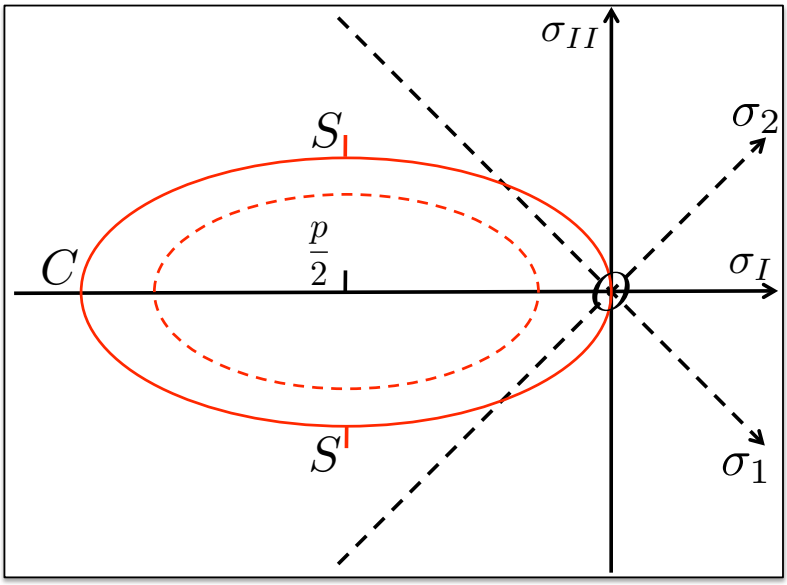


Figure A.1: Elliptical yield curve in principle stress $(\sigma_1, \sigma_2)$ space for a viscous-plastic rheology. For plastic deformation, the stress state lies on the solid curve. The stress state for pure shear is located at S giving maximal $|\sigma_{II}|$, pure convergence is at C, and pure divergence is at the origin O. For very small strain rates, the stress state moves inside the yield curve as shown by the dashed ellipse. For a zero strain rate the internal ice pressure $p/2$ must be countered.

The stress tensor is calculated with

$$\sigma_{ij} = 2\eta\dot{\varepsilon}_{ij} + (\zeta - \eta)\dot{\varepsilon}_{kk}\delta_{ij} - \frac{1}{2}p\delta_{ij}. \tag{A.2.2}$$

where $\eta$ and $\zeta$ are the nonlinear shear and bulk viscosities, $p$ is the ice pressure, and $\dot{\varepsilon}_{ij}$ is the deformation rate as in equation (A.2.1). Hibler (1979) gives the shear and bulk viscosities as functions of $\dot{\varepsilon}_{ij}$ and $p$ in accordance with the yield curve in figure A.1, with

$$\eta = \frac{\zeta}{e^2}, \tag{A.2.3a}$$

$$\zeta = \frac{p}{2\Delta}, \text{ and} \tag{A.2.3b}$$

$$\Delta = \left\{(\dot{\varepsilon}_{11}^2 + \dot{\varepsilon}_{22}^2)(1 + e^{-2}) + 4e^{-2}\dot{\varepsilon}_{12}^2 + 2\dot{\varepsilon}_{11}\dot{\varepsilon}_{22}(1 - e^{-2})\right\}^{\frac{1}{2}}, \tag{A.2.3c}$$

where $e$ is the yield curve's eccentricity. The upper bounds of the viscosity are the ice strength or pressure $p$. This is given as a function of the ice concentration $A$. This variable $0 \leq A \leq 1$ gives the non dimensional fraction of thick sea ice $(A)$ to thin sea ice or open ocean $(1 - A)$. Hibler (1979) gives

$$p = p^* h g(A) \text{ with } g(A) = e^{-c(1-A)}, \tag{A.2.4}$$

where $p^*$ is a constant, $h$ is the ice thickness and $c = 20$ is a tuning constant. The function $g(A)$ is used to represent the amount of floe contact in the ice pack (Gray & Morland 1994) with $g(A = 0) = 0$ and $g(A = 1) = 1$. This parameterisation of the ice strength gives a linear relationship between the strength and thickness for high ice concentrations. As the concentration decreases the ice strength falls significantly.

This viscous-plastic rheology and numerical derivations of it (e.g. Hunke & Dukowicz 1997) have been implemented in sea-ice models such as the Los Alamos Sea Ice (CICE) model. It has been shown to perform well at the sea ice edge (Lepparanta & Hibler 1985) which is its intended use in this thesis.

# BIBLIOGRAPHY

Aagaard, K. & Carmack, E. C. (1989), 'The role of sea ice and other fresh water in the arctic circulation', *J. geophys. Res* **94**(14), 14485–14498.

Anderson, R. J. (1987), 'Wind stress measurements over rough ice during the 1984 marginal ice zone experiment', *Journal of Geophysical Research* **92**(C7), 6933–6941.

Andreas, E. L., Claffy, K. J. & Makshtas, A. P. (2000), 'Low-level atmospheric jets and inversions over the western weddell sea', *Boundary-layer meteorology* **97**(3), 459–486.

Andreas, E. L., Tucker III, W. B. & Ackley, S. F. (1984), 'Atmospheric boundary-layer modification, drag coefficient, and surface heat flux in the antarctic marginal ice zone', *Journal of Geophysical Research* **89**(C1), 649–661.

Asplin, M. G., Galley, R., Barber, D. G. & Prinsenberg, S. (2012), 'Fracture of summer perennial sea ice by ocean swell as a result of arctic storms', *Journal of Geophysical Research-Oceans* **117**, C007221.

Belcher, S., Newley, T. & Hunt, J. (1993), 'The drag on an undulating surface induced by the flow of a turbulent boundary-layer', *Journal of Fluid Mechanics* **249**, 557–596.

Belcher, S., Xu, D. & Hunt, J. (1990), 'The response of a turbulent boundary-layer to arbitrarily distributed 2-dimensional roughness changes', *Quarterly Journal of the Royal Meteorological Society* **116**(493), 611–635. WOS:A1990DN07900005.

Bennett Jr, T. J. & Hunkins, K. (1986), 'Atmospheric boundary layer modification in the marginal ice zone', *Journal of Geophysical Research* **91**(C11), 3033–3044.

Birnbaum, G. & Lupkes, C. (2002), 'A new parameterization of surface drag in the marginal sea ice zone', *Tellus Series a-Dynamic Meteorology and Oceanography* **54**(1), 107–123.

Bitz, C. M., Holland, M. M., Weaver, A. J. & Eby, M. (2001), 'Simulating the ice-thickness distribution in a coupled climate model', *Journal of Geophysical Research-Oceans* **106**(C2), 2441–2463.

Bitz, C. M. & Lipscomb, W. H. (1999), 'An energy-conserving thermodynamic model of sea ice', *Journal of Geophysical Research* **104**(15), 669–15.

Bourke, R. & Garrett, R. (1987), 'Sea ice thickness distribution in the arctic-ocean', *Cold Regions Science and Technology* **13**(3), 259–280.

Brigham, L. W. & Ellis, B. (2009), Arctic marine shipping assessment 2009, Technical report, Arctic Council.

Broecker, W. S. et al. (1995), 'Chaotic climate', *Scientific American* **273**(5), 62–69.

Brümmer, B., Busack, B., Hoeber, H. & Kruspe, G. (1994), 'Boundary-layer observations over water and arctic sea-ice during on-ice air flow', *Boundary-Layer Meteorology* **68**(1), 75–108.

Brümmer, B. & Thiemann, S. (2002), 'The atmospheric boundary layer in an arctic wintertime on-ice air flow', *Boundary-layer Meteorology* **104**(1), 53–72.

Cavalieri, D. J. & Parkinson, C. L. (2008), 'Antarctic sea ice variability and trends, 1979–2006', *Journal of Geophysical Research* **113**, C07004.

Cavalieri, D., Parkinson, C., Gloersen, P. & Zwally, H. J. (1996), 'Sea ice concentrations from nimbus-7 SMMR and DMSP SSM/I-SSMIS passive microwave data 1990-2008'.

Chu, P. (1987), 'An ice breeze mechanism for an ice divergence convergence criterion in the marginal ice-zone', *Journal of Physical Oceanography* **17**(10), 1627–1632.

Collins, W. J., Bellouin, N., Doutriaux-Boucher, M., Gedney, N., Hinton, T., Jones, C. D., Liddicoat, S., Martin, G., O'Connor, F., Rae, J. et al. (2008), 'Evaluation of the HadGEM2 model', *Hadley Center Technical Note* **74**.

Comiso, J. C. (1994), 'Surface temperatures in the polar regions from nimbus 7 temperature humidity infrared radiometer', *Journal of Geophysical Research: Oceans* **99**(C3), 5181–5200.

Comiso, J. C. (2003), Large-scale characteristics and variability of the global sea ice cover, *in* D. N. Thomas & G. S. Dieckmann, eds, 'Sea Ice:An Introduction to it's Physics, Chemistry, Biology and Geology.', Oxford, Blackwell, pp. 112–142.

Comiso, J. C., Kwok, R., Martin, S. & Gordon, A. L. (2011), 'Variability and trends in sea ice extent and ice production in the ross sea', *Journal of Geophysical Research-Oceans* **116**. WOS:000289851800002.

Comiso, J. C., Parkinson, C. L., Gersten, R., Stock, L. et al. (2008), 'Accelerated decline in the arctic sea ice cover', *Geophysical Research Letters* **35**(1), L01703.

Coon, M. D., Maykut, G. A., Pritchard, R. S., Rothrock, D. A. & Thorndike, A. S. (1974), 'Modeling the pack ice as an elastic-plastic material', *AIDJEX Bulletin* **24**, 1–105.

Csanady, G. T. (2001), *Air-sea interaction: laws and mechanisms*, Cambridge Univ Pr.

Curry, J., Schramm, J. & Ebert, E. (1995), 'Sea-ice albedo climate feedback mechanism', *Journal of Climate* **8**(2), 240–247.

Donelan, M., Dobson, F., Smith, S. & Anderson, R. (1993), 'On the dependence of sea-surface roughness on wave development', *Journal of Physical Oceanography* **23**(9), 2143–2149. WOS:A1993LX81900016.

Drennan, W. M., Graber, H. C., Hauser, D. & Quentin, C. (2003), 'On the wave age dependence of wind stress over pure wind seas', *Journal of Geophysical Research-Oceans* **108**(C3). WOS:000182197900004.

Dyke, M. D. V. (1975), *Perturbation Methods in Fluid Mechanics*, annotated ed edn, Parabolic Pr.

Fairall, C. W., Bradley, E. F., Hare, J. E., Grachev, A. A. & Edson, J. B. (2003), 'Bulk parameterization of air-sea fluxes: Updates and verification for the COARE algorithm', *Journal of Climate* **16**(4), 571–591. WOS:000180912100002.

Fairall, C. W. & Markson, R. (1987), 'Mesoscale variations in surface stress, heat fluxes, and drag coefficient in the marginal ice zone during the 1983 marginal ice zone experiment', *Journal of Geophysical Research* **92**(C7), 6921–6932.

Feltham, D. L. (2005), 'Granular flow in the marginal ice zone', *Philosophical Transactions of the Royal Society A: Mathematical, Physical and Engineering Sciences* **363**(1832), 1677–1700.

Feltham, D. L. (2008), Sea ice rheology, *in* 'Annual Review of Fluid Mechanics', Vol. 40, Annual Reviews, Palo Alto, pp. 91–112.

Fennel, W. & Johannessen, O. M. (1998), 'Wind forced oceanic responses near ice edges revisited', *Journal of Marine Systems* **14**(1-2), 57–79.

Fer, I. & Sundfjord, A. (2007), 'Observations of upper ocean boundary layer dynamics in the marginal ice zone', *Journal of Geophysical Research* **112**, C04012.

Fetterer, F. & Untersteiner, N. (1998), 'Observations of melt ponds on arctic sea ice', *Journal of Geophysical Research-Oceans* **103**(C11), 24821–24835.

Flato, G. & Hibler, W. (1989), 'The effect of ice pressure on marginal ice-zone dynamics', *Ieee Transactions on Geoscience and Remote Sensing* **27**(5), 514–521.

Flocco, D. & Feltham, D. L. (2007), 'A continuum model of melt pond evolution on arctic sea ice', *Journal of Geophysical Research-Oceans* **112**(C8).

Flocco, D., Feltham, D. L. & Turner, A. K. (2010), 'Incorporation of a physically based melt pond scheme into the sea ice component of a climate model', *Journal of Geophysical Research-Oceans* **115**, C005568.

Flocco, D., Schroeder, D., Feltham, D. L. & Hunke, E. C. (2012), 'Impact of melt ponds on arctic sea ice simulations from 1990 to 2007', *Journal of Geophysical Research-Oceans* **117**. WOS:000309421800002.

Frankcombe, L. M. & Dijkstra, H. A. (2011), 'The role of atlantic-arctic exchange in north atlantic multidecadal climate variability', *Geophysical Research Letters* **38**, L048158.

Frankenstein, S., Loset, S. & Shen, H. H. (2001), 'Wave-ice interactions in barents sea marginal ice zone', *Journal of Cold Regions Engineering* **15**(2), 91–102. WOS:000168808700002.

Fujisaki, A. & Oey, L.-Y. (2011), 'Formation of ice bands by winds', *Journal of Geophysical Research-Oceans* **116**, C006655.

Garratt, J. R. (1994), *The atmospheric boundary layer*, Cambridge Univ Pr.

Gerber, H., Chang, S. & Holt, T. (1989), 'Evolution of a marine boundary-layer jet', *Journal of the Atmospheric Sciences* **46**(10), 1312–1326. WOS:A1989U627400002.

Glendening, J. W. (1994), 'Dependence of boundary layer structure near an ice-edge coastal front upon geostrophic wind direction', *Journal of Geophysical Research-Atmospheres* **99**(D3), 5569–5581.

Gordon, A. & Huber, B. (1990), 'Southern-ocean winter mixed layer', *Journal of Geophysical Research-Oceans* **95**(C7), 11655–11672. WOS:A1990DQ36000019.

Graversen, R. G., Mauritsen, T., Drijfhout, S., Tjernstrom, M. & Martensson, S. (2011), 'Warm winds from the pacific caused extensive arctic sea-ice melt in summer 2007', *Climate Dynamics* **36**(11-12), 2103–2112. WOS:000291165900005.

Gray, J. & Morland, L. W. (1994), 'A two-dimensional model for the dynamics of sea ice', *Philosophical Transactions of the Royal Society: Physical and Engineering Sciences (1990-1995)* **347**(1682), 219–290.

Greenan, B. J. W. & Prinsenberg, S. J. (1998), 'Wind forcing of ice cover in the labrador shelf marginal ice zone', *Atmosphere-Ocean* **36**(2), 71–93.

Grossman, R. & Friehe, C. (1986), 'Vertical structure of the southwest monsoon low-level jet over the central and eastern arabian sea', *Journal of the Atmospheric Sciences* **43**(24), 3266–3272. WOS:A1986G534600017.

Guest, P. & Davidson, K. (1991), 'The aerodynamic roughness of different types of sea ice', *Journal of Geophysical Research-Oceans* **96**(C3), 4709–4721.

Guest, P. S., Glendening, J. W. & Davidson, K. L. (1995), 'An observational and numerical study of wind stress variations within marginal ice zones', *Journal of Geophysical Research* **100**(C6), 10887–10.

Hayes, D. R., Jenkins, A. & McPhail, S. (2007), 'Autonomous underwater vehicle measurements of surface wave decay and directional spectra in the marginal sea ice zone', *Journal of Physical Oceanography* **37**(1), 71–83.

Herman, A. (2010), 'Sea-ice floe-size distribution in the context of spontaneous scaling emergence in stochastic systems', *Physical Review E* **81**(6), 066123.

Hewitt, H. T., Copsey, D., Culverwell, I. D., Harris, C. M., Hill, R. S. R., Keen, A. B., McLaren, A. J. & Hunke, E. C. (2011), 'Design and implementation of the infrastructure of HadGEM3: the next-generation met office climate modelling system', *Geoscientific Model Development* **4**(2), 223–253.

Hibler, W. D. I. (1979), 'A dynamic thermodynamic sea ice model', *Journal of Physical Oceanography* **9**(4), 815–846.

Hibler, W. D. I. (1986), Ice dynamics, *in* N. Untersteiner, ed., 'The Geophysics of Sea Ice', Plenum Press.

Hogstrom, U. & Smedman, A. (1984), 'The wind regime in coastal areas with special reference to results obtained from the swedish wind energy program', *Boundary-Layer Meteorology* **30**(1-4), 351–373. WOS:A1984TW65700017.

Holland, M. M., Bitz, C. M. & Tremblay, B. (2006), 'Future abrupt reductions in the summer arctic sea ice', *Geophysical Research Letters* **33**(23), L23503.

Holland, M. M., Bitz, C. M., Tremblay, L.-B. & Bailey, D. A. (2008), The role of natural versus forced change in future rapid summer arctic ice loss, *in* E. T. DeWeaver, C. M. Bitz & L. B. Tremblay, eds,

'Arctic Sea Ice Decline: Observations, Projections, Mechanisms, and Implications', Vol. 180, Amer Geophysical Union, Washington, pp. 133–150.

Holland, P. R. & Kwok, R. (2012), 'Wind-driven trends in antarctic sea-ice drift', *Nature Geoscience* **5**(12), 872–875. WOS:000311835800018.

Houghton, D. M. (1992), *Wind Strategy*, Fenhurst Books, Brighton UK.

Hunke, E. C. (2010), 'Thickness sensitivities in the CICE sea ice model', *Ocean Modelling* **34**(3-4), 137–149.

Hunke, E. C. & Dukowicz, J. K. (1997), 'An elastic-viscous-plastic model for sea ice dynamics', *Journal of Physical Oceanography* **27**(9), 1849–1867.

Hunke, E. C. & Lipscomb, W. H. (2010), CICE: the los alamos sea ice model documentation and software user's manual version 4.1., Technical Report LA-CC-06-012, T-3 Fluid Dynamics Group, Los Alamos National Laboratory, Los Alamos NM 87545.

Hunt, J. C. R., Orr, A., Rottman, J. W. & Capon, R. (2004), 'Coriolis effects in mesoscale flows with sharp changes in surface conditions', *Quarterly Journal of the Royal Meteorological Society* **130**(603), 2703–2731.

Jarmalavicius, D., Satkunas, J., Zilinskas, G. & Pupienis, D. (2012), 'The influence of coastal morphology on wind dynamics', *Estonian Journal of Earth Sciences* **61**(2), 120–130.

Johannessen, O. M., Johannessen, J. A., Morison, J., Farrelly, B. A. & Svendsen, E. A. (1983), 'Oceanographic conditions in the marginal ice zone north of svalbard in early fall 1979 with an emphasis on mesoscale processes', *Journal of Geophysical Research-Oceans* **88**(C5), 2755–2769.

Kantha, L. & Mellor, G. (1989), 'A numerical model of the atmospheric boundary layer over a marginal ice zone', *Journal of Geophysical Research* **94**, 4959–4970.

King, J. C., Doble, M. J. & Holland, P. R. (2010), 'Analysis of a rapid sea ice retreat event in the bellingshausen sea', *Journal of Geophysical Research-Oceans* **115**. WOS:000285465200002.

Kohout, A. L. & Meylan, M. H. (2008), 'An elastic plate model for wave attenuation and ice floe breaking in the marginal ice zone', *Journal of Geophysical Research* **113**(C9), C004434.

Korsnes, R. (1994), 'An ice drift series from the fram strait january-march 1992 based on ERS-1 SAR data', *Polar research* **13**(1), 55–58.

Kouraev, A. V., Papa, F., Buharizin, P. I., Cazenave, A., Cretaux, J. F., Dozortseva, J. & Remy, F. (2003), 'Ice cover variability in the caspian and aral seas from active and passive microwave satellite data', *Polar Research* **22**(1), 43–50. WOS:000183909600007.

Kwok, R. (2001), 'Deformation of the arctic ocean sea ice cover between november 1996 and april 1997: a qualitative survey', *IUTAM Scaling Laws in Ice Mechanics and Ice Dynamics* **94**, 315–322.

Kwok, R. (2004), 'Fram strait sea ice outflow', *Journal of Geophysical Research* **109**(C1), C01009.

Laing, A. K. & Brenstrum, E. (1996), 'Scatterometer observations of low-level wind jets over new zealand coastal waters', *Weather and Forecasting* **11**(4), 458–475.

Lepparanta, M. & Hibler, W. (1985), 'The role of plastic ice interaction in marginal ice-zone dynamics', *Journal of Geophysical Research-Oceans* **90**(NC6), 1899–1909.

Liu, A., Holt, B. & Vachon, P. (1991), 'Wave-propagation in the marginal ice-zone - model predictions and comparisons with buoy and synthetic aperture radar data', *Journal of Geophysical Research-Oceans* **96**(C3), 4605–4621.

Liu, A. Q., Moore, G. W. K., Tsuboki, K. & Renfrew, I. A. (2006), 'The effect of the sea-ice zone on the development of boundary-layer roll clouds during cold air outbreaks', *Boundary-Layer Meteorology* **118**(3), 557–581.

Long, Z. & Perrie, W. (2012), 'Air-sea interactions during an arctic storm', *Journal of Geophysical Research* **117**, D016985.

Lu, P., Li, Z. J., Zhang, Z. H. & Dong, X. L. (2008), 'Aerial observations of floe size distribution in the marginal ice zone of summer prydz bay', *Journal of Geophysical Research* **113**(C2), C003965.

Lu, Q., Larsen, J. & Tryde, P. (1989), 'On the role of ice interaction due to floe collisions in marginal ice-zone dynamics', *Journal of Geophysical Research-Oceans* **94**(C10), 14525–14537.

Marcq, S. & Weiss, J. (2012), 'Influence of sea ice lead-width distribution on turbulent heat transfer between the ocean and the atmosphere', *Cryosphere* **6**(1), 143–156.

Markus, T. (1999), 'Results from an ECMWF-SSM/I forced mixed layer model of the southern ocean', *Journal of Geophysical Research* **104**(C7), 15603–15.

Maslanik, J., Stroeve, J., Fowler, C. & Emery, W. (2011), 'Distribution and trends in arctic sea ice age through spring 2011', *Geophysical Research Letters* **38**. WOS:000292834700002.

Maslowski, W., Clement Kinney, J., Higgins, M. & Roberts, A. (2012), 'The future of arctic sea ice', *Annual Review of Earth and Planetary Sciences* **40**(1), 625–654.

Massom, R. A., Stammerjohn, S. E., Lefebvre, W., Harangozo, S. A., Adams, N., Scambos, T. A., Pook, M. J. & Fowler, C. (2008), 'West antarctic peninsula sea ice in 2005: Extreme ice compaction and ice edge retreat due to strong anomaly with respect to climate', *Journal of Geophysical Research-Oceans* **113**(C2).

Massom, R. A., Stammerjohn, S. E., Smith, R. C., Pook, M. J., Iannuzzi, R. A., Adams, N., Martinson, D. G., Vernet, M., Fraser, W. R., Quetin, L. B., Ross, R. M., Massom, Y. & Krouse, H. R. (2006), 'Extreme anomalous atmospheric circulation in the west antarctic peninsula region in austral spring and summer 2001/02, and its profound impact on sea ice and biota', *Journal of Climate* **19**(15), 3544–3571.

McClean, J., Bader, D., Bryan, F., Jones, P., Dennis, J., Mirin, A., Maltrud, M., Ivanova, D., Kim, Y. Y. & Boyle, J. (2010), 'A prototype two-decade fully-coupled fine-resolution CCSM simulation', *EGU General Assembly 2010, held 2-7 May, 2010 in Vienna, Austria, p. 5450* **12**, 5450.

McLaren, A. J., Banks, H. T., Durman, C. F., Gregory, J. M., Johns, T. C., Keen, A. B., Ridley, J. K., Roberts, M. J., Lipscomb, W. H., Connolley, W. M. & Laxon, S. W. (2006), 'Evaluation of the sea ice simulation in a new coupled atmosphere-ocean climate model (HadGEM1)', *Journal of Geophysical Research-Oceans* **111**(C12), C003033.

McPhee, M. G., Kwok, R., Robins, R. & Coon, M. (2005), 'Upwelling of arctic pycnocline associated with shear motion of sea ice', *Geophysical Research Letters* **32**(10), L021819.

McPhee, M. G., Maykut, G. A. & Morison, J. H. (1987), 'Dynamics and thermodynamics of the ice/upper ocean system in the marginal ice zone of the greenland sea', *Journal of Geophysical Research* **92**(C7), 7017–7031.

McPhee, M. G. & Morison, J. H. (2001), 'Under-ice boundary layer', *Encyclopedia of Ocean Sciences* pp. 3069–3076.

Meylan, M. & Squire, V. (1994), 'The response of ice floes to ocean waves', *Journal of Geophysical Research-Oceans* **99**(C1), 891–900.

Ogi, M. & Wallace, J. M. (2012), 'The role of summer surface wind anomalies in the summer arctic sea ice extent in 2010 and 2011', *Geophysical Research Letters* **39**. L09704.

Orr, A., Hanna, E., Hunt, J. C. R., Cappelen, J., Steffen, K. & Stephens, A. G. (2005*b*), 'Characteristics of stable flows over southern greenland', *Pure and Applied Geophysics* **162**(10), 1747–1778.

Orr, A., Hunt, J., Capon, R., Sommeria, J., Cresswell, D. & Owinoh, A. (2005*a*), 'Coriolis effects on wind jets and cloudiness along coasts', *Weather* **60**(10), 291–299.

Padman, L. & Dillon, T. M. (1991), 'Turbulent mixing near the yermak plateau during the coordinated eastern arctic experiment', *Journal of Geophysical Research* **96**(C3), 4769–4782.

Parkinson, C. L., Vinnikov, K. Y. & Cavalieri, D. J. (2006), 'Evaluation of the simulation of the annual cycle of arctic and antarctic sea ice coverages by 11 major global climate models', *Journal of Geophysical Research-Oceans* **111**(C7), C003408.

Pedersen, L. T. & Coon, M. (2004), 'A sea ice model for the marginal ice zone with an application to the greenland sea', *Journal of Geophysical Research* **109**, C001827.

Perovich, D. K., Grenfell, T. C., Light, B. & Hobbs, P. V. (2002), 'Seasonal evolution of the albedo of multiyear arctic sea ice', *Journal of Geophysical Research-Oceans* **107**(C10), C000438.

Pickart, R. S., Spall, M. A., Ribergaard, M. H., Moore, G. W. K., Milliff, R. F. et al. (2003), 'Deep convection in the irminger sea forced by the greenland tip jet', *Nature* **424**(6945), 152–156.

Pomeroy, K. R. & Parish, T. R. (2001), 'A case study of the interaction of the summertime coastal jet with the california topography', *Monthly Weather Review* **129**(3), 530–539.

Proelss, A. (2009), 'Governing the arctic ocean', *Nature Geoscience* **2**(5), 310–313.

Quadfasel, D., Gascard, J. & Koltermann, K. (1987), 'Large-scale oceanography in fram strait during the 1984 marginal ice-zone experiment', *Journal of Geophysical Research-Oceans* **92**(C7), 6719–6728.

Rasmussen, E., Pietrzak, J. & Brandt, R. (1999), 'A coupled ice–ocean model for the greenland, iceland and norwegian seas', *Deep Sea Research Part II: Topical Studies in Oceanography* **46**(6), 1169–1198.

Reed, R. J. & Campbell, W. J. (1960), 'Theory and observations of the drift of ice station alpha', *Seattle. Univ. of Washington, Dept. of Meteorology. Final Report to ONR under contract NR* pp. 307–250.

Robin, G. (1963), 'Wave propagation through fields of pack ice', *Philosophical Transactions of the Royal Society of London Series a-Mathematical and Physical Sciences* **255**(1057), 313–&.

Roed, L. P. & O'Brien, J. J. (1983), 'A coupled ice-ocean model of upwelling in the marginal ice zone', *Journal of Geophysical Research* **88**(C5), 2863–2872.

Rothrock, D. A. (1970), 'The pressure term in the constitutive law of an ice pack', *AIDJEX Bulletin* (2), 28–32.

Rudels, B. (1995), 'The thermohaline circulation of the arctic ocean and the greenland sea', *Philosophical Transactions of the Royal Society of London. Series A: Physical and Engineering Sciences* **352**(1699), 287–299.

Shaw, W. J., Stanton, T. P., McPhee, M. G. & Kikuchi, T. (2008), 'Estimates of surface roughness length in heterogeneous under-ice boundary layers', *Journal of Geophysical Research* **113**, C004550.

Shen, H. H., Hibler III, W. D. & Leppäranta, M. (1987), 'The role of floe collisions in sea ice rheology', *Journal of Geophysical Research* **92**(C7), 7085–7096.

Shen, H. H., Hibler, W. D. & Leppäranta, M. (1986), 'On applying granular flow theory to a deforming broken ice field', *Acta Mechanica* **63**(1), 143–160.

Simpson, J. E. (2007), *Sea Breeze and Local Winds*, new ed edn, Cambridge University Press.

Smedman, A., Tjernstrom, M. & Hogstrom, U. (1993), 'Analysis of the turbulence structure of a marine low-level jet', *Boundary-Layer Meteorology* **66**(1-2), 105–126. WOS:A1993LZ06200006.

Smith, D. & Bird, A. (1991), 'The interaction of an ocean eddy with an ice edge ocean jet in a marginal ice-zone', *Journal of Geophysical Research-Oceans* **96**(C3), 4675–4689.

Stroeve, J. C., Kattsov, V., Barrett, A., Serreze, M., Pavlova, T., Holland, M. & Meier, W. N. (2012), 'Trends in arctic sea ice extent from CMIP5, CMIP3 and observations', *Geophysical Research Letters* **39**, L052676.

Stroeve, J., Holland, M. M., Meier, W., Scambos, T. & Serreze, M. (2007), 'Arctic sea ice decline: Faster than forecast', *Geophysical Research Letters* **34**(9), L029703.

Stroeve, J., Serreze, M., Drobot, S., Gearheard, S., Holland, M., Maslanik, J., Meier, W. & Scambos, T. (2008), 'Arctic sea ice extent plummets in 2007', *Eos* **89**(2), 13–14.

Taylor, P. D. & Feltham, D. L. (2004), 'A model of melt pond evolution on sea ice', *Journal of Geophysical Research-Oceans* **109**(C12), C002361.

Thorndike, A. S., Rothrock, D. A., Maykut, G. A. & Colony, R. (1975), 'The thickness distribution of sea ice', *Journal of Geophysical Research* **80**(33), 4501–4513.

Thorpe, S. A. (2005), *The turbulent ocean*, Cambridge Univ Pr.

Tisler, P., Vihma, T., Müller, G. & Brümmer, B. (2008), 'Modelling of warm-air advection over arctic sea ice', *Tellus A* **60**(4), 775–788.

Tjernström, M. (2005), 'The summer arctic boundary layer during the arctic ocean experiment 2001 (AOE-2001)', *Boundary-Layer Meteorology* **117**(1), 5–36.

Toole, J. M., Timmermans, M. L., Perovich, D. K., Krishfield, R. A., Proshutinsky, A. & Richter-Menge, J. A. (2010), 'Influences of the ocean surface mixed layer and thermohaline stratification on arctic sea ice in the central canada basin', *Journal of Geophysical Research* **115**, C10018.

Toyota, T., Haas, C. & Tamura, T. (2011), 'Size distribution and shape properties of relatively small sea-ice floes in the antarctic marginal ice zone in late winter', *Deep-Sea Research Part Ii-Topical Studies in Oceanography* **58**(9-10), 1182–1193.

Tsamados, M., Feltham, D. L. & Wilchinsky, A. V. (2012), 'Impact of a new anisotropic rheology on simulations of arctic sea ice', *Submitted to Journal of Geophysical Research* .

Turner, J., Bracegirdle, T. J., Phillips, T., Marshall, G. J. & Hosking, J. S. (2013), 'An initial assessment of antarctic sea ice extent in the CMIP5 models', *Journal of Climate* **26**(5), 1473–1484. WOS:000315571800001.

Turner, J., Comiso, J. C., Marshall, G. J., Lachlan-Cope, T. A., Bracegirdle, T., Maksym, T., Meredith, M. P., Wang, Z. & Orr, A. (2009), 'Non-annular atmospheric circulation change induced by stratospheric ozone depletion and its role in the recent increase of antarctic sea ice extent', *Geophysical Research Letters* **36**. WOS:000265533800005.

Untersteiner, N. (1986), *The Geophysics of Sea Ice*, NATO ASI Series, Plenum Press.

Uotila, P., O'Farrell, S., Marsland, S. J. & Bi, D. (2012), 'A sea-ice sensitivity study with a global ocean-ice model', *Ocean Modelling* **51**, 1–18.

van Angelen, J. H., van den Broeke, M. R. & Kwok, R. (2011), 'The greenland sea jet: A mechanism for wind-driven sea ice export through fram strait', *Geophysical Research Letters* **38**, L047837.

van den Broeke, M. R. & Gallee, H. (1996), 'Observation and simulation of barrier winds at the western margin of the greenland ice sheet', *Quarterly Journal of the Royal Meteorological Society* **122**(534), 1365–1383.

Vihma, T. & Brummer, B. (2002), 'Observations and modelling of the on-ice and off-ice air flow over the northern baltic sea', *Boundary-Layer Meteorology* **103**(1), 1–27.

Vihma, T., Hartmann, J. & Lüpkes, C. (2003), 'A case study of an on-ice air flow over the arctic marginal sea-ice zone', *Boundary-Layer Meteorology* **107**(1), 189–217.

Vihma, T., Launiainen, J. & Uotila, J. (1996), 'Weddell sea ice drift: Kinematics and wind forcing', *Journal of Geophysical Research-Oceans* **101**(C8), 18279–18296.

Vinje, T. & Finnekåsa, Ø. (1986), *The ice transport through the Fram Strait*, number 186 *in* 'Skrifter', Norsk Polarinstitutt, Oslo.

Vinnikov, K. Y., Robock, A., Stouffer, R. J., Walsh, J. E., Parkinson, C. L., Cavalieri, D. J., Mitchell, J. F. B., Garrett, D. & Zakharov, V. F. (1999), 'Global warming and northern hemisphere sea ice extent', *Science* **286**(5446), 1934–1937.

Wadhams, P. (1978), 'Wave decay in marginal ice zone measured from a submarine', *Deep-Sea Research* **25**(1), 23–40.

Wadhams, P. (2000), *Ice in the Ocean*, CRC Press.

Wadhams, P., Squire, V., Goodman, D., Cowan, A. & Moore, S. (1988), 'The attenuation rates of ocean waves in the marginal ice-zone', *Journal of Geophysical Research-Oceans* **93**(C6), 6799–6818.

Wang, M. & Overland, J. E. (2009), 'A sea ice free summer arctic within 30 years', *Geophysical Research Letters* **36**(7), L07502.

Watanabe, T., Ikeda, M. & Wakatsuchi, M. (2004), 'Thermohaline effects of the seasonal sea ice cover in the sea of okhotsk', *Journal of Geophysical Research-Oceans* **109**(C9), C001905.

Weeks, W. F. & Ackley, S. F. (1986), The growth, structure, and properties of sea ice, *in* N. Untersteiner, ed., 'The Geophysics of Sea Ice', Plenum Press.

Wilchinsky, A. V. & Feltham, D. L. (2006*a*), 'Anisotropic model for granulated sea ice dynamics', *Journal of the Mechanics and Physics of Solids* **54**(6), 1147–1185.

Wilchinsky, A. V. & Feltham, D. L. (2006*b*), 'Modelling the rheology of sea ice as a collection of diamond-shaped floes', *Journal of Non-Newtonian Fluid Mechanics* **138**(1), 22–32.

Williams, G. D., Nicol, S., Raymond, B. & Meiners, K. (2008), 'Summertime mixed layer development in the marginal sea ice zone off the mawson coast, east antarctica', *Deep-Sea Research Part Ii-Topical Studies in Oceanography* **55**(3-4), 365–376.

Zemba, J. & Friehe, C. (1987), 'The marine atmospheric boundary-layer jet in the coastal ocean dynamics experiment', *Journal of Geophysical Research-Oceans* **92**(C2), 1489–1496. WOS:A1987G086200004.

Zhang, X. & Walsh, J. E. (2006), 'Toward a seasonally ice-covered arctic ocean: Scenarios from the IPCC AR4 model simulations', *Journal of Climate* **19**(9), 1730–1747.